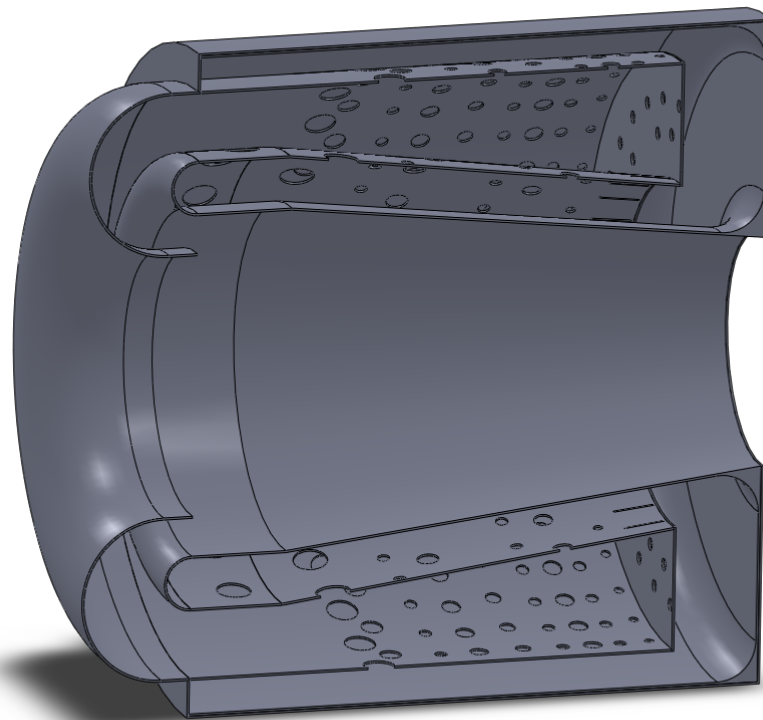


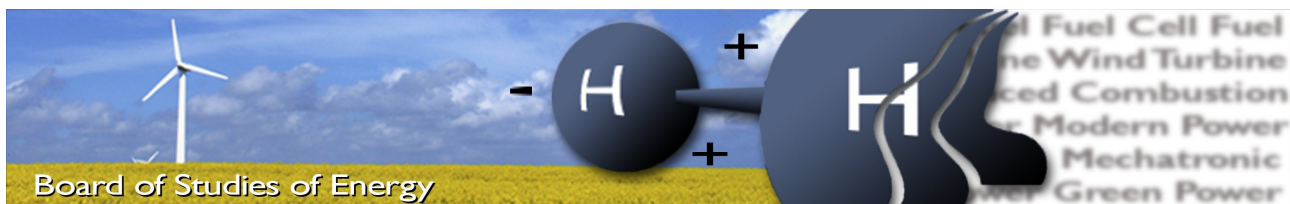
# *Numerical Investigation of the Soot Initiated Formation of Ultra Fine Particles in a Jet Turbine Engine Using Conventional Jet Fuel*

---

STUDENT REPORT  
MASTER'S THESIS  
SPRING 2012  
GROUP TEPE4-1005  
BOARD OF STUDIES OF ENERGY







**Title:** Numerical Investigation of the Soot Initiated Formation of Ultra Fine Particles in a Jet Turbine Engine Using Conventional Jet Fuel

**Semester:** 10th semester, Thermal Energy and Process Engineering

**Semester theme:** Master's Thesis

**Project period:** 01.02.12 to 31.05.12

**ECTS:** 30

**Supervisors:** Lasse Rosendahl and Thomas Condra

**Project group:** TEPE4-1005

---

Rasmus Møller Bering

---

Kåre Elgaard Buskov

**SYNOPSIS:**

A 3D numerical simulation in ANSYS Fluent, describing the combustion of Jet A in a SR-30 Turbojet Engine is made at a full-load case. This is done to investigate the formation of primary particles, which are mainly soot. The project is delimited to only focus on the formation in the combustion chamber of the turbine. A reduced reaction mechanism consisting of 38 reactions and 24 species, describing the combustion of Jet A as a surrogate fuel is used. This is chosen as it resembles the combustion characteristics of Jet A, and because soot precursors are present as species in the mechanism. From an initial literature study, the presence of soot precursors is said to predict the formation of soot under favorable conditions. A non-premixed combustion simulation is made in ANSYS Fluent, with the reduced reaction mechanism and the surrogate fuel incorporated. The boundary conditions of the model is based on results from experiments done on the SR-30 Turbojet Engine. From the results of this CFD simulation a soot formation pathway is analysed and predicted. This is compared with the soot formation model available in ANSYS Fluent. Despite it was not possible to obtain a fully evolved soot model, it indicates that the predicted soot formation is correct. In order to predict all pathways of the soot formation a more detailed reaction mechanism is needed.

Copies: 5  
Pages, total: 112  
Appendix: 4  
Supplements: CD

**By signing this document, each member of the group confirms that all participated in the project work and thereby all members are collectively liable for the content of the report.**



# Summary

A numerical study in ANSYS Fluent of combustion of jet fuel in a small scale test gas turbine, SR-30 Turbjet Engine, is conducted to investigate the soot initiated formation of ultra fine particles. Ultra fine particles are defined as particles with a diameter less than or equal to  $0.1 \mu\text{m}$ . They can cause health related issues when inhaled because they are able attach to the lung system in human beings.

Ultra fine particles account for most of the particle numbers in the airborne particulate matter, but a negligible size of the total mass. Particles are divided into two categories: primary particles and secondary particles. The primary particles are particles emitted directly from jet engines, while secondary particles are formed in the atmosphere as the emitted particles reach the ambient air in the exhaust, for example in the exhasut plume of an airplane. Only the primary particles are considered in this report.

Soot particles are emitted from jet engines from the combustion of hydrocarbon fuels. They consist of C-atoms and H-atoms in a ratio similar to the chemical formula  $\text{C}_8\text{H}$ . The soot particles fall in the size category of ultra fine particles. The formation of soot is a complex process of chemical reactions that still is not fully understood.

Today the widely accepted formation process of soot is that: Fuel is decomposed, and the first aromatic rings, *i.e.* phenyl ( $\text{C}_6\text{H}_5$ ) or benzene ( $\text{C}_6\text{H}_6$ ), are formed. These monocyclic aromatic hydrocarbons grow by the addition of gas-phase species like acetylene ( $\text{C}_2\text{H}_2$ ), ethylene ( $\text{C}_2\text{H}_4$ ) and isomers of these, to eventually form larger polycyclic aromatic hydrocarbons. Through nucleation the polycyclic aromatic hydrocarbons are converted to a soot nuclei, which is susceptible for gas-phase species to attach to its surface. The nuclei grows in size by agglomeration of the gas-phase species, and through coagulation the mass of the nuclei is further increased, while the number of nuclei is decreased. The result of these processes are the particles known as soot. Soot particles can be oxidated in which case they vanish, or are pyrolytically converted to a carbonaceous solid much like graphite, depending on the conditions and residence time of the soot particles in these conditions.

The project is delimitated to only focus on the combustion chamber of the turbine, and particles containing C-atoms and H-atoms. In the Project Description it is assumed that if soot precursors are located in the same zone, under favorable conditions, soot, and thereby ultra fine particles, are formed.

It is chosen to implement a reduced reaction mechanism, and a surrogate fuel to model the combustion of Jet A. The reduced reaction mechanism consists of 38 reactions and 24 species, and describes the combustion of a Jet A surrogate fuel, which consists of 72.7 wt% decane ( $\text{C}_{10}\text{H}_{22}$ ) + 9.1 wt% hexane ( $\text{C}_6\text{H}_{14}$ ) + 18.2 wt% benzene ( $\text{C}_6\text{H}_6$ ). Due to mass imbalance in a three of the reactions in the mechanism these reactions are modified based on literature, and mass balance is obtained to be able to implement it to the ANSYS Fluent simulation. 5 soot precursors are identified in the mechanism, which will be used to predict the soot formation in the modeled combustion chamber.

A 1/6 3D model of the combustion chamber of the SR-30 is constructed in Solidworks, and meshed using ANSYS ICEM. A mesh independency is made in which three different mesh sizes are compared; a 200,000

element mesh, a 400,000 element mesh and a 600,000 element mesh. The velocity of a point in the combustion chamber is traced for all three meshes, and compared. A comparison of the mean value of the tracked velocities show that they all very close, but they do not resemble a completely mesh independent solution. It is therefore chosen to proceed with the 600,000 element mesh, as the additional cells most likely yields a more accurate solution, by capturing more gradients.

A non-reacting hot flow CFD model is made using the measurement of fuel flow, temperatures and gauge pressures from an experiment made on the SR-30 Turbojet Engine by fellow students. The inlet temperature in the combustion chamber is set to 1000 K in order to create a high temperature flow field. The inlet air mass flow is 0.05764 kg/s which corresponds to the experiment results measured at 80,000 RPM, which is full speed, for the SR-30 Turbojet Engine.

The hot flow simulation serves as an initial solution of the combustion chamber, and is used as basis in the reacting CFD model. The reacting CFD model is modeled as non-premixed combustion with the Steady Flamlet model. Air is set as the oxidizer, and the surrogate fuel from the reduced mechanism as fuel. The boundary conditions are updated to correspond to the experimental results, and the reduced reaction mechanism is imported to ANSYS Fluent to be used in the combustion simulation.

The results of the CFD model show that benzene, acetylene, ethylene and high temperatures are present in the same areas. From these facts a soot formation pathway is predicted using soot formation theory. The pathway is that the polycyclic aromatic hydrocarbon, "cyclopenta acenaphthylene", is formed within the flame by the addition of ethylene to the 2-ring polycyclic aromatic hydrocarbon, naphthalene, that is formed from addition of acetylene and ethylene to benzene. It is assumed that the "cyclopenta acenaphthylene" can nucleate to form soot nuclei, which then can grow to a soot particle. With the assumeably presence of soot particles, it predicts the presence of ultra fine particles as well.

A post-process soot model, Moss-Brooke-Hall, available in Fluent is used to predict the soot formation, to compare the predicted soot formation pathways. It was not possible to make the model converge to the  $10^{-6}$  recommended by ANSYS Fluent, which means the soot formation is not fully evolved. But the results obtained indicate that soot is formed in the same area as the analysis and prediction with the use of the knowledge and theory obtained showed.

The predicted soot formation pathway is only one of many, and a much more detailed mechanism is needed in order to predict all of the different PAHs that can nucleate to form soot nuclei. However the computational requirements and time needed for a CFD simulation using a detailed reaction mechanism, that contains all of the soot precursors and formation, are extensive.

# Preface

This Master's thesis was prepared during the 4th semester of the Master in Thermal Energy and Process Engineering Technology at the Board of Studies of Energy at Aalborg University.

Along with this report a CD is included. This CD contains the following:

- The case and data files for the different simulations in ANSYS Fluent.
- The ANSYS ICEM mesh files.
- The Solidworks CAD drawing of the geometry.
- The Chemkin mechanism and thermodynamic data file.
- The report in a PDF version.

The authors of this report would like to thank the following people:

- Groups TE6-603 and TE6-604 for experimental data from the SR-30 Turbojet Engine.
- Associate Professor Chungun Yin for answering our questions on CFD.



# Nomenclature

Symbol	Unit	Specification
$a_n$	[—]	Thermodynamic coefficients
$A$	[ $cm, molec, s$ ]	Pre-exponential factor
$A/F$	[—]	Air-fuel ratio
$A/F_{stoich}$	[—]	Stoichiometric air-fuel ratio
$C_p$	[ $\frac{kJ}{kg-K}$ ]	Heat capacity
$D$	[ $m$ ]	Particle Diameter
$E_a$	[ $\frac{kcal}{mol}$ ]	Activation Energy
$H$	[ $J$ ]	Enthalpy
$k$	[ $\frac{m^2}{s^2}$ ]	Turbulent kinetic energy
$mass\%$	[—]	Mass percent
$\dot{m}_{air}$	[ $\frac{kg}{s}$ ]	Mass flow of air
$\dot{m}_{fuel}$	[ $\frac{kg}{s}$ ]	Mass flow of fuel
$M_{air}$	[ $\frac{kmol}{kg}$ ]	Molar mass of air
$M_{fuel}$	[ $\frac{mol}{kg}$ ]	Molar mass of fuel
$n$	[—]	Number of C-atoms
$n$	[—]	Power of temperature (Arrhenious)
$N$	[—]	Number of particles
$P$	[ $Pa$ ]	Pressure
$R$	[ $\frac{J}{mol-K}$ ]	Gas constant
$S$	[ $\frac{kJ}{K}$ ]	Entropy
$T$	[ $K$ ]	Temperature
$vol\%$	[—]	Volume percent
$\dot{V}_{fuel}$	[ $\frac{m^3}{s}$ ]	Volume flow of fuel
$wt\%$	[—]	Weight percent
$x$	[—]	x-direction of spray
$y$	[—]	y-direction of spray
$z$	[—]	z-direction of spray
$\epsilon$	[ $m^2/s^3$ ]	Dissipation of kinetic energy
$\epsilon_{external}$	[—]	External wall radiation
$\phi$	[—]	Equivalence Ratio
$\lambda$	[ $m$ ]	Taylor microscale
$\nu$	[ $\frac{m^2}{s}$ ]	Kinematic viscosity
$\nu_{stoich}$	[—]	Stoichiometric coefficient

**Table 1:** Symbols with corresponding units used throughout the report.

## Abbreviations

Abbreviation	Meaning
APU	Auxiliary Power Unit
ASTM	American Society for Testing and Materials
CFD	Computational Fluid Dynamics
CPH	Copenhagen Airport
DEF STAN	Defence Standard
DMU	Dansk Miljøundersøgelse
FAAE	Fatty Acid Alkyl Ester
FAEE	Fatty Acid Ethyl Ester
FAME	Fatty Acid Methyl Ester
GHG	Green House Gasses
HC	Hydrocarbons
HRJ	Hydroprocessed Renewable Jet Fuel
JIG	Joint Inspection Group
LCA	Life Cycle Assessments
MAH	Monocyclic Aromatic Hydrocarbon
PAH	Polycyclic Aromatic Hydrocarbon
PM	Particulate Matter
SPK	Synthetic Paraffinic Kerosene
SR-30	SR-30 Turbojet Engine
UFP	Ultra Fine Particles

*Table 2: Abbreviations used throughout the report.*

# Contents

<b>1</b>	<b>Introduction</b>	<b>1</b>
<b>2</b>	<b>Jet Fuels</b>	<b>5</b>
2.1	Conventional Jet Fuel . . . . .	5
2.2	Alternative Jet Fuels . . . . .	11
2.3	Emissions from Alternative Jet Fuels Compared to Conventional Jet Fuels . . . . .	13
<b>3</b>	<b>Combustion</b>	<b>15</b>
3.1	Hydrocarbon Combustion . . . . .	15
3.2	Particles . . . . .	18
3.3	Soot . . . . .	20
<b>4</b>	<b>Project Description</b>	<b>27</b>
4.1	Project delimitation . . . . .	27
<b>5</b>	<b>Modelling of Combustion</b>	<b>29</b>
5.1	Surrogate Fuels . . . . .	29
5.2	Reaction Mechanisms . . . . .	30
5.3	Choosing a Reduced Chemical Reaction Mechanism . . . . .	31
5.4	Kinetic Model - Cantera . . . . .	35
<b>6</b>	<b>SR-30 Turbojet Engine</b>	<b>37</b>
6.1	The SR-30 Turbojet Engine . . . . .	37
6.2	Operation Conditions and Dimensions . . . . .	38
6.3	The Combustion Chamber . . . . .	39
6.4	Air Delivery System . . . . .	40
6.5	Liquid Fuel Injection . . . . .	40
6.6	SR-30 Experiments . . . . .	41
6.7	Inlet and Outlet Conditions of the Combustor Zone . . . . .	43
<b>7</b>	<b>Modeling</b>	<b>45</b>
7.1	Geometry and Mesh . . . . .	45
7.2	CFD Model . . . . .	54
<b>8</b>	<b>Results</b>	<b>63</b>
8.1	Results from the Combustion Simulation . . . . .	63

8.2 Soot Formation Discussion . . . . .	71
8.3 Results from the Combustion Simulation incl. Moss-Brookes-Hall Soot Model . . . . .	73
<b>9 Conclusion</b>	<b>77</b>
<b>10 Future Work</b>	<b>79</b>
<b>Bibliography</b>	<b>79</b>
<b>11 Appendix A</b>	<b>87</b>
11.1 Structure of CHEMKIN Files . . . . .	87
<b>12 Appendix B</b>	<b>91</b>
12.1 Data From Experiment . . . . .	91
<b>13 Appendix C</b>	<b>93</b>
13.1 Modelling results . . . . .	93
<b>14 Appendix D</b>	<b>97</b>
14.1 Mesh Independency Study . . . . .	97

The aviation industry faces a challenge which will take a considerable amount of research, testing and global cooperation to overcome. The challenge is to incorporate alternative jet fuels into the industry at a competitive cost compared to conventional fuels while at the same time limit the emission of Green House Gasses (GHG). There are two main reasons why alternative jet fuels are interesting, both of which drive the aviation industry to investigate and invest large amounts of money into this challenge [Price, 2011]. As described by several authors these reasons are the rising price of conventional jet fuel and the environmental effects caused by the emissions from the conventionally jet fuelled aeroengines [Hemighaus et al., 2006b] [Hileman et al., 2008] [Kinder and Rahmes, 2009] [Altman et al., 2010].



**Figure 1.1:** The monthly development in jet fuel price since 1998 to 2012 [Barrientos and Soria, 2012]. The price has increased by 574 % (excluding inflation) from October 1998 to January 2012. An obvious reason for the large interest in alternative jet fuels shown from the aviation industry.

Already in the 1970s and 1980s a large scale investigation of shale-derived jet fuel was made by the U.S. Air Force, and the search for alternative jet fuels has been going on ever since [Hemighaus et al., 2006b]. Amongst the fuels considered in aviation biofuels shows to be most promising in terms of CO<sub>2</sub> emission reductions [Bailis and Baka, 2010]. The reason for this is the fact that the GHG emissions from biofuels can be largely reduced compared to the emissions from conventional jet fuel as described by several authors [Hileman et al., 2009] [Kinder and Rahmes, 2009] [Altman et al., 2010]. One of the reasons why biofuels has a lower GHG emission is because it has a higher content of oxygen compared to conventional jet fuel, see Section 2.2.1 on page 11. Bailis and Baka [2010] compared the Life Cycle Assessment (LCA) of different (bio)Synthetic Paraffinic Kerosenes (SPK) produced from *Jatropha curcas* (small tree with seeds) against a reference scenario of conventional jet fuel. The data used in the LCAs were based on data from the *Jatropha* growers. Different

scenarios are analyzed where the variable is the location of the farm. A reduction up to 85 % in GHG emissions compared to the reference scenario is found in the case of planting *Jatropha* in former agro-pastoral land. Kinder and Rahmes [2009] reports similar results for an well-to-wake LCA of *Jatropha*, which shows a reduction of 65-80 % in GHG emissions compared to conventional jet fuel.

Up to today a number of alternative jet fuels have been used in blends with jet fuel, in both test flights and commercial flights. In July 2011 a new American Society for Testing and Materials (ASTM) standard, D7566-11, made it possible to blend up to 50% bio-derived synthetic fuel into conventional jet fuel, thus enabling the use of biofuel blends for commercial flights [Ponticel, 2012]. Tabel 1.1 shows the date of flight, aircraft and engine type, and fuel used in different test flights and commercial flights. Hydroprocessed Renewable Jet (HRJ) fuels is produced from for example plant oil from which the oxygen first is removed by deoxygenation and then hydroisomerized (conversion of a compound into a different isomeric form via the use of an intermediate alkene) in order to create hydrocarbons in the range of Jet-A [Hileman et al., 2009].

**Table 1.1:** Test flights and commercial flights done with blends of renewable jet-fuels [Hileman et al., 2009, and references therein]

<b>Test flights</b>			
<b>Airline</b>	<b>Air New Zealand</b>	<b>Continental Airlines</b>	<b>Japan Airline</b>
Date	December 30, 2008	January 7, 2009	January 30, 2009
Aircraft Type	Boeing 747-400	Boeing 737-800	Boeing 747-300
Engine Type	Rolls-Royce RB211	CFM56-7B	Pratt and Whitney JT9D
Fuel Mixture	<i>Jatropha</i> HRJ (50%) Conv. Jet fuel (50%)	<i>Jatropha</i> HRJ (2.5%) Algae (47.5%) Conv. Jet fuel (50%)	Camelina HRJ (42%), <i>Jatropha</i> (< 8%) Algae (< 1%) Conv. Jet fuel (50%)
<b>Commercial flights</b>			
<b>Airline</b>	[Finnair, 2012] <b>Finnair</b>	[AeroMexico, 2012] <b>AeroMexico</b>	[KLM, 2012] <b>KLM</b>
Date	July 20, 2011	August 1, 2011	June 22, 2011
Aircraft Type	Airbus A319	Boeing 777-200	Boeing 737-800
Engine Type	CFM56	CFM56-7B	CFM56-7B26
Fuel Mixture	Cooking Oil Biofuel (50%) Conv. Jet fuel (50%)	<i>Jatropha</i> HRJ (30%) Conv. Jet fuel (70%)	Cooking Oil Biofuel (50%) Conv. Jet fuel (50%)

There is an allowed limit of 50 % blend of some alternative jet fuels with the conventional jet fuels for commercial flights [Lewis, 2011]. Allowing blends of alternative jet fuels into conventional jet fuels is one of the ways to achieve the emission reduction goals set by the aviation industry. The International Air Transport Association (IATA) hopes to be using 6 % blends by 2020, and a goal of 50 % reduction in CO<sub>2</sub> emissions from 2005 levels by 2050 [Bailis and Baka, 2010].

Although several authors, [Hileman and Wong, 2008] [Kinder and Rahmes, 2009] [Bailis and Baka, 2010] [Altman et al., 2010] [Corporan et al., 2011], have investigated the emissions from different alternative jet fuels and their corresponding possible emission reduction there is still a need for further research to map the cost-benefits of each fuel, and increase the understanding of the emissions to establish a larger alternative jet fuel database. What also adds to the list of research needed is the fact that almost each individual batch of alternative

jet fuel contains a different composition of hydrocarbon components [Corporan et al., 2011]. This is due to the variation from one feedstock source to another, variation in production conditions; e.g. temperature, pressure, etc.

Regulations for reductions in pollutant emissions from airplanes are scheduled to begin in 2012, which sets a limit of 97% of the average annual emissions for the years 2004, 2005 and 2006 [EurActiv, 2011]. One of the more recent fields of interest following these new emission limits is the formation of Ultra Fine Particles (UFP) from jet fuel combustion in aeroengines and Auxiliary Power Units (APU). UFPs are particles with a diameter less than 1  $\mu\text{m}$  (termed  $\text{PM}_{0.1}$  (Particulate Matter)), and investigations have shown that they contribute to the greenhouse effect as well as possibly causing severe human health problems [Morawska et al., 2004].

Danmarks Miljøundersøgelse (DMU) in cooperation with Copenhagen Airport (CPH) has made an investigation of the emissions of UFPs from the airplanes at CPH [Ellermann et al., 2011]. The key results shows that on the tarmac of the airport the emission of UFPs is at least three times larger than the emissions measured at the busiest road in the center of Copenhagen.

Antal per $\text{cm}^3$	August - December 2010				Januar - Juni 2011			
	Samlet Antal	6 - 40 nm	40 - 109 nm	109 - 700 nm	Samlet Antal	6 - 40 nm	40 - 109 nm	109 - 700 nm
Forplads B4	31900	27900	3100	900	38600	32600	4600	1400
Station Vest					11000	7500	2500	1100
Station Øst	10000	7500	1800	700				
H. C. Andersens Boulevard	16100	9900	4700	1600	13400	7800	4100	1400
H. C. Ørsteds Institut	5500	2300	2200	1000	6500	2300	2800	1400
Lille Valby / Risø	3700	1400	1500	900	4000	1200	1700	1000

Figure 1.2: Mean values for the total particle size distribution measured in CPH and the area around [Ellermann et al., 2011].



Figure 1.3: The place in CPH where the measurements were taken [Ellermann et al., 2011].

As of February 2012, there exist no limits for the emission of UFPs ( $PM_{0.1}$ , particles with diameter less than  $0.1 \mu\text{m}$ ), only for fine ( $PM_{2.5}$ , particles with diameter less than  $2.5 \mu\text{m}$ ) and coarse ( $PM_{10}$ , particles with diameter less than  $10 \mu\text{m}$ ) particles. Limits for UFP emission are needed which is also highlighted and stressed by Press-Kristensen [2011]. How and why these UFPs are formed is not clear, and more research is needed in order to determine the chemistry and composition of UFPs as it varies from place to place, and from source to source.

**Note that the Project Description and Project Delimitation is located in Chapter 4 on page 27, and that the chapters leading to this is used to establish knowledge needed to formulate the Project Description.**

The following chapter explains conventional and alternative jet fuels in details, in order to establish knowledge on jet fuels and the emissions resulting from the combustion of these. This knowledge is useful when determining what compounds are present in jet fuel, conventional or alternative, that reacts during combustion to ultimately form UFPs.

The chemical properties and composition of the conventional and alternative jet fuel are investigated to highlight the advantages and disadvantages of the conventional and alternative fuels. A comparison of the emissions from conventional and alternative jet fuels are made in the last section of this chapter. If nothing else is mentioned, this section is based on [Hemighaus et al., 2006a] and [Lefebvre and Ballal, 2010].

## 2.1 Conventional Jet Fuel

The term conventional jet fuel covers fossil-based jet fuel, *i.e.* fuel which is refined from crude oil/petroleum [Hemighaus et al., 2006b]. Since the 1950s where a wide development in the commercial jet industry took place, and kerosene-dominant fuels were selected to have the best properties as a jet fuel, these type of fuels have been used in the aviation business. The two dominating fuels since then and up till now are Jet A (kerosene), used in the USA, and Jet A-1 used in the majority of the rest of the world. [Blakey et al., 2010]

**Table 2.1:** Some specification properties from the ASTM D1655 and DEF STAN 91-91 compared.[Hemighaus et al., 2006a]

<b>Fuel</b>	Jet A	Jet A-1
Specification	ASTM D 1655	DEF STAN 91-91
Acidity, max [mg KOH/g]	0.10	0.015
Aromatics, max vol [-] %	25	25
Naphtalenes, max vol [-] %	3.0	3.0
Sulfur, mass % [-]	0.30	0.30
Sulfur, mercaptan, mass % [-]	0.003	0.003
Flash Point, min [°C]	38	38
Density @ 15°C, [kg/m <sup>3</sup> ]	775-840	775-840
Freezing Point, max [°C]	-40	-47.0
Viscosity @ -20°C, max [mm <sup>2</sup> ]/s]	8.0	8.0
Net Heat of Combustion, min [MJ/kg]	42.8	42.8
Smoke Point, min [mm]	18	19
Existent gum, max [mg/100 ml]	7	7

Fuel specifications for these two major types of jet fuels are specified in the ASTM standard D1655 and Defence Standard (DEF STAN) 91-91. Jet A follows the specifications of ASTM D1655, while Jet A-1 follows the specification of DEF STAN 91-91. However, many refineries follow a specification referred to as the Joint Checklist. This is made by the Joint Inspection Group (JIG) which is a group of oil companies who have gathered the most restrictive limitations from ASTM D1655 and DEF STAN 91-91 in one document; Aviation Fuel Quality Requirements for Jointly Operated Systems. Hence then the refineries are able to produce jet fuel which meet both specifications.

Table 2.1 on the preceding page shows some of the required specification properties of Jet A and Jet A-1. It is seen that there are minor differences between the two set of requirements, where the most significant is the difference in freezing point and the acidity.

### 2.1.1 Hydrocarbons

Conventional jet fuels consist of mixtures of hundreds of different hydrocarbons, *i.e.* compounds with only carbon and hydrogen. The specification properties made however, have implicitly restricted the hydrocarbons to carbon numbers of approximately 8 to 16 [Edwards, 2010]. Depending on the number of C-atoms, they may be either gaseous, liquid, or solid at normal temperature and pressure:

- Hydrocarbons with up to 4 C-atoms are gaseous
- Hydrocarbons from 4 to 19 C-atoms are liquids
- Hydrocarbons with 20 or more C-atoms are solids.

It is common to divide the hydrocarbons in jet fuels into 4 different categories, that is; *Paraffins*, *Olefins*, *Naphthenes* and *Aromatics*. Each of these categories is evaluated with regard to their structure and physical properties in the following sections.

#### Paraffins

Paraffins, also called kerosenes, are a hydrocarbon compound of C-atoms connected in a chain. The general chemical formula is  $C_nH_{2n+2}$ . Here the  $n$  is the number of C-atoms, *i.e.* the carbon number, of the hydrocarbon. Paraffins only have single bonds between the C-atoms, and the C-atoms which create the base structure of the paraffin are positioned in a zig-zag pattern, but for clarity they are shown as a linear structure.

Two examples of basic paraffins are shown in Figure 2.1

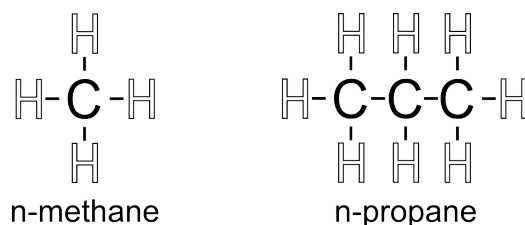


**Figure 2.1:** Examples of the chemical structure of paraffins.

Isomers (compounds with same molecular formula but different structures) are called isoparaffins. These have branches of C-atoms from the main straight structure of the paraffin. An example of these is 1,2,4-

trimethylpentane which is shown in Figure 2.2. The numbers in front of the chemical name shows which number C-atom in the structure the methyl group (CH<sub>3</sub>) is connected to.

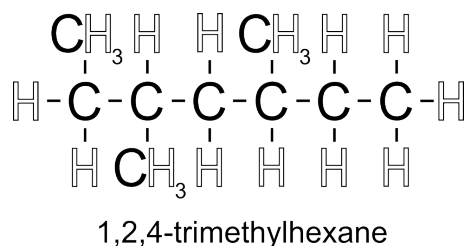


**Figure 2.2:** An example of the chemical structure of isoparaffins.

Compared to other hydrocarbon fuels, paraffins have the properties of higher gravimetric heat of combustion, lower density and freeze point, and a higher hydrogen-to-carbon ratio. They also have a high thermal stability, and combustion of paraffins is absent of exhaust smoke and deposition of coke.

### Naphthenes

Naphthenes, also known as cycloparaffins, are saturated hydrocarbons where the C-atoms are connected in a ring, as opposed to the chains of the paraffins. Single ring naphthenes have the chemical formulae C<sub>n</sub>H<sub>2n</sub>. Illustrations of naphthenes are seen in Figure 2.3. They have equal names according to carbon numbers as the corresponding paraffins, but the term *cyclo* is put in front.

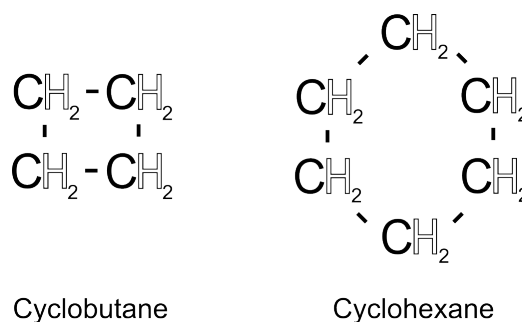


**Figure 2.3:** An example of the chemical structure of naphthenes.

As with paraffins, naphthenes have a good thermal stability, low tendency to form soot, and a high gravimetric heat of combustion. They also aid in reducing the freezing point of the fuel, which is suitable in the high altitude flights [Blakey et al., 2010].

### Olefins

Olefins, also called alkenes, has the same structure as paraffins, but additionally they contain at least one double bond between neighboring C-atoms. Hence they must consist of at least 2 C-atoms. Hereby the general chemical formula for olefins with a single double bond is the same as for single ring naphthenes, *i.e.* C<sub>n</sub>H<sub>2n</sub>. Examples of olefins are illustrated in Figure 2.4 on the following page.

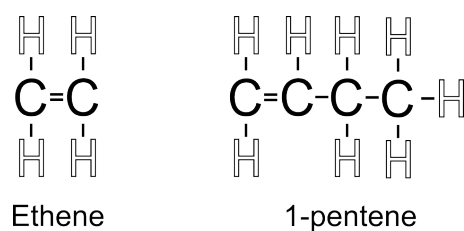


**Figure 2.4:** An example of the chemical structure of olefins.

As with paraffins, isomers of olefins exist when 4 or more C-atoms are present in the compound.

Olefins do not usually appear in petroleum, but they are created in the refineries via conversion processes. They are very chemically active as they are unsaturated, *i.e.* there are not as many H-atoms attached as is possible. This leads to reactions with other compounds that can create rubberlike material and gums. Hence olefins are highly unwanted in jet fuel, and are therefore only present in small trace concentrations.

## Aromatics

Aromatics are unsaturated compounds consisting of one or more rings of 6 C-atoms as naphthenes, but with 3 double bonds distributed between every second C-atom. In reality though, the bonds are shown to be distributed evenly among the C-atoms. Hence aromatics has less hydrogen bonded than naphtenes, which leads to a lower specific energy of the compounds.

The chemical formula for monocyclic (which means they consist of only one carbon ring) aromatics is  $C_nH_{2n-6}$ . More complicated monocyclic aromatic compounds can also be made, by for example exchanging some H-atoms with hydrocarbon groups. An illustration of the simplest aromatic, benzene, and the more complex toluene is shown in Figure 2.5.

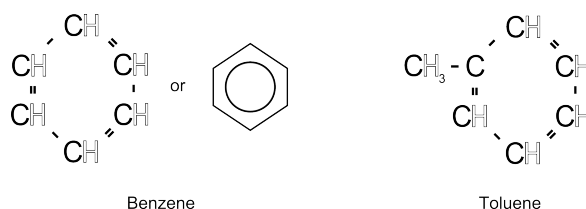


**Figure 2.5:** An example of the chemical structure of monocyclic aromatics.

Polycyclic aromatics consist of several 6 C-atom rings, where some C-atoms are shared between the rings. An example of this is naphthalene, which is the simplest dicyclic aromatic, illustrated in Figure 2.6 on the facing page.

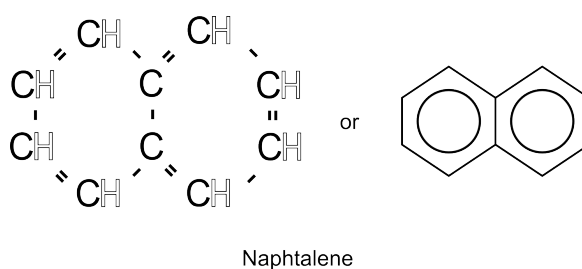


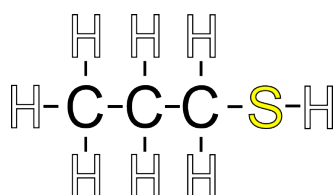
**Figure 2.6:** An example of the chemical structure of polycyclic aromatics.

An advantage of aromatics in jet fuel is its capability to cause swelling of o-rings in the fuel system, which helps to seal off the high pressure system, and its ability to act as a lubricant [Altman et al., 2010]. Disadvantages however are primarily the aforementioned lower specific energy, higher soot formation, a significantly high hygroscopicity which can cause the release of ice crystals in the fuel at low temperatures, and the ability to act as a strong solvent on rubber which is unwanted in certain fuel tanks. All in all, even though the disadvantages of aromatics in jet fuel are dominating, the lubricating effect is important and some aromatics, according to [Ebbinghaus and Wiesen, 2001] a minimum of 10%, are necessary to avoid the the use of additives [Altman et al., 2010].

### Sulfur Compounds

Even though the main components in crude oil is different kinds of hydrocarbons, there are also compounds which consist of other atoms than just hydrogen and carbon. These atoms are mainly sulfur and nitrogen. These are bound into the structures of carbon and hydrogen, creating new compounds. They only represent a very small part of the crude oil, but they are still very important in regards to fuel properties as for example thermal and storage stability.

Mercaptans are one kind of compounds where sulfur is present in the molecular structure. They consist of a sulfur atom connected to a hydrogen atom and a hydrocarbon. An example of a mercaptan is seen in Figure 2.7.



Propyl mercaptan

**Figure 2.7:** An example of the chemical structure of mercaptans.

By oxidizing mercaptans, disulfides can be created, which consist of two sulphur atoms bonded, and each of them connected to a hydrocarbon. More variations of sulphur compounds are sulfides where a sulfur compound is situated between two C-atoms, and thiopenes where a sulfur atom is bound to an aromatic compound. A disulfide, sulfide, and a thiopene is illustrated in Figure 2.8 on the following page.

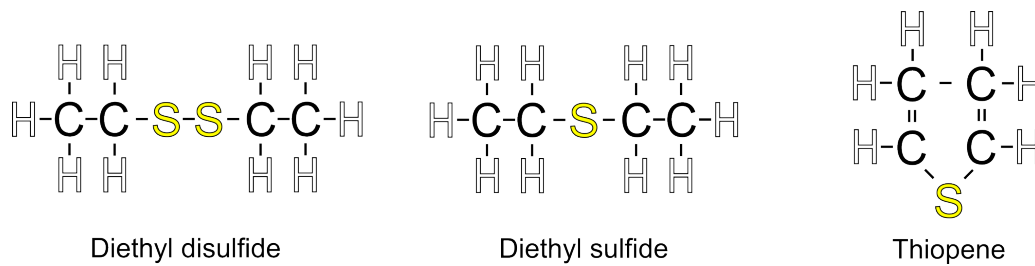


**Figure 2.8:** An example of the chemical structure of disulfides, sulfides, and thiophenes.

The jet fuel limits for mercaptans and sulfur in general can be seen in Table 2.1 on page 5.

## Fuel Composition

On average, a jet fuel has the composition of 60% paraffins, dependent on the source of the petroleum and the refining process, 20% aromatics, and 20% naphthenes. [Lefebvre and Ballal, 2010] A survey of the average chemical compound composition of jet fuels has also been made. This was done by using the ASTM D2425 test standard for hydrocarbons on a sample set of 55 jet fuels [Edwards, 2010]. This method divides the fuel up in categories as seen in Table 2.2.

**Table 2.2:** The average hydrocarbon composition using ASTM D2425 on a sample set of 55 jet fuels. [Edwards, 2010]

Chemical compound	%	Hydrocarbon group
(n-/iso-) paraffins	58.78	Paraffins
Monocycloparaffins	10.89	Naphthenes
Dicycloparaffins	9.25	Naphthenes
Tricycloparaffins	1.08	Naphthenes
Alkyl Benzenes	13.36	Aromatics
Indans/tetralins	4.9	Aromatics
Naphthalene	0.13	Aromatics
Substituted naphthalenes	1.55	Aromatics

As seen when adding the numbers, this obtained average is in good relation with the numbers from Lefebvre and Ballal [2010]. Additionally jet fuel hold around 500 ppm of sulfur. Figure 2.9 on the next page show a gas chromatography of the chemical composition of Jet A.

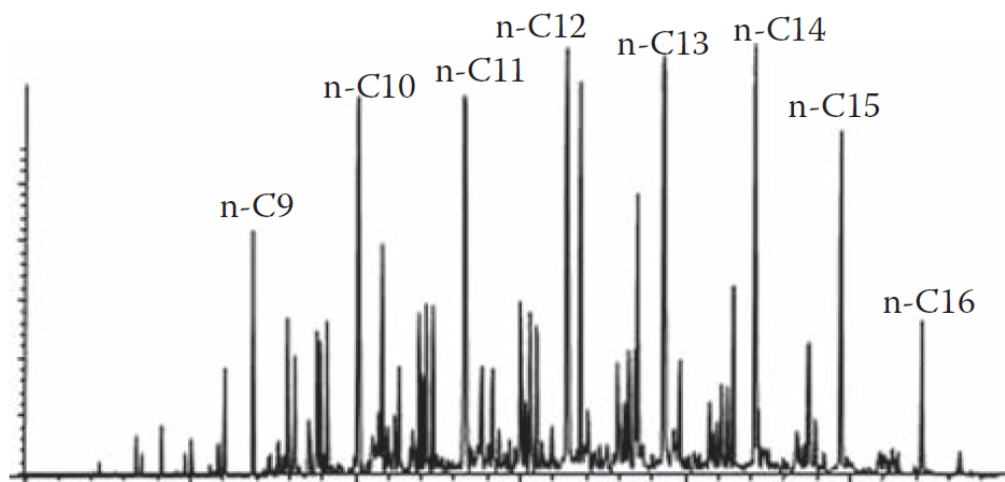


**Figure 2.9:** Gas chromatography of the chemical composition of Jet A.[Lefebvre and Ballal, 2010]

## 2.2 Alternative Jet Fuels

As mentioned in the Introduction in chapter 1 on page 1, the fuel industry spend a lot of research on alternative fuels for use in commercial aviation. There are several kinds of alternative fuels still considered, some which is still based on fossil feedstock and some based on renewable resources, *e.g.* biofuels from biomass. Some alternative fuels considered as substitutes for conventional jet fuel:

- Fischer Tropsch
- Hydro-treated Renewable Jet
- Biodiesel
- Cryogenic fuels

This report does not cover the details of the different alternative fuels, but only covers the details of biodiesel. Biodiesel is the only alternative fuel made available for the authors. Several authors describe the other alternative fuels in detail, *e.g.* Hemighaus et al. [2006a], Bailis and Baka [2010], Vertés et al. [2010] and Luque et al. [2011].

### 2.2.1 Biodiesel

It is possible to produce biodiesel from a range of different feedstocks. Amongst these are edible vegetable oils and animal fat (termed first generation biofuels), non-edible oils and side streams from refining and the much anticipated future feedstock, algae (termed second generation biofuels) [Luque et al., 2011]. Algae is estimated to yield up to ten times the amount of oil per hectare compared to other biofuels, *e.g.* soybeans and corn [Vertés et al., 2010]. This large production potential is mainly related to the fact that algae grows in water and thus there is no limit to water and nutrient for the plants, which in turn maximizes the growth rate and productivity. However a lot more research is needed in order to make large scale algae production competitive. More details on biodiesel produced from algae can be found in Vertés et al. [2010, Chap. 8].

Biodiesel is composed of Fatty Acid Alkyl Esters (FAAE). The alkyl group can be replaced with two types of alkyls; ethyl and methyl. These biodiesel types are termed Fatty Acid Ethyl Esters (FAEE) and Fatty Acid Methyl Esters (FAME), where FAME is the most common. FAME is the product of transesterification (basically a process combination of methanol and fats and oils) [Luque et al., 2011]. Details will not be given on the production methods of biodiesel. Information on transesterification and esterification can be found in Luque et al. [2011] and Vertés et al. [2010]. Figure 2.10 shows how the chemical structure significantly varies from feedstock to feedstock, depending on the fatty acids contained in the feedstock fat or oil. In the table the x-axis label "C8" for example refers to a fatty acid consisting of a chain of 8 C-atoms, and the ":0" means that the fatty acid does not contain any molecular double bonds.

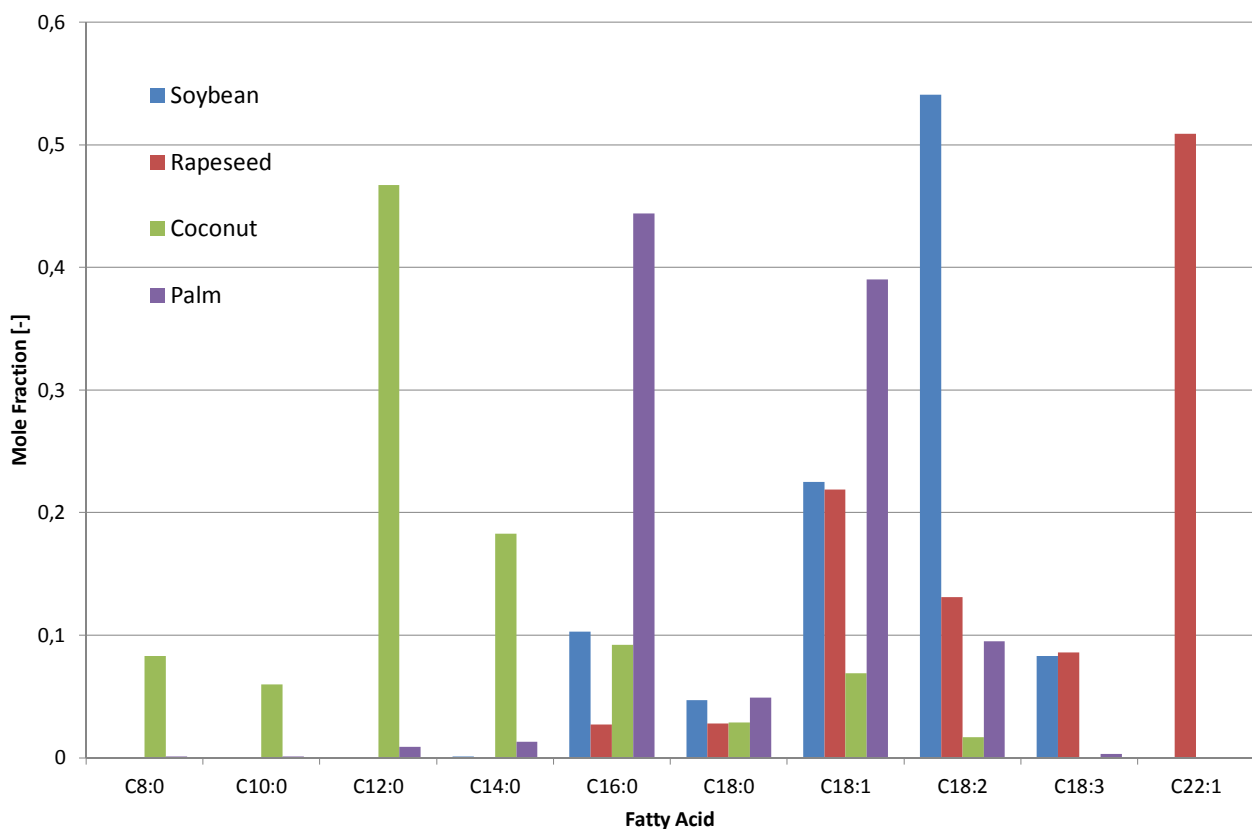


**Figure 2.10:** Biodiesel feedstocks and their fatty acid profiles [McCrary et al., 2007]

FAME has a wide range of similarities with conventional diesel fuel, including the structure, energy value and cetane number [Luque et al., 2011]. It can also be blended with diesel in order to obtain blends of for example 20 % biodiesel in diesel, which is called B20 (B for blend, 20 for the percentage of biodiesel in the diesel). Whereas biodiesel is a good alternative for using in diesel engines in vehicles, biodiesel is not as good a substitute for conventional Jet Fuel. A comparison of conventional jet fuel and FAME can be found in Table 2.3 on the facing page.

**Table 2.3:** Similarities and differences between conventional jet fuel and biodiesel [Hemighaus et al., 2006a] [Hemighaus et al., 2006b] [Luque et al., 2011].

Property	Conventional Jet Fuel	Biodiesel
Chemical structure	C <sub>8</sub> -C <sub>16</sub>	C <sub>12</sub> -C <sub>22</sub>
High Heat of Combustion [MJ/kg]	43.2	40.0
Boiling Range [°C]	180-240	250-450
Freezing Point [°C]	-40	0
Sulfur content, wt% [-]	0.05-0.15	< 0.05
Aromatic content, max vol% [-]	25	0
Viscosity @ 40°C, Cst. [mm <sup>2</sup> /s]	1.2	3.50 - 5.00
Relative Density @ 15°C [kg/m <sup>3</sup> ]	800	860-900

As can be seen from the table there is an obvious difference between the two fuels. The most alarming difference is the difference in low temperature properties. Using biodiesel as an alternative for jet fuel will cause an issue when the plane is at cruise altitude. At these altitudes the plane is subjected to very low temperatures, and thus biodiesel is more likely to reach its freezing point, which then might stop the input of fuel to the jet engines. This is obviously a serious problem, and the main reason why biodiesel is not considered a promising jet fuel alternative. Blends of biodiesel does not solve this problem as the freezing point still is too high. The freezing point of biodiesel can be changed a few degrees Celsius by adding additives [Hemighaus et al., 2006a]. This however is generally not a good trade off, because most additives are unwanted as they are expensive and must be approved before use.

Other properties that do not favor biodiesel as a jet fuel are the lower heat of combustion and chemical structure. The chemical structure influences the thermal stability of the fuel because the higher number of C-atoms might change the atomization and vaporization that occurs in the combustion chamber. Little is known on these subjects and thus a thoroughly investigation must be done to solve the issues correlated with using biodiesel as a jet fuel.

## 2.3 Emissions from Alternative Jet Fuels Compared to Conventional Jet Fuels

One thing that favors the use of biodiesel as a jet fuel is the emissions resulting from combustion of biodiesel. McCrady et al. [2007] states that significant reductions in PM, including soot, HC and CO emissions have been shown for biodiesel compared to similar emissions from conventional jet fuel. EPA [2002] correlated the concentration of biodiesel (blend) in conventional diesel fuel with changes in four common pollutants. The data is based on data from heavy-duty highway engines, and a statistical regression analysis is used to correlate the data. The correlated data can be seen in Figure 2.11 on the next page.

One reason behind this is because biodiesel does not contain any aromatics, which produces more soot, as explained in section 3.3.1 on page 25. The reduction in PM seen on Figure 2.11 is most likely due to the non exciting content of aromatics in biodiesel.

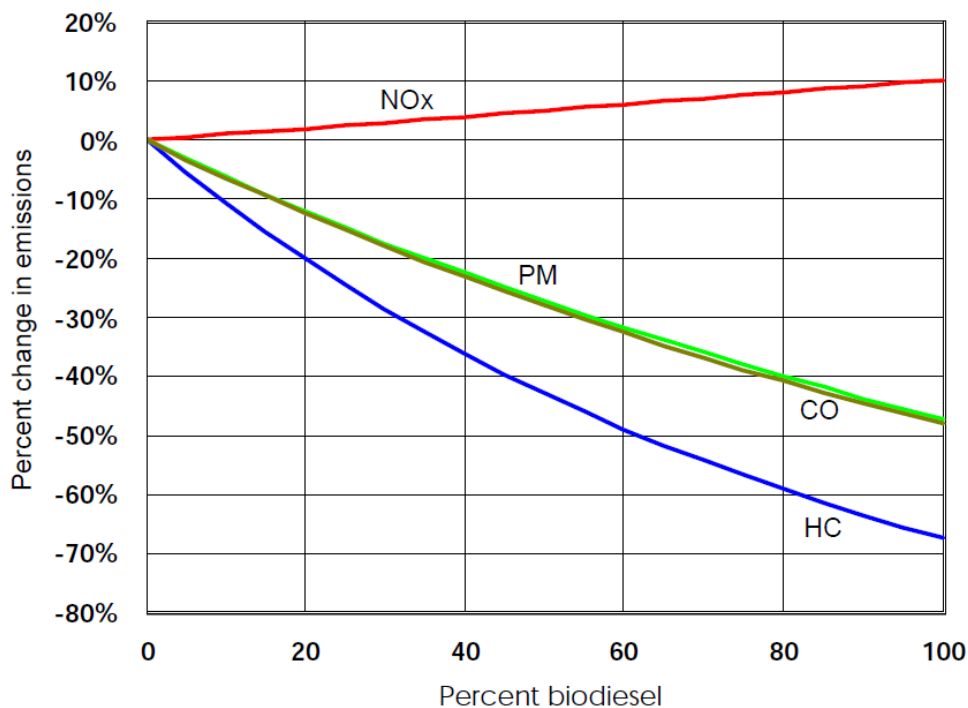


*Figure 2.11: Emission reduction obtained with different blends of biodiesel and diesel [EPA, 2002].*

The use of biodiesel would greatly reduce or even remove the sulfur emitted to the environment, due to the very low, or non existing, content of sulfur. Sulfur is a known precursor in the formation of secondary particles, and essentially also contribute to the formation of acid rain. See section 3.2 on page 18 for more on secondary particles. Sulfur can also be removed from conventional jet fuel through the process of hydrodesulfurization, but this is an expensive process due to the use of catalysts and pure hydrogen.

Another factor that reduces the emissions from biodiesel is the content of oxygen in biodiesel. The presence of oxygen reduces soot emission due to a series of reaction mechanisms, where radicals such as O, OH and HCO are produced because of the oxygenated compounds. These radicals help oxidize CO into CO<sub>2</sub> which reduces the amount of C-atoms available for precursors to soot formation. Large concentrations of OH-radicals in particular help to reduce the inception of soot particles and growth of aromatic rings. [Vertés et al., 2010]. More details are shown in section 3.3.1 on page 21.

**The details of conventional and alternative jet fuels are described in this chapter. The content on aromatics in the fuel is an important factor in the formation of soot from combustion of the fuels. It should be noted that biodiesel will not be considered any further, but only mentioned when appropriate.**

Chapter 2 established knowledge of the compounds found in different jet fuels, and showed the difference in emissions from conventional and alternative fuels. This chapter build on top of this knowledge, and describes in detail what happens when these jet fuels are combusted.

The chapter contains sections on the subjects and processes associated with combustion of hydrocarbons. The first section describes a simplified oxidation scheme of hydrocarbons, assuming complete combustion. The next sections describes the consequences of incomplete combustion, and what implications, in form of particle formation, this has. The final section in this chapter describes the primary combustion particles known as soot, and the complex formation process of these particles.

## 3.1 Hydrocarbon Combustion

Generally seen, the combustion of hydrocarbons can be taken as a process including two steps; creation of CO by break down of the fuel, and oxidation of this CO to CO<sub>2</sub>. This section treats the combustion of hydrocarbons, specifically larger carbon number paraffins.

As described in section 2.1 on page 5 paraffins are straight-changed hydrocarbons, in a saturated state, which is the main part of jet fuel. A general scheme with the key steps of the oxidation process of these paraffins is showed in this section. This excludes the oxidation of methane and ethane however, as these do not follow this generic scheme, but larger paraffins do.

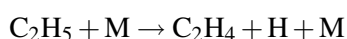
In general simplified formulation, the oxidation scheme initiates with the attack of H- and O- atoms on the paraffins, which break them down to form hydrogen and olefins. These olefins are then oxidized further to H<sub>2</sub> and CO. As a final step the CO oxidizes to CO<sub>2</sub> and H, and it is in this step the major part of the heat during the reactions is released.

This oxidation process can be further broken down, and can hence be showed to follow 8 consecutive steps with propane as example [Turns, 2000]:

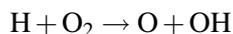
1. As C-C bonds are weaker than H-C bonds, due to a lower bond energy ( $347 \frac{kJ}{mol}$  versus  $413 \frac{kJ}{mol}$  [iSchool, 2004]), these are primarily broken initially.



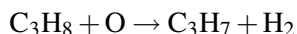
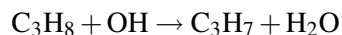
2. The products which are hydrocarbon radicals, then break down again to produce olefins and H-atoms. This reaction is called H-atom abstraction.



3. These H-atoms are then able to start the growth of a radical pool, of among others O and OH.



4. These radical products from step 3, are then able to attack the fuel molecules in new ways.



5. As is in step 2, H-atom abstraction then creates olefins and H-atoms from the hydrocarbon radicals. This process is following the so-called  $\beta$ -scission rule. This rule implies that when a C-C or H-C bond is broken, the bond broken must be the one, one bond away from the radical site. This is because the unpaired electron strengthens the bonds around it, but weakens the bond one place further away.

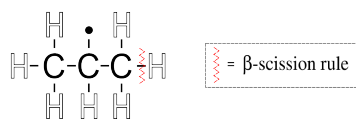
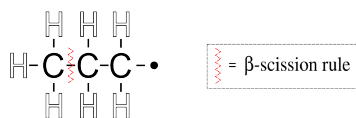
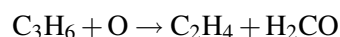
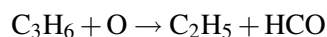


**Figure 3.1:** H-atom abstraction by the  $\beta$ -scission rule. Inspired by [Turns, 2000].

6. Then the olefins which was created in step 2 and 5 is initially oxidized by an attack of O-atoms. This forms HCO (formyl radicals) and  $\text{H}_2\text{CO}$  (formaldehyde)



7. Then oxidation of formaldehyde, methyl radicals and, methylene occurs. Each of these oxidation reactions has CO as product.
8. The CO then oxidizes according to the CO oxidation mechanism shown in Turns [2000], but where the most important reaction is shown below.



As mentioned in Turns [2000] the oxidation scheme for higher paraffins is very complex, and it is still under research.

To further describe the concept of radicals, these are atoms or molecules which possess at least one unpaired electron, and hence they are very reactive and have a very important role in combustion. The majority of molecules has an even number of electrons, as each covalent bond between two atoms in a molecule shares an electron pair. In radicals one of these covalent bonds are broken. Biradicals with two unpaired electrons also

exists. Here each of the unpaired electrons is on a different atom. [Condra, 2010]. It is common to mark the location of the unpaired electron on a molecule as a dot, as seen in Figure 3.2.

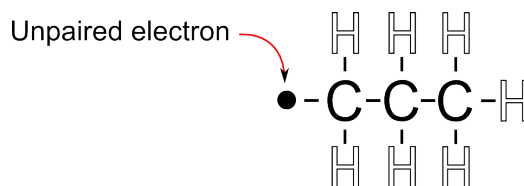


**Figure 3.2:** The common way to show a radical side on a molecule, in this case an n-Propyl radical.

The importance of radicals can be illustrated with very simple example by looking on Figure 3.3.

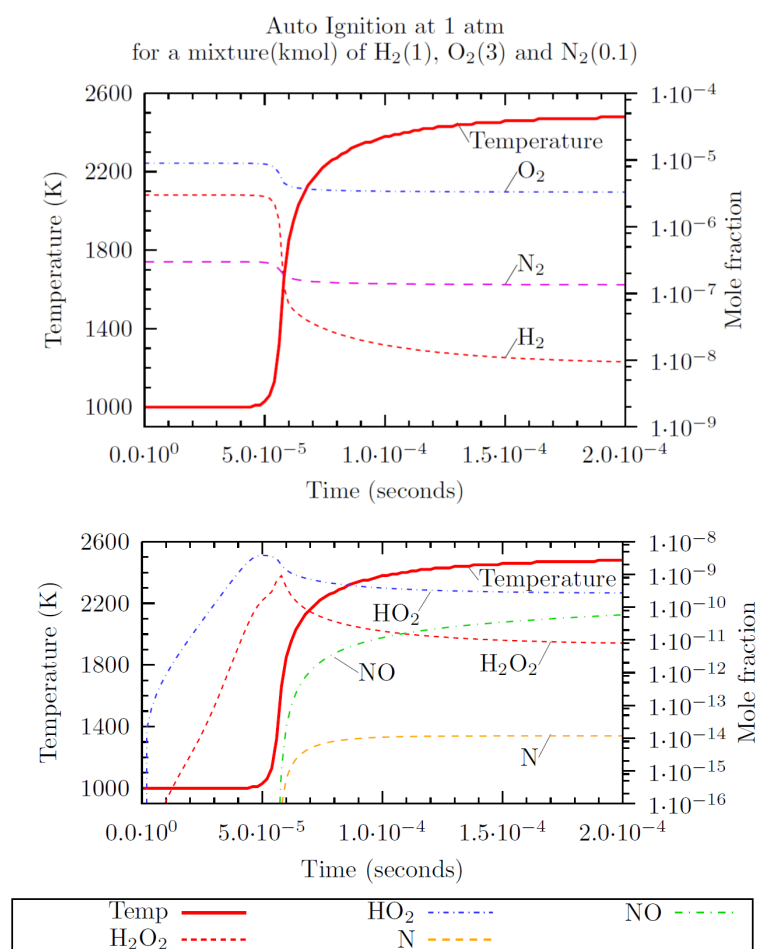


**Figure 3.3:** Figure illustrating the importance of radicals.[Condra, 2010]

Here a combustion process of H<sub>2</sub> with air is modelled in Chemkin. The important thing to note on the bottom figure is that for example looking at the perhydroxyl radical, HO<sub>2</sub>, it is formed in small concentrations even before the autoignition of H<sub>2</sub> happens, and the temperature rises. It is the radicals that essentially initiates and "pushes" the combustion process as intermediate products, hence the presence of these are of utter importance for the reactions to proceed because of their willingness to react.

## 3.2 Particles

Particles are formed during the incomplete combustion of hydrocarbon fuels under fuel-rich conditions. This section describes the terms and sizes of particles. An overview of the health related problems caused by these particles are given, along with a size distribution of the emitted particles.

Particles are defined in terms of their diameter, and are divided in three size categories: UFPs ( $PM_{0.1}$ ), fine particles ( $PM_{2.5}$ ) and coarse particles ( $PM_{10}$ ) [Palmgren et al., 2009]. Other terminology used to describe the three particle size categories are *nucleation mode*, *accumulation mode* and *coarse mode*. Particles in all ranges of sizes are emitted to the air by both natural processes and all kinds of human activities [Palmgren et al., 2009], where combustion processes are responsible for the main emission of fine and ultra fine particles [Morawska et al., 2004]. These particles are responsible for several health related problems as they attach to the lungs after being inhaled. Smaller particles can be deposited further into the lungs compared to larger particles which results in more severe health related problems [Morawska et al., 2004]. To mention a few associated health related problems: Blood clots, heart disease, premature death, lung cancer, bronchitis and asthma [Press-Kristensen, 2011].

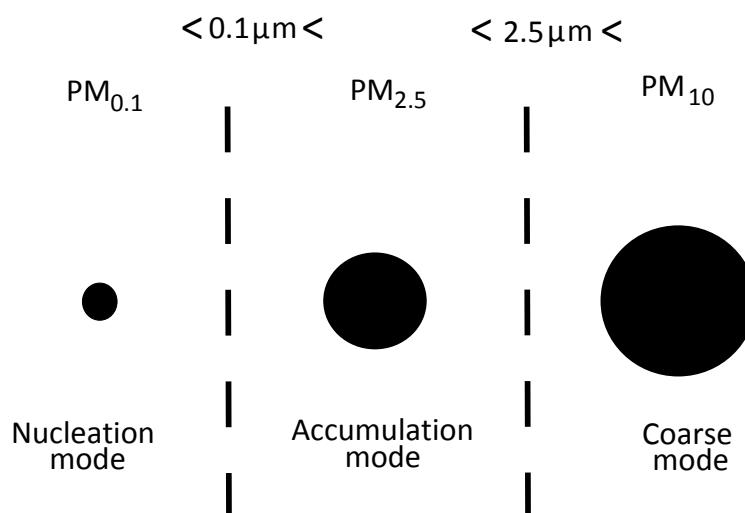


**Figure 3.4:** A conceptual sketch of the different particle mode sizes.

Within recent years two baggage handlers in CPH have been diagnosed with cancer, most likely due to the daily exposure to UFPs [Campbell and Graham, 2012]. A rough estimate was made by [Press-Kristensen, 2011] who estimated that a baggage handler during one hour of work inhales 45 billion particles. The large amount of particles are emitted from the aeroengines and APUs of the planes located on and around the tarmac, as explained in Chapter 1. Also explained in the same chapter is the fact that there exists no emission limits for UFPs, but only for the larger particles. Press-Kristensen states that limits are needed, and even though no limits exist it is still possible to limit the emission of UFPs, hinting that more should be done on this matter.

The particle size distribution found in CPH is shown in Figure 3.5 on the facing page.

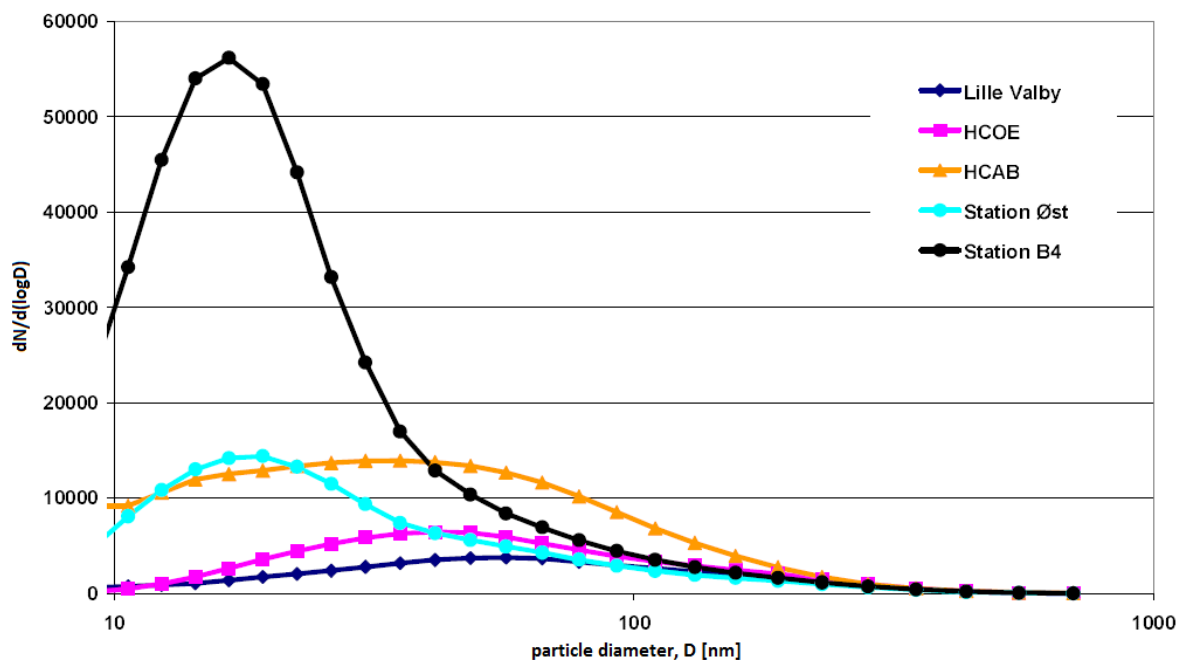


**Figure 3.5:** Particle size distribution [Ellermann et al., 2011].  $N$  is the number of particles, and  $D$  is the diameter.

UFPs accounts for most of the particle numbers in the airborne particulate matter, but a negligible size of the total mass. Larger particles on the other hand accounts for most of the total mass, though not significant in amount. The larger amount of UFPs further increases the risk for health related problems.

As the exhaust gas from an aeroengine is cooled in the ambient air, a number of reactions occur. These reactions are important in terms of emissions and particle sizes and numbers [Morawska et al., 2004]. Among other chemical reactions, oxidation of for example soot particles will change their size and decreases the total amount emitted [Flagan and Seinfeld, 1988]. The formation of sulfuric acid also starts occurring as the exhaust gas mixes with the ambient air and  $\text{SO}_2$  from the combustion chamber is oxidized into  $\text{SO}_3$ , then hydrated into gaseous  $\text{H}_2\text{SO}_4$  before condensating into liquid  $\text{H}_2\text{SO}_4$  [Sander et al., 1984] [Glassman, 1996]. The formation of aerosols (particles and/or liquid droplets and gas together) in aircraft wakes (the plume) have been investigated by different authors who describes some of the chemical reactions occurring in that mixing zone [Kärcher and Fahey, 1997] [Kircher et al., 1998].

Particles are divided into two categories; Primary particles (emitted directly from the engine) and secondary particles (PM formed in the atmosphere by chemical reactions of gases, as described above). The primary particles mainly consists of soot formed under fuel-rich combustion of HCs. The very complex process of soot formation involving different chemical and physical reactions are described in the following section. Secondary particles are formed from chemical reactions of gas-phase products which either condense or nucleate to form new particles. They usually consists of ammonium sulfate, sulfuric acid, nitrates and organic compounds, and also trace metals like for example iron, magnesium and zinc. Condensation of gas-phase onto the existing ambient particles are known as heterogeneous nucleation, while nucleation of the gas-phase is called homogeneous nucleation. In homogeneous nucleation it is possible that both the mass and number of particles increase, while for heterogeneous nucleation only the mass increases. [Morawska et al., 2004]

Because of the different chemical reactions leading to the formation of secondary particles the composition of these particles change significantly from place to place. The fuel source, and local conditions also plays a key role on the particle composition. Generally secondary particles constitute of sulfuric acid, ammonium sulfate, nitrates and organic compounds, as well as a series of trace metals like iron, magnesium, zinc, etc. [Morawska et al., 2004]. **Secondary particles are beyond the scope of this report and the presence of sulfur, and other compounds than H and C, are not considered any further.**

### 3.3 Soot

As described in the previous section soot are primary particles emitted from the combustion of hydrocarbon fuels. This section gives a detailed description of soot, along with a detailed physical explanation of the formation process of soot.

Soot is normally a black or dark colored carbonaceous solid material, and is the result of an incomplete combustion of hydrocarbon fuels. Soot is not uniquely defined, as its composition varies with the type of fuel used and the overall combustion process. However the main compound of a soot particle is carbon and about 10 mole % of it is hydrogen [Haynes and Wagner, 1981]. Glassman [1996] states that at least 1 wt. % of soot is hydrogen, which is a relatively large amount on an atomic basis, and correlates to a chemical formula around  $C_8H$ . Soot particles contain more hydrogen in the initial steps of the formation process, and as the formation process proceeds most of the hydrogen is abstracted. The soot particles have a roughly spherical shape with a diameter between  $0.01 - 0.2 \mu m$ , with most between  $0.01-0.05 \mu m$  [Flagan and Seinfeld, 1988]. Soot particles are UFPs because of their size, which through agglomeration grows to larger particles, as described in the following section.

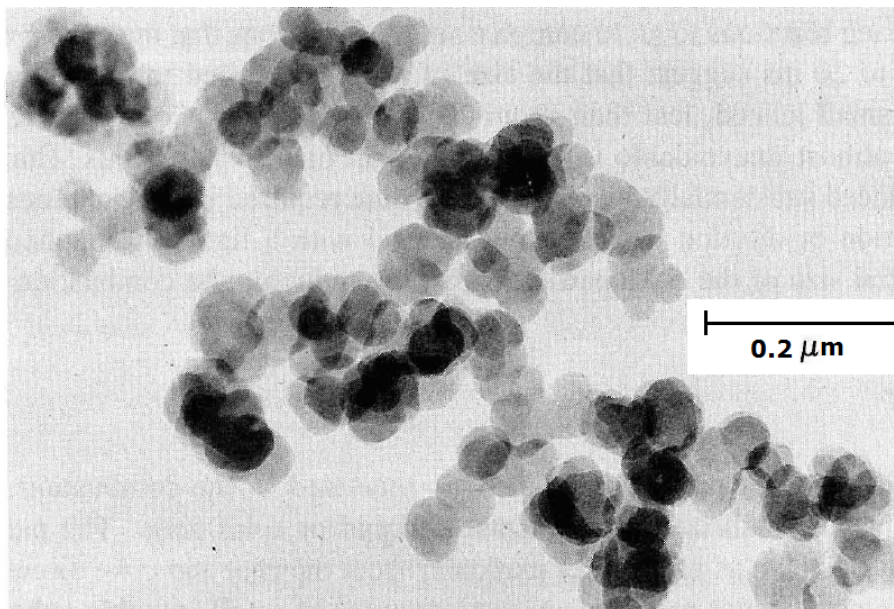


*Figure 3.6: Spherical shaped soot particles and their size [Flagan and Seinfeld, 1988].*

Soot is generally not wanted as a combustion product and the formation is undesirable for several reasons:

- Soot particles are UFPs and can thus cause human health problems and mortality, as described in Sec-

tion 3.2 on page 18.

- When emitted to the atmosphere, soot particles absorb solar radiation, and can thus heat or cool the earth's surface by either being deposited on the surface or located in the atmosphere [White, 2011] [Ramanathan et al., 2005].
- Soot particles can cause severe damage to the turbine blades in a gas turbine engine. Soot can also be deposited on engine walls and radiant heat loss to the particles can lead to hot spots in the engine [Glassman, 1996]

### 3.3.1 Soot Formation

The formation of soot is described by multiple authors, *e.g.* Glassman [1996], Haynes and Wagner [1981], Kalaskar [2009] and Richter and Howard [2000]. The authors define a different numbers of steps in the formation process, because some authors include steps which others does not. However the overall formation process is similarly described by all authors, and is today the widely accepted process of soot formation. Although the authors agree on the overall formation process, many details in soot formation are still not fully understood. Depending on whether the fuel is aliphatic or aromatic, the formation is either slower or faster. Aliphatic fuels are acyclic or cyclic, non-aromatic carbon compounds, and are the opposite of aromatic compounds. Soot is formed by the following steps, as described in detail by Richter and Howard [2000]. If the fuel is aromatic the first step is not relevant, because the fuel already has an aromatic ring. An aromatic ring (benzene,  $C_6H_6$ , or phenyl,  $C_6H_5$ ) is the start point for the growth of a soot particle, and this ring must be formed in order for a soot particle to be formed. Details of the formation process is given throughout this section.

1. *For Aliphatic hydrocarbons only:* The first aromatic ring must be formed from decomposition/pyrolysis of the given fuel. This happens through cyclization (the formation of a ring in a chemical compound) of benzene/phenyl precursors.
2. **Growth of first aromatic ring:** The first aromatic ring, *i.e.* benzene or phenyl, grows by the addition of smaller gas phase species. 2-ring compounds, naphthalenes, are first formed by this addition, followed by larger, heavier 3- or 4-ring compounds, termed Polycyclic Aromatic Hydrocarbons (PAH).
3. **Formation of particle nuclei by nucleation:** The heavy ring compounds/PAH molecules are converted to nuclei (initial, growing soot particles) by nucleation, which arranges the molecules in a pattern with the characteristics of a crystalline solid (a structured and strong pattern). This form a nucleus on which other particles can be deposited, which then makes the nucleus grow.
4. **Particle nuclei agglomeration:** The newly formed nuclei increase in size and mass by agglomeration, surface growth by addition, of gas phase species like acetylene  $C_2H_2$  and various  $C_3$  and  $C_4$  species, as well as radicals of PAHs. This increases the size of the nuclei and the number of nuclei is kept constant.
5. **Particle nuclei coagulation:** Further increase in mass happens through coagulation (collision and coalescence) between the nuclei (now mature soot particle). Throughout the collisions the nuclei size increase and the number of nuclei decrease. The total nuclei growth is a combination of the surface growth and collision. This is the solid material known as soot.

The formation process is illustrated on Figure 3.7, and shows the slow and fast formation pathways of soot. The slow formation pathways for aliphatic fuels, like for example biodiesel, results in lower emissions of soot. This is most likely due to that the formation pathway of soot particles from aliphatic fuels are slower, and thus not all of the chemical reactions needed to form soot are completed before the particles leave the favorable soot conditions in the combustion chamber.

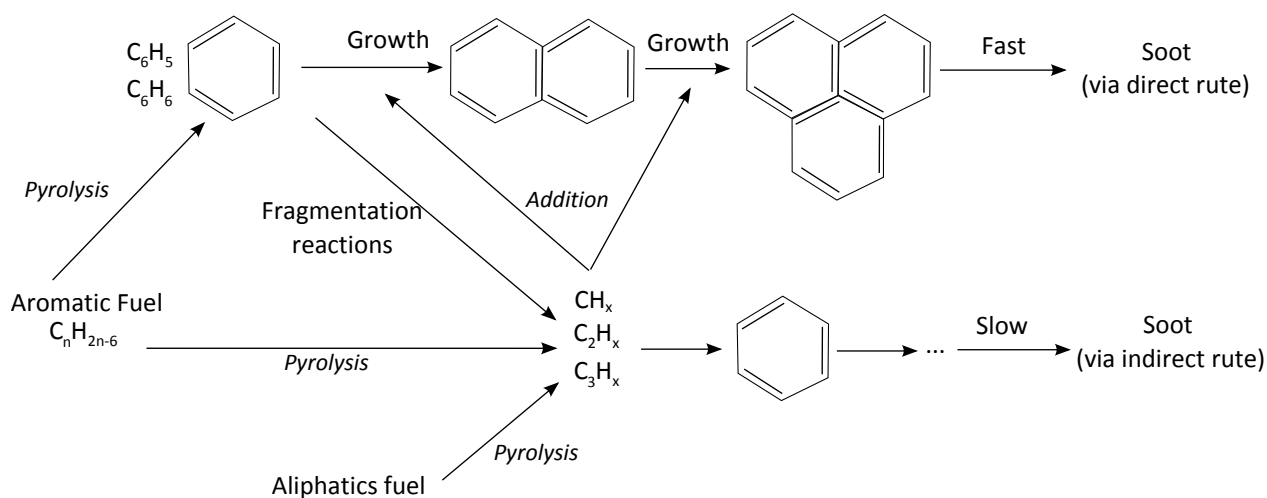


**Figure 3.7:** Simplified scheme for the formation of soot. Inspired by [Flagan and Seinfeld, 1988].

When the soot particles are formed two things can happen to it depending on the conditions in the combustion chamber:

If soot is under pyrolytic conditions, *i.e.* high temperature and low oxygen concentrations, in a high residence time it will decompose and convert into a material with a structure similar to graphite. The process decreases the mass of the particle, but the overall number of particles are kept constant.

When the soot particles mix with fuel-lean gases oxidation of the soot particles can occur, in which case they will burn up. During the oxidation process the mass of PAH and soot material is decreased as the soot is burned up. This happens because CO and CO<sub>2</sub> are formed from the soot particles reacting with the oxidation reactants OH, O and O<sub>2</sub>. Among the oxidation reactants OH contributes the most to oxidation, especially under fuel-rich combustion, while O<sub>2</sub> dominates under fuel-lean combustion. Thus the actual emitted mass fraction of soot is only a small part of the soot particles formed.

### Soot Precursors

As indirectly explained in the previous section the number of reactions which describe the formation of soot is extensive. The formation of the first aromatic ring is a key-point in soot formation. This process alone (for aliphatic fuels at least) consists of a large number of reactions. Not only does benzene and phenyl have their own precursors and reactions, but precursors to each of these also have their own reactions. Richter and Howard [2000] describes several benzene formation paths investigated by different authors. The details of benzene formation is still not clear. For lower temperatures benzene is formed primarily from the following formation:

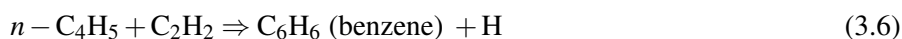




At different temperatures benzene can also be formed by recombination of, for example, propargyl ( $\text{C}_3\text{H}_3$ ) as described in Miller and Melius [1992] by the following reactions:



According to Miller and Melius [1992] the two most cited reactions that leads to the formation of the first aromatic ring are:



and



where  $\text{C}_3\text{H}_3$  and its isomers for example, are formed from the reactions:



The abovementioned reactions are just examples to show some of the intermediate species for the formation of benzene. Other pathways to benzene also exist, for example, from different  $\text{C}_4$  species ( $\text{C}_4\text{H}_3$  and  $\text{C}_4\text{H}_5$ ) and acetylene ( $\text{C}_2\text{H}_2$ ) [Richter and Howard, 2000]. For more details on benzene formation see Richter and Howard

[2000] who made an excellent review on this topic. The authors conclude and emphasize that each elementary reaction step are important for PAH formation, so even small uncertainties in the different thermodynamic data, for example, activation energy and reaction rates, can limit the accuracy. Also interest in accurately predicting each reaction step has increased the past years in order to control PAH and soot emissions from various engines.

It is clear that just the formation of benzene includes a lot of reactions. As described in the formation process of soot formation, the first aromatic ring grow to form naphthalenes (two ring compounds) and eventually larger PAHs (3 or 4 rings). PAHs are the primary precursors for soot particles. Growth species for benzene to form PAHs are *e.g.*  $C_2H_2$  (acetylene),  $C_2H_4$  (Ethylene), and isomers of  $C_3H_3$ , *e.g.*  $CH_3C=CH$  (propyne) and  $HC\equiv C-CH_2$  (propargyl), and isomers of  $C_4H_4$ . [Wheeler et al., 2007]. The growth of benzene to form naphthalenes can be seen in Figure 3.8.

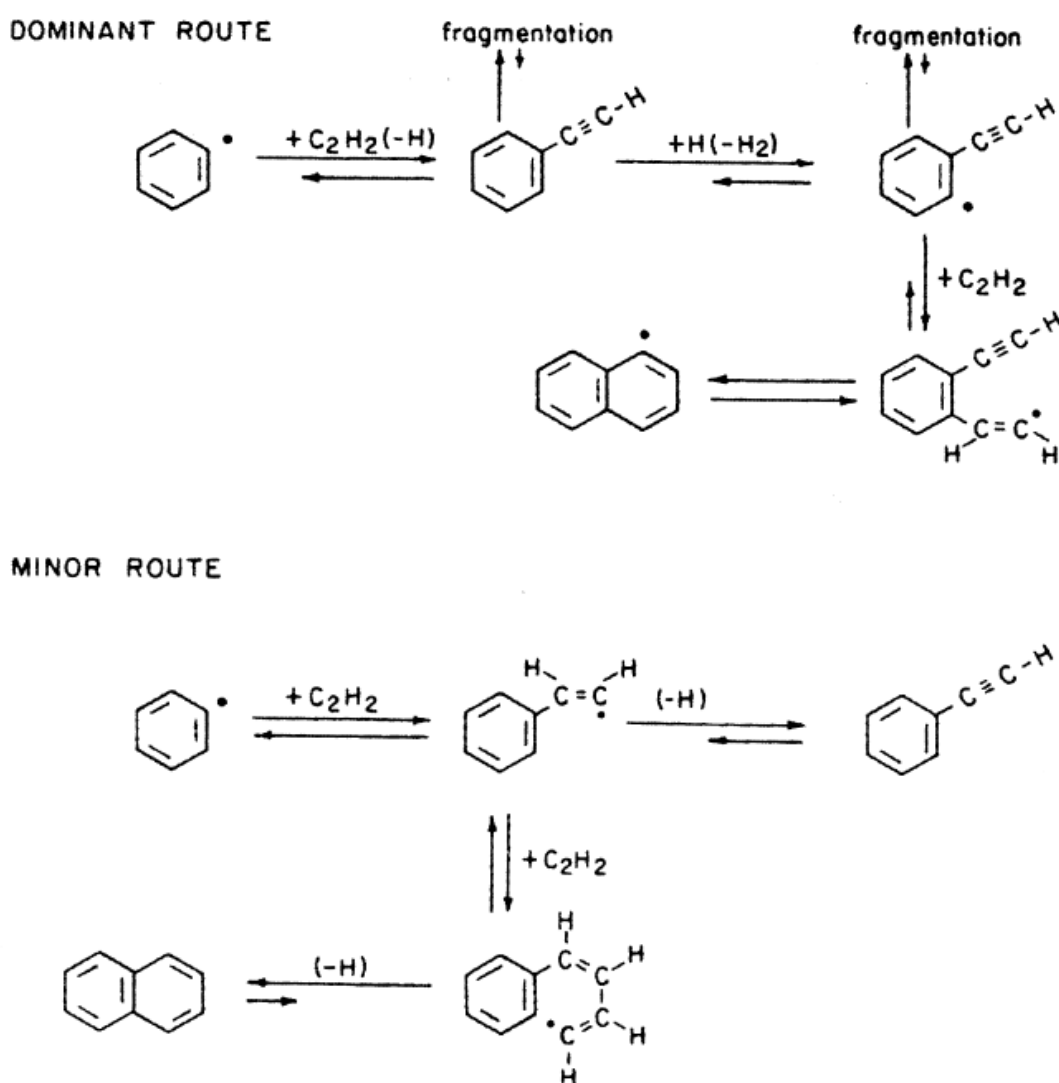


**Figure 3.8:** The growth of benzene to form larger PAHs [Richter and Howard, 2000].

A detailed formation scheme for multi-ring PAHs from the first aromatic ring can be seen in Figure 3.9 on the next page, and is shown to give the reader an impression of the many possible reactions in the formation of

PAHs and soot.

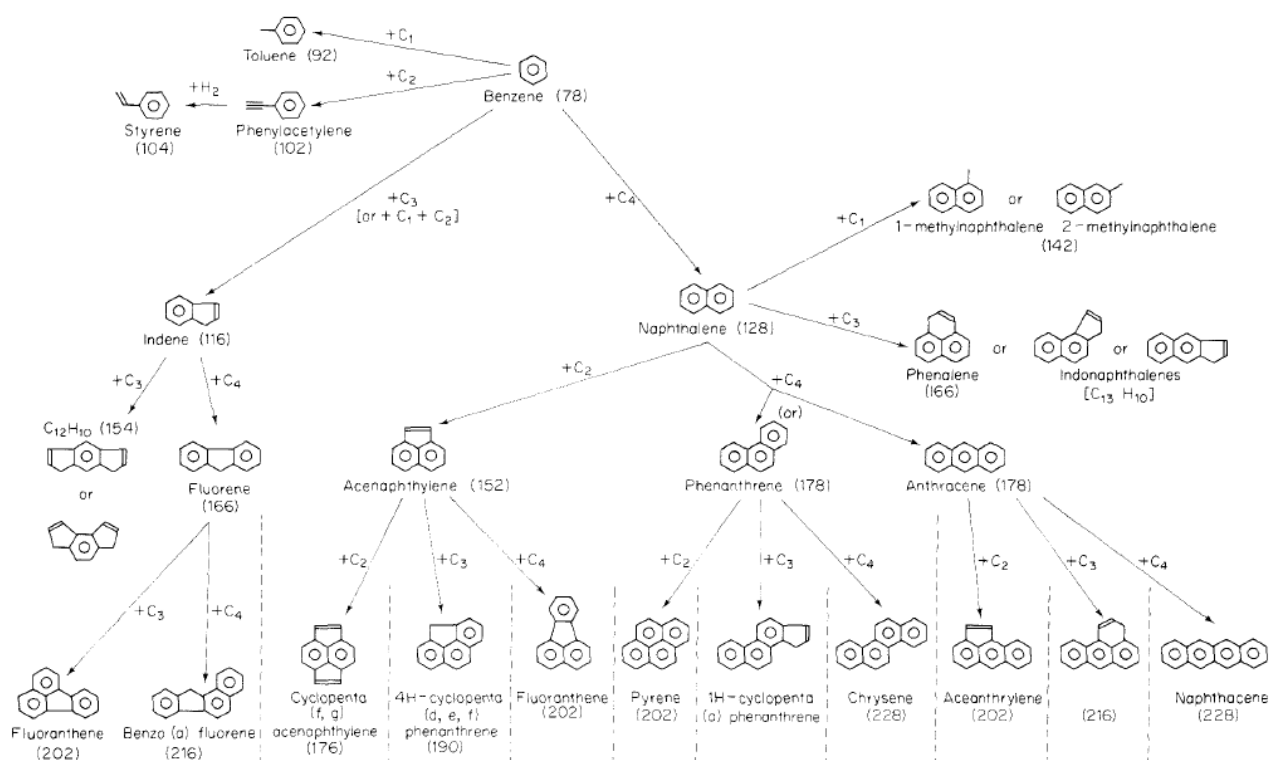


**Figure 3.9:** The formation and growth of PAHs starting from the first aromatic rings [Flagan and Seinfeld, 1988].

### Conditions Favoring Soot Formation

In order to limit the formation of soot it is necessary to know which conditions favor soot formation. Several parameters influence the formation and behavior of soot; fuel type, temperature, pressure, premixed or non-premixed combustion and presence of additives. As explained above the soot tendency of a fuel varies with the composition of the fuel. Aromatics have a higher tendency to soot (faster formation of soot) than aliphatics. According to the ability to form soot this can be shown as: naphthalenes > benzenes > aliphatics. [Flagan and Seinfeld, 1988]. This fact is established by Dagaut and Cathonnet [2005] who comments on the aromatic limits in jet fuel:

***"Fuels with high aromatics contents, especially polyaromatics, produce more soot. This is why both the total aromatic content is limited to 22–25% and the naphthalene content to 3% in volume. Practically, the aromatic content of JP-8 varies between 10 and 25% with a mean at 18% in volume"***

In non-premixed combustors, for example aeroengines, soot is only formed in fuel-rich zones. [Haynes and Wagner, 1981] [Flagan and Seinfeld, 1988]. But even in fuel-lean, non-premixed combustors there are fuel-rich zones or points in which significant soot formation occurs due to improper mixing, but also especially around the formed flame.

For premixed combustion the higher temperature the lower sooting tendency. This is due to the presence of oxygen in the pyrolysis zone which oxidizes the soot. Millikan [1962] showed that the oxidation rate increases

faster than the pyrolysis rate, which then decreases soot formation. For non-premixed combustion however, the higher temperature the higher tendency to soot because less oxygen usually is present in the pyrolysis zone for this type of combustion [Millikan, 1962].

According to Haynes and Wagner [1981] and Glassman [1996] soot formation in spray flames is favored with increased pressure in the combustor. Likewise low pressure in the combustor reduces soot formation.

For premixed combustion the fuel and oxidizer is mixed in advance, and thus the gradients between fuel-rich spots and fuel-lean spots are smaller compared to those in non-premixed combustion. Therefore mixing plays a bigger role for the sooting formation in non-premixed combustion [Haynes and Wagner, 1981]. Poor mixing allows soot to survive even if enough oxygen is present to fully consume it, as explained above. Higher mixing rates might not prevent soot formation, but it enhances the opportunity for the soot formed early in the flame to burn/oxidize [Flagan and Seinfeld, 1988].

Some additives used in the fuel can reduce the output of soot. Especially metals and organometallic compounds like ferrocene, barium, strontium and calcium. These metals share a common property; They have a large ionization potential, which reduce the soot particle size and volume fraction. Because of this agglomeration decreases, and as the (now) smaller particles goes through the flame flame, the particle burnup is increased. These additives thus help reduce the buildup of soot, but no evidence exists that they affect formation of soot precursors or soot. [Glassman, 1996]

The angle at which fuel is sprayed into the combustion chamber also significantly influences the amount of soot formed. For low cone angles the fuel is more concentrated and thus more fuel-rich. Using a larger cone angle will reduce soot formation, as there is a better chance of mixing between the fuel and oxydizer. [Haynes and Wagner, 1981].

Hayashi et al. [2010] studied the effects of fuel droplet size on soot formation in a laminar counterflow spray flame both numerically and experimentally. The study showed that small droplet sizes of the injected fuel will cause faster evaporation of the fuel. The smaller droplets have a lower spray penetration compared to larger droplets, which in turn will create a rich primary combustion zone that thus leads to increased soot formation. It takes longer for larger droplets to evaporate, and some large droplets might not get evaporated in the combustion zone, if the residence time is not high enough. Hayashi et al. observed immediate reduction in the formation of soot as the particle size increases, which they explained by the formation of groups of unburnt particles in the combustion zone.

**In this chapter knowledge of hydrocarbon combustion and particles and their size distribution is obtained. The different formation paths of soot and the precursors are also investigated, as well as the conditions which enhances this formation. On the basis of this, a problem description is formulated as seen on the next page.**

The previous sections focused on conventional and alternative jet fuels. This included their chemical composition, the emissions resulting from combustion, and chemical reaction mechanisms during the combustion process in an aeroengine. Furthermore particle formation, specifically soot formation, was investigated. As it is shown by the work done by Copenhagen Airport and DMU, UFPs emitted by commercial airplanes can cause severe health related hazards and should be avoided, it is an area of interest to investigate how these particles are formed. On the basis of the previous chapters, considering the particle formation, it is found that:

- Primary particles, which are mainly soot, are formed in high temperature and fuel-rich zones of the combustion chamber.
- Soot particles are formed from nucleation of PAHs which forms nuclei that through agglomeration and coagulation increases the size of the soot particles.
- The presense of soot precursors facilitate soot formation.
- Soot particle contain C-atoms and H-atoms, in a ratio similar to  $C_8H$ .
- Soot particles can be classified as UFPs due to their size.

It is of great interest to map the formation process of UFPs emitted from aeroengines. The aim of this project is to numerically model the formation of UFPs from combustion of commercial jet fuel, *i.e.* Jet A using ANSYS Fluent. To numerically model the formation of UFPs, and the various small radicals and volatile particles associated with these, a reaction mechanism of the combustion of Jet A is required. The use of a reaction mechanism is described in detail in Chapter 5 on page 29, where a reduced mechanism is chosen to be used in the CFD model. The main focus of the numerical model is to couple the numerical calculation in ANSYS Fluent with the kinetics of the chemical reactions of soot formation via the reduced reaction mechanism.

Since soot particles are classified as UFPs, and the fact that only particles consisting of C and H-atoms are considered, soot particles are a viable source of UFP formation, which is what is wanted to model. It is assumed that if soot precursors are located in the same zone, and that the favorable conditions mentioned above are present, soot, and thereby UFPs, are formed.

## 4.1 Project delimitation

The project is delimited only to look on what happens inside the combustion chamber, and thus the formation of primary particles, *i.e.* soot particles and UFPs, happening here. This means that the particle formation in the exhaust gas outside the combustion chamber is not considered, which is why the formation of secondary particles is not considered in this work. As written in section 3.2 on page 18 the project is delimited to only consider particles that include C-atoms and H-atoms, and thus species such like sulfur is not considered.



As mentioned in the Project Description a reduced mechanism is used in the CFD model of the combustion of Jet A. This chapter describes how some combustion processes usually are modeled using reaction mechanisms and so called surrogate fuels. The reduced reaction mechanism used in the CFD model is presented in this chapter, which is chosen based on a discussion of the advantages and disadvantages of using a reduced mechanism compared to a detailed mechanism.

## 5.1 Surrogate Fuels

Some authors have modeled the combustion process of different jet fuels in order to predict, for example, the emission performance of the fuels. Due to the high complexity of the composition of the jet fuels many authors have chosen a more simplified approach. Jet fuel is modeled by using a so-called surrogate fuel, which has a more simplified composition compared to the real fuel, *i.e.* fewer components. The advantage of surrogate fuels is that the combustion characteristics of the real fuel can be modeled in a satisfying way using a simplified mixture of fuels.

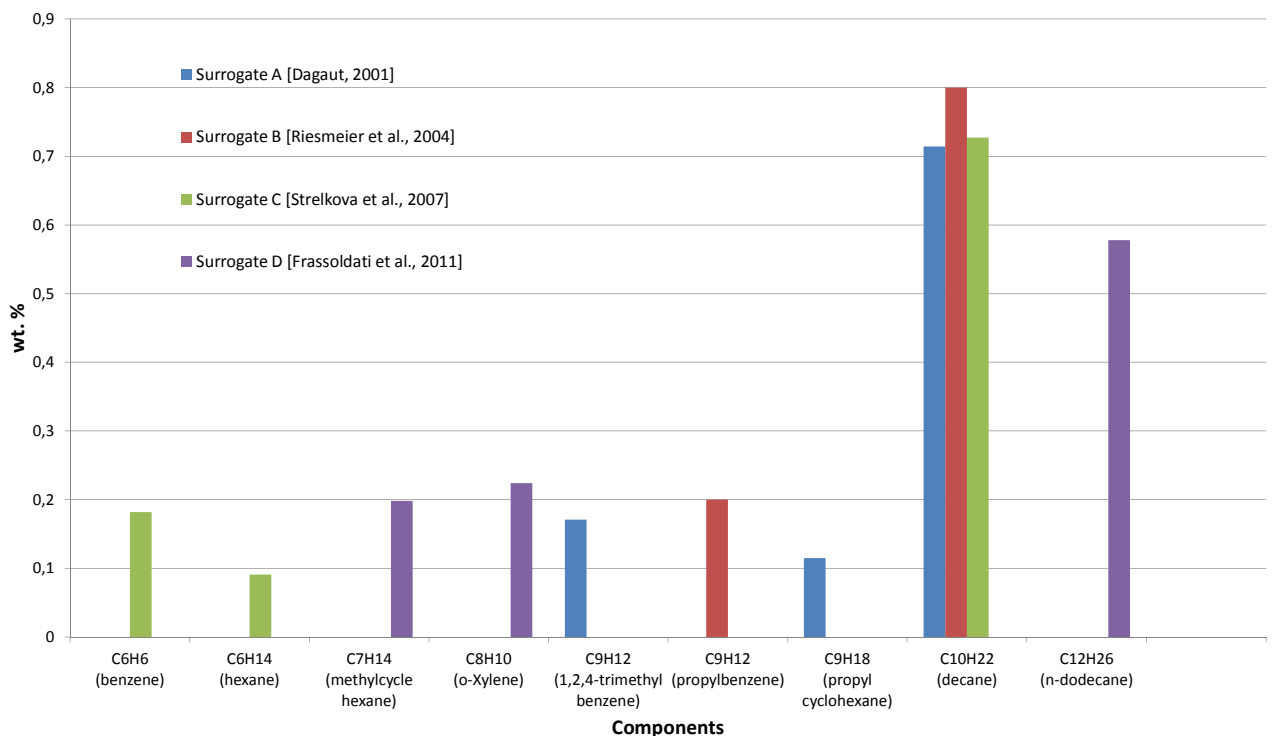


**Figure 5.1:** The composition of different surrogate fuels used by different authors.

Different surrogate fuels used by different authors can be seen in Figure 5.1 on the preceding page. [Dagaut, 2001] modeled the combustion of kerosene using "Surrogate A" with the composition seen in Figure 5.1. The modeling showed good representation of the kerosene oxidation, and was in very good agreement with experiments conducted. Riesmeier et al. [2004] made use of a flamelet model to CFD model kerosene using "Surrogate B", which proved to model kerosene in a satisfying manner. Strelkova et al. [2007] also chose a surrogate fuel approach when CFD modeling the combustion of Jet A aviation fuel. The reduced mechanism of a Jet A, "Surrogate C", showed good agreement when compared with the results obtained from a detailed mechanism of the Jet A aviation fuel. A recent study compared different surrogate fuels of kerosene (similar to Jet-A) where the results of using "Surrogate D" emulated the results of kerosene in a similar way [Frassoldati et al., 2011].

## 5.2 Reaction Mechanisms

Reaction mechanisms describe the elemental reactions of a chemical reaction step-wise. Reaction mechanisms are generally divided into three categories; global, single-step or multi-step mechanisms. These reactions can then be described as either simplified or detailed. The degree of detail varies from one step to several hundreds or thousands steps, as implied by the three categories. Global mechanisms are the most simplified of the three categories, as they often only contain a single elemental reaction that approximates the destruction of the reactants and formation of products. They do not offer a description of the intermediate reactions that actually happens.

Whether to choose a global reaction mechanism, a very detailed mechanism or a simplified mechanism, depends on the application in which the mechanism is used. Flagan and Seinfeld [1988] describes this by pointing out that global mechanisms excel at, for example, describing the net rate of heat release during a combustion process because the minor species / intermediates are of little interest. On the other hand more detailed mechanisms are very useful when pollutant formation is described as the minor species in a far larger degree influence the final outcome. At the same time the computational effort needed to solve global mechanism are way smaller compared to what is needed in the detailed mechanisms. Therefore it is really a trade off between computational effort and degree of detail.

A third thing that influences the choice of reaction mechanism is what it should describe. When describing, for example hydrocarbon fuel, the challenge is that usually the exact composition of the fuel is unknown. Only rarely is the composition fully described in which case a detailed reaction mechanism directly can be used [Flagan and Seinfeld, 1988].

Also when modeling a detailed multi-step mechanism the reaction rates associated with each step are not always known, and these must thus be estimated. The detailed mechanism gives a more correct picture of the chemical reactions, but the estimations gives the final result an uncertainty, and the final results might not be all trustworthy. In cases like this it might be better to use a more simple mechanism where the reaction rates are known, which then gives a result that might not totally correspond to reality, but has less uncertainty.

A good way of determining whether a reduced mechanism represents a detailed mechanism is by comparing the ignition delay of the two mechanism, using a software package like the Cantera. If the ignition delay is similar for the two mechanism it can be said that the reduced mechanism corresponds well to the detailed mechanism.

## 5.3 Choosing a Reduced Chemical Reaction Mechanism

From section 5.1 on page 29 it was described how different authors have obtained reasonable result when using a surrogate fuel to model a real jet fuel. This encourages the use of a similar approach. Using a surrogate fuel to model Jet A simplifies the reaction mechanism as well as saves computational time.

As the authors of this report have no experience in creating a chemical mechanism, and that work in itself is beyond the scope of this project, it was chosen to use a reaction mechanism obtained from the literature. It proved to be more difficult than first imagined to find a reduced mechanism of Jet A combustion, which models both the combustion of Jet A as well as soot formation and oxidation. Most reaction mechanisms of Jet A combustion are very detailed mechanisms, consisting of several hundreds or thousands reactions, and does only describe either the combustion of Jet A or the formation/oxidation of PAHs/soot. It was not possible to find a reduced reaction mechanism describing both the combustion of Jet A and the formation/oxidation of PAHs/soot.

It is therefore considered what is important in the modeling part when choosing which reduced mechanism to use to model the combustion of Jet A. In order to describe the formation of soot correct, the correct combustion characteristics must be present, otherwise the soot formation is not correct. Therefore the following things are chosen as important for the reaction mechanism that is chosen:

1. The surrogate fuel must resemble the real fuel
2. The combustion characteristics of the surrogate must correspond to the real fuel
3. The degree of detail; It is computational advantageous and necessary to use a reduced number of reactions and species

With these things in mind a reduced mechanism of combustion of Jet A (described/simplified by the chemical formula  $C_{12}H_{23}$ ) with 26 reactions and 17 species was found in Su and Zhou [1999]. This mechanism however is considered to be too simple since a single global reaction is used to describe the pyrolysis steps involved in chemical reactions of Jet A. Also the mechanism is based on the mechanism of propane except for the single global reaction, with the assumption that most HC fuels react in almost the same way.

A reduced mechanism of a surrogate Jet A fuel with 38 reactions 24 species for use in CFD simulations of gas turbine combustors is proposed by Strelkova et al. [2007]. This mechanism is reduced from a detailed mechanism of the surrogate fuel with 417 reactions and 71 species, and is thus considered more accurate than the mechanism from Su and Zhou [1999]. Since no other reduced mechanism of Jet A was found it was chosen to use the reduced mechanism from Strelkova et al. [2007], which is described in detail in the following section.

### 5.3.1 Reduced Mechanism of Jet A Surrogate

The reduced mechanism of surrogate Jet A (consisting of 72.7 wt% decane + 9.1 wt% hexane + 18.2 wt% benzene) from Strelkova et al. [2007] is obtained from a relatively detailed mechanism of Jet A surrogate with 417 elemental reversible reactions and 71 components. The detailed mechanism is also developed by Strelkova et al. [2007] on the basis of other papers focusing on n-decane, n-hexane and benzene combustion mechanism development. These can all be seen in Strelkova et al. [2007]. Furthermore the thermodynamic data is obtained from [Burcat, 2006]. The mechanism is developed to model the combustion and detonation of Jet A, and does not describe the formation or oxidation of PAHs or soot. It is constructed by a 3-level approach which will

not be elaborated further in this project, but the method can be investigated in Strelkova et al. [2007]. The aim from Strelkova et al. [2007] was to formulate a reduced chemical mechanism from the detailed mechanism, for use in CFD simulations of gas turbine combustors. This was done in a two stage procedure.

In the first stage an analysis of the reaction pathways was made in order to exclude both minor reactions and whole pathways. In the second stage a sensitivity tool is used to make a prioritized list over reactions and species in order to remove less important species and reactions. Afterwards a lumping procedure was used to obtain the final reduced mechanism of 38 reactions and 24 species. These procedures are not investigated further, but details of the procedures can be found in Fournet et al. [1999] as given by Strelkova et al. as reference.

The reduced mechanism can be seen in Table 5.1 on page 34. It should be noted that the three reactions marked with "\*" (reactions 4, 14 and 15) is slightly modified from the original mechanism, as it was discovered that these three reactions have mass imbalance between reactants and products. Therefore it will not be applicable in a numerical model, and has to be modified. The original three reactions were:

- 4:  $C_{10}H_{22} + HO_2 \Rightarrow C_2H_5 + *2C_2H_4* + 2OH$  (lack of C- and H-atoms on product side)
- 14:  $C_5H_5 + O_2 \Rightarrow C_5H_4O + *H*$  (lack of O-atom on product side)
- 15:  $C_5H_4O \Rightarrow 2C_2H_2 + *H_2O*$  (lack of C-atom on product side)

Through a study of these reactions in literature available, these have been modified as seen above to obtain mass balance. In the article by Strelkova et al. [2007], it is stated that the CHEMKIN reaction mechanism and thermodynamic data files are available by contacting the authors. An inquiry was made to get these files, but unfortunately no reply was received. As these files were used by Strelkova et al. [2007] mass balance had to be present in these files. It is therefore possible that the errors in the reduced mechanism presented in the article might be due to typing errors. This is what is assumed, and it is decided to proceed the work with the modified reduced mechanism.

As an initial restriction for the reduced mechanism set by Strelkova et al. [2007], it is required that the kinetic curves of the reduced mechanism is within 50 % accuracy of the detailed mechanism in pressure ranges from 1-100 atm, temperatures of 1100-1800 K, and equivalence ratios of 0.5, 1 and 2. In a comparison of results regarding values of ignition times, temperatures and major concentration behaviors, the detailed and reduced mechanisms both show good mutual agreement, and furthermore also good resemblance with experimental results obtained of Jet A kerosene combustion. Curves of these comparisons can be seen in Strelkova et al. [2007].

In reactions 17, 24, 29, and 37 a so called third body,  $M$ , is added to the reactions. This may be any molecule, but is specified closer in the reaction mechanism in Appendix A. In reactions involving two radicals, as with the  $OH + OH$  reaction, a third body is required as it has the ability to absorb the energy released when a stable species is formed. This energy is absorbed as kinetic energy to the third body. Without the third body present, the created species will dissociate to its constituent atoms. [Turns, 2000]

Because this mechanism is used in the CFD simulations in this project, it is important to identify the precursors to soot in the reaction mechanism. The following species are chosen as soot precursors based on the knowledge gain in Section 3.3.1 on page 21:

- **Soot Precursors in the reduced mechanism:**
- $C_6H_6$  (benzene)
- $C_6H_5$  (phenyl-radical)
- $C_2H_2$  (acetylene)
- $C_2H_3$  (vinyl-radical)
- $C_2H_4$  (ethylene)

These soot precursors are the ones that it is wanted to identify in the flow domain of the CFD simulation, in order to determine the location dependent possibility of UFP formation in the combustor model.

**Table 5.1:** The 34 reaction 24 species reduced mechanism for surrogate Jet A [Strelkova et al., 2007].

N	Reactions	A [ <i>cm, molec, s</i> ]	n [–]	E <sub>a</sub> [ <i>kcal/mol</i> ]
1	$C_{10}H_{22} + O_2 \Rightarrow C_2H_5 + 4C_2H_4 + HO_2$	2e-21	3.4	46
2	$C_{10}H_{22} \Rightarrow 2C_2H_5 + 3C_2H_4$	1.26e-17	0	81
3	$C_{10}H_{22} + OH \Rightarrow C_2H_5 + 4C_2H_4 + H_2O$	1.66e-16	2	-0.76
4*	$C_{10}H_{22} + HO_2 \Rightarrow C_2H_5 + 4C_2H_4 + 2OH$	4.07e-11	0	17
5	$C_6H_{14} + O_2 \Rightarrow C_2H_5 + 2C_2H_4 + HO_2$	2e-21	3.4	46
6	$C_6H_{14} \Rightarrow 2C_2H_5 + C_2H_4$	9.55e-16	0	81
7	$C_6H_{14} + OH \Rightarrow C_2H_5 + 2C_2H_4 + H_2O$	4.68e-16	1.61	0.04
8	$C_6H_{14} + HO_2 \Rightarrow C_2H_5 + 2C_2H_4 + 2OH$	2.44e-11	0	17
9	$C_6H_6 + O_2 \Rightarrow C_6H_5 + HO_2$	1.58e-20	3.2	61.5
10	$C_6H_6 + O \Rightarrow C_5H_5 + CO + H$	3.39e-11	0	43
11	$C_6H_6 + OH \Rightarrow C_6H_5 + H_2O$	2.69e-16	1.42	1.45
12	$C_6H_5 + O_2 \Rightarrow C_5H_5 + CO + O$	1.7e-11	0	3.6
13	$C_5H_5 + O \rightleftharpoons C_5H_4O + H$	9.33e-11	-0.02	0.02
14*	$C_5H_5 + O_2 \Rightarrow C_5H_4O + OH$	3.02e-12	0.08	18
15*	$C_5H_4O \Rightarrow 2C_2H_2 + CO$	5.62e-32	-6.76	68.5
16	$C_5H_5 + O \Rightarrow C_2H_2 + C_2H_2 + HCO$	5.37e-11	-0.17	0.44
17	$C_2H_4 + H + M \rightleftharpoons C_2H_5 + M$	1.26e-29	0	0.76
18	$C_2H_4 + H \Rightarrow C_2H_3 + H_2$	3.29e-22	3.62	11.3
19	$C_2H_4 + OH \Rightarrow C_2H_3 + H_2O$	3.39e-11	0	5.96
20	$C_2H_3 + O_2 \Rightarrow HCO + CH_2O$	6.46e-12	0	-0.24
21	$C_2H_3 + H \Rightarrow C_2H_2 + H_2$	3.31e-11	0	2.5
22	$CH_2O + OH \Rightarrow HCO + H_2O$	5.75e-15	1.18	-0.45
23	$HCO + O_2 \Rightarrow HO_2 + CO$	2.24e-11	0	0.4
24	$HCO + M \rightleftharpoons H + CO + M$	3.1e-07	-1	17
25	$C_2H_2 + O \Rightarrow HCCO + H$	1.55e-15	1.4	2.22
26	$HCCO + O \Rightarrow H + CO + CO$	1.58e-10	0	0
27	$CO + OH \rightleftharpoons CO_2 + H$	1.51e-17	1.5	-0.5
28	$H + O_2 \rightleftharpoons O + OH$	3.39e-10	-0.1	15.12
29	$H + O_2 + M \rightleftharpoons HO_2 + M$	7.76e-30	-0.86	0
30	$OH + H_2 \rightleftharpoons H_2O + H$	3.63e-16	1.52	3.48
31	$OH + OH \rightleftharpoons H_2O + O$	5.5e-20	2.42	-1.94
32	$HO_2 + H \Rightarrow OH + OH$	7.41e-10	0	1.4
33	$HO_2 + OH \Rightarrow H_2O + O_2$	4.79e-11	0	-0.497
34	$CH_2O + H \Rightarrow CHO + H_2$	9.55e-17	1.9	2.74
35	$HO_2 + H \Rightarrow H_2 + O_2$	1.75e-10	0	2.06
36	$HO_2 + HO_2 \rightleftharpoons H_2O_2 + O_2$	7e-10	0	12.6
37	$OH + OH + M \rightleftharpoons H_2O_2 + M$	6.31e-30	-0.9	-1.7
38	$H + OH + M \rightleftharpoons H_2O + M$	6.17e-26	-2	0

## 5.4 Kinetic Model - Cantera

At the start of the project it was decided to use the software Cantera to model the kinetics of a few reactions mechanisms, in order, for example, to compare the reduced mechanism to a detailed mechanism. This can be done by comparing the ignition delay of the two mechanisms, as explained in Section 5.2 on page 30. Another result that could be obtained from Cantera is the adiabatic flame temperature of the combustion, which could be used to validate the temperature in the CFD model.

From the reduced mechanism data a Cantera input file to Cantera was made. Unfortunately the file did not work, and no results were obtained from Cantera despite large efforts.

Furthermore a detailed mechanism, describing the oxidation of hydrocarbons with carbon numbers in the interval of 8-16 was applied in Cantera. This mechanism showed to be extensively computational demanding, as a single time-step took in the area of 40 minutes to perform, where it normally will take approximately a few seconds. The same picture unfolded for other mechanisms regarding biodiesel. Hence this was taken to be too computational demanding.

No further work with Cantera was made in this project.

**In order to CFD model the formation of UFPs from the combustion of Jet A, a domain is needed in which the simulation can be done. The domain is based on the geometry of the SR-30 Turbojet Engine, which is described in the following chapter. The focus is on the reactions and particle formation happening inside the modeled combustion chamber. This is based on the delimitation mentioned in the Project Description, that states that the reactions happening in the exhaust gas is beyond the scope of this project, and will not be covered further.**



---

# SR-30 Turbojet Engine

---

# 6

The combustion chamber of the gas turbine is used to CFD model the combustion of the Jet A surrogate fuel, and thus this chapter describes the gas turbine. The chapter contains four sections that describe the key parts of the turbine in relation to this project. The last section in this chapter contains results from experiments done on the gas turbine, conducted by Jensen et al. [2012].

## 6.1 The SR-30 Turbojet Engine

The SR-30 Turbojet Engine (SR-30) is a small gas turbine that is used for education, study, and research which is designed and produced by Turbine Technologies. The turbine corresponds to typical full scale gas turbines and thus allows studies of full scale turbine operation. Different kinds of fuel can be used in the SR-30, but the fuel used in this project is kerosene. The SR-30 Turbojet Engine can be seen in Fig. 6.1 placed inside a protective cabinet. The turbine is the middle part seen in the figure. Fitted onto the air intake of the turbine is a white, almost oval shaped box, which is a silencer. At the turbine outlet an exhaust pipe is mounted. There is a gap between the turbine outlet and the exhaust pipe to ensure the exhaust gas meets ambient pressure.



*Figure 6.1: The SR-30 Turbojet Engine modelled in this project [Technologies, 2007].*

## 6.2 Operation Conditions and Dimensions

The turbine operation cycle on the SR-30 is similar to any other gas turbine. The steps in the cycle corresponds to the numbers seen in Figure 6.2:

1. Ambient air for combustion is supplied through the cone shaped air inlet.
2. The ambient air is compressed and guided through the holes of an outer liner into the combustion chamber.
3. Liquid fuel is injected into the combustion chamber and a non-premixed combustion occurs between the fuel and compressed ambient air.
4. The hot combustion gas is accelerated through a guided vane, making the turbine rotate, which powers the compressor.
5. Jet thrust is produced by accelerating the gas through the thrust nozzle, which converts the heat energy that's left in the gas to jet thrust. The gas finally enters the exhaust pipe and is mixed with ambient air.

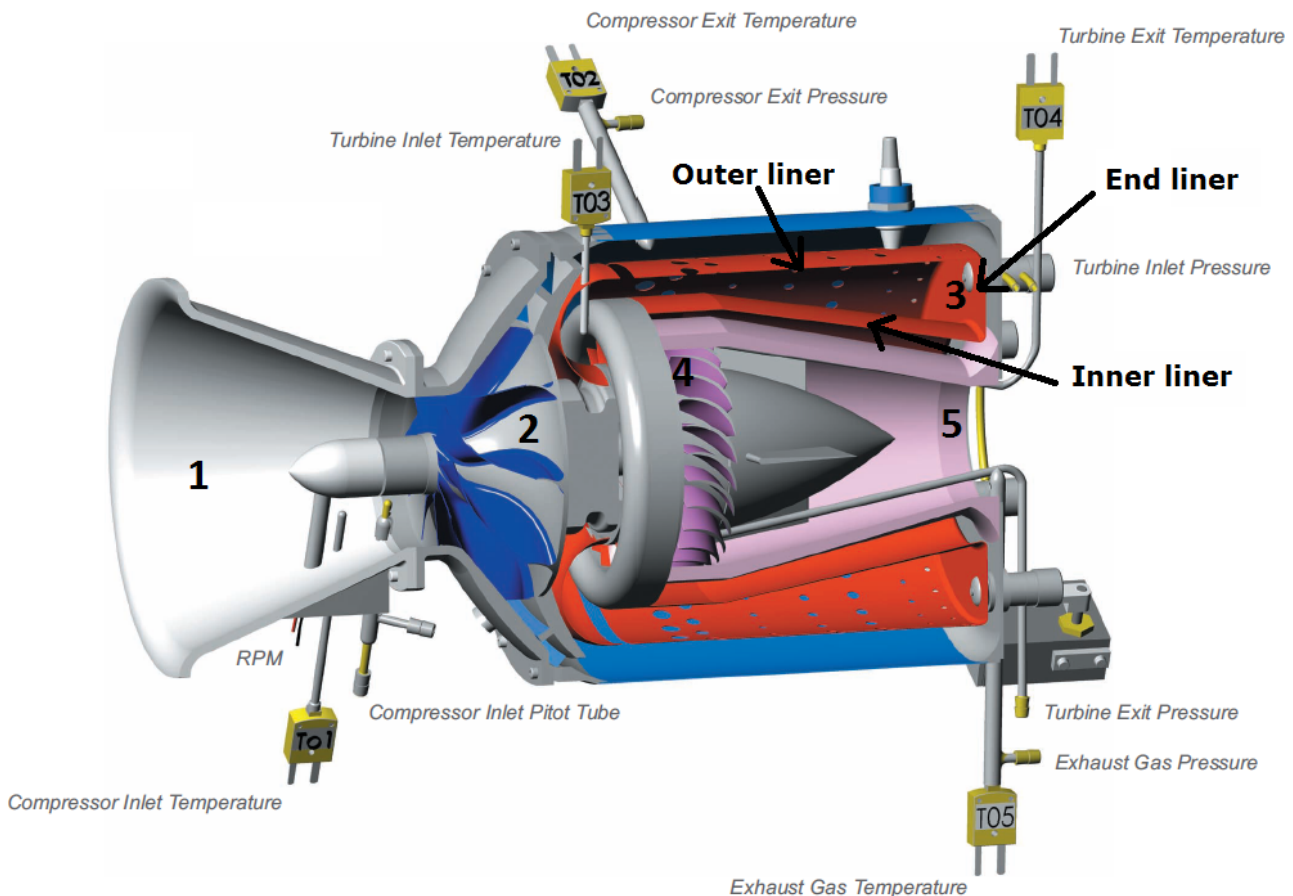


**Figure 6.2:** The inside of the SR-30 Turbojet Engine, including placement of sensors [Technologies, 2007].

Due to the structure of the combustor it is characterized as a reverse-flow annular combustor. This will be explained in section 6.4 on page 40.

The rated conditions for the turbine as given by Turbine Technologies can be seen in Table 6.1.

**Table 6.1:** The rated operation conditions for the SR-30 Turbojet Engine specified by the manufacturer.[Technologies, 2007]

Engine Compression Ratio	3.4
Exhaust Gas Temperature	720 ° C
Engine Diameter	17 cm
Engine Length	27 cm
Mass Flow	0.5 kg/s
Design Maximum Thrust	178 N
Compressor Type	Single Stage Centrifugal
Turbine Type	Single Stage Axial Flow
Design Maximum RPM	87,000

### 6.3 The Combustion Chamber

An example of a reverse-flow annular combustion chamber can be seen on Figure 6.3. The figure does not represent the actual combustion chamber on the SR-30, but shows the general concept of this particular combustion chamber.

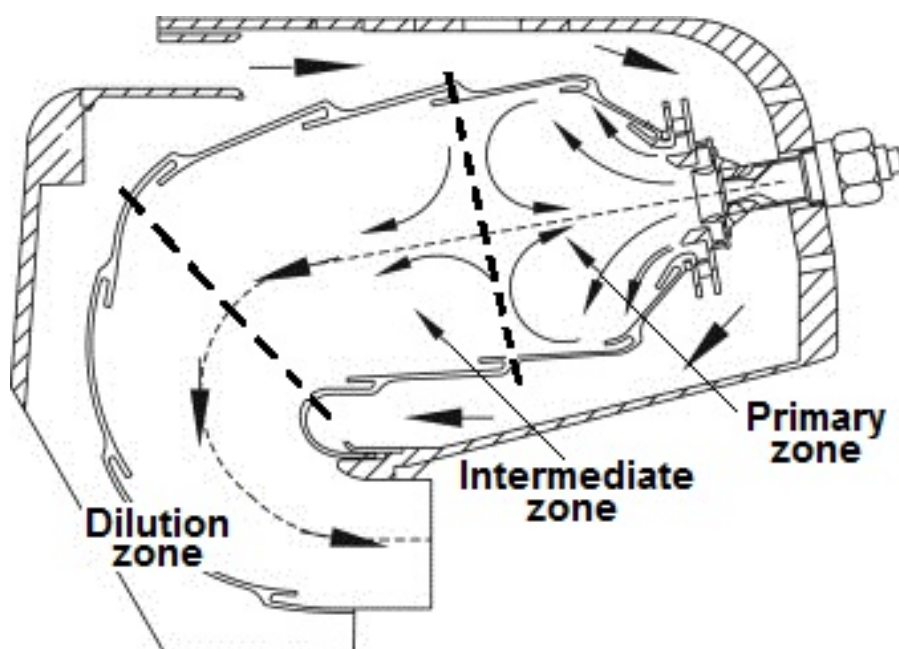


**Figure 6.3:** An example of a reverse-flow annular combustion chamber which also is used on the SR-30 [Turns, 2000].

As seen on Figure 6.3 the combustion chamber is essentially divided into three zones as described by [Lefebvre and Ballal, 2010].

- Primary zone: Anchors the flame and provides the conditions, *i.e.* temperature, turbulence and time, to

(theoretically) achieve complete combustion.

- Intermediate zone: Air from the liners cool the gas and allows unburned hydrocarbons to complete combustion, along with allowing burnout of soot.
- Dilution zone: The purpose of the dilution zone is too cool the gas to a temperature acceptable to the turbine blades.

As the ambient air is introduced to the combustion zones through the outer (upper), inner(lower) and end liner separately from the liquid fuel, the combustion is characterized as non-premixed. The fuels is not completely vaporized when entering the combustion zone, and the combustion is therefore called heterogeneous spray combustion, since the air and fuels is in different physical state.

## 6.4 Air Delivery System

As explained in the start of this chapter the combustion chamber of the SR-30 is known as a reverse-flow annular combustor. This is because ambient air enters the combustion chamber from the outer and inner liner in which the air flows are reverse. Due to a longer flow length of the ambient air going through the inner liner there is a higher pressure loss in this part of the combustion chamber, compared to the air flowing through the outer liner. This makes it very difficult to balance the air flow from the two liners, and in return a recirculation flow zone from a created single-vortex appears, which helps to film-cool the liner and afterwards helping the primary combustion.

Another challenge with the reverse-flow annular combustion chamber is that it has a large surface area that needs cooling, compared to the combustor volume. Thus a high flow of cooling air is needed to ensure that the combustor material does not fail. [Wei-hua et al., 2011]

## 6.5 Liquid Fuel Injection

The liquid fuel is supplied to the combustion chamber through six fuel injector nozzles placed at the opposite end of the combustion chamber compared to the air inlet. There is a 60 degree spacing between each fuel inlet relative to the center of the circular shape of the combustor. The injectors operate under high pressure which causes the liquid fuel sheet to break up into droplets of different size, also known as atomization. It is unknown what type of specific atomizer is used on the SR-30. This means that the droplet distribution size is also unknown. More on this will be discussed in Chapter 7 on page 45.

## 6.6 SR-30 Experiments

This section describes the results of the experiment done on the SR-30 conducted by Jensen et al. [2012], who shared their results with the authors of this report. The experiment on the SR-30 was done in order to determine its operation conditions, and this data has been used in this report. Note that the turbine was using kerosene as fuel during this experiment. In the experiment the temperatures, pressures and mass flows in different locations in the turbine was measured using sensor located on the SR-30 setup, as seen on Figure 6.2 on page 38. The procedure of the experiment was to maintain the turbine at given speed for 2 minutes in order to get stabilized measurements. After the turbine was running stable at the given speed the measurements were taken. Each measurement was repeated for a series of rotational speeds. Appendix B contains a small part of the measurements that the values used in this report is based on.

In Figure 6.4 the gauge pressures at the different pressure sensor locations in the turbine can be seen. The pressure of the ambient air increases as the rotational speed increases. The energy in the compressed air is extracted in the turbine which reduces its pressure. Along the curves a number of points seem to gather, for example at  $7.25 \cdot 10^4$  RPM. This is where the turbine has stabilized.

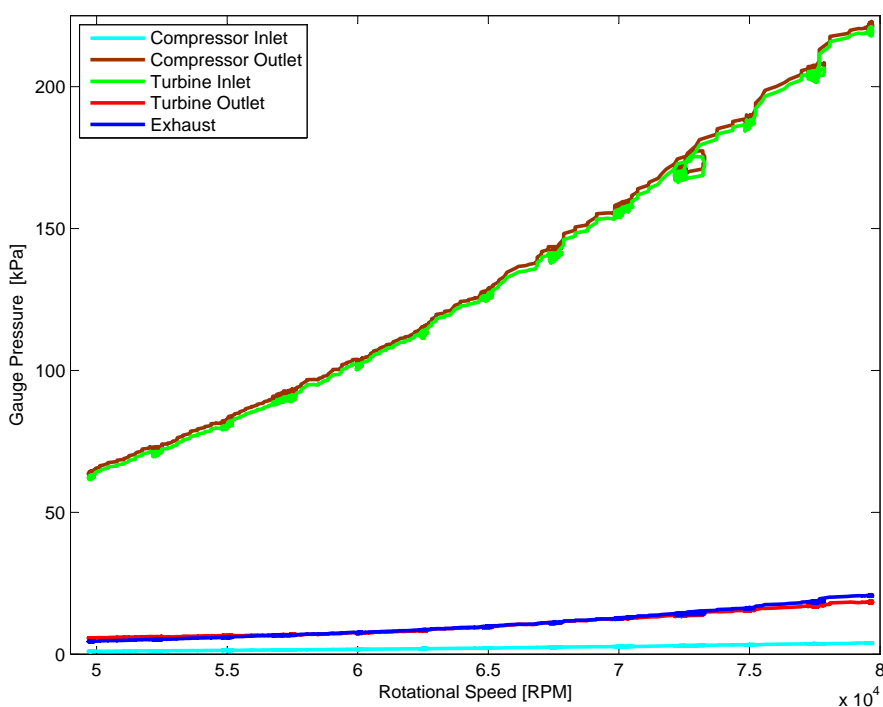


**Figure 6.4:** Operating Pressures at different locations on the SR-30 [Jensen et al., 2012].

On Figure 6.5 on the next page the temperature in the turbine can be seen. Similar for all four curves it can be said that the higher rotational speed, the higher temperature. At the lowest rotational speed the ambient air temperature is increased to  $100\text{ }^{\circ}\text{C}$  by the compressor. For the same rotational speed a large increase in temperature happens as the air reach the combustion zone. Afterwards the hot gas enters the turbine with a temperature of approximately  $520\text{ }^{\circ}\text{C}$ . As the hot gas leaves the turbine it is cooled by ambient air and its temperature decreases to roughly  $250\text{ }^{\circ}\text{C}$ .

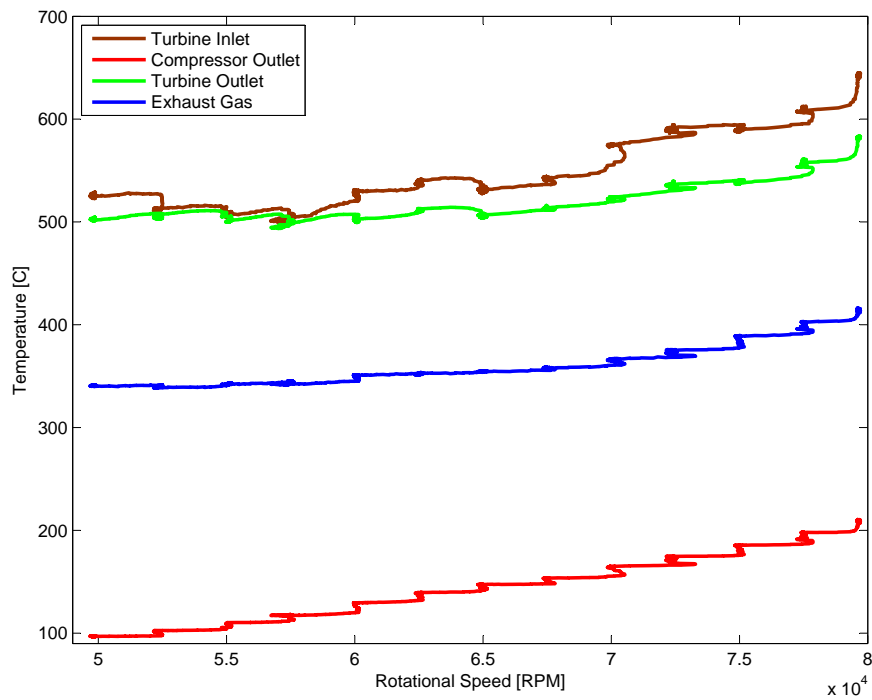


**Figure 6.5:** Operating temperatures at different locations in the SR-30 [Jensen et al., 2012].

The equivalence ratio as function of rotational speed of the SR-30 is seen in figure 6.6.

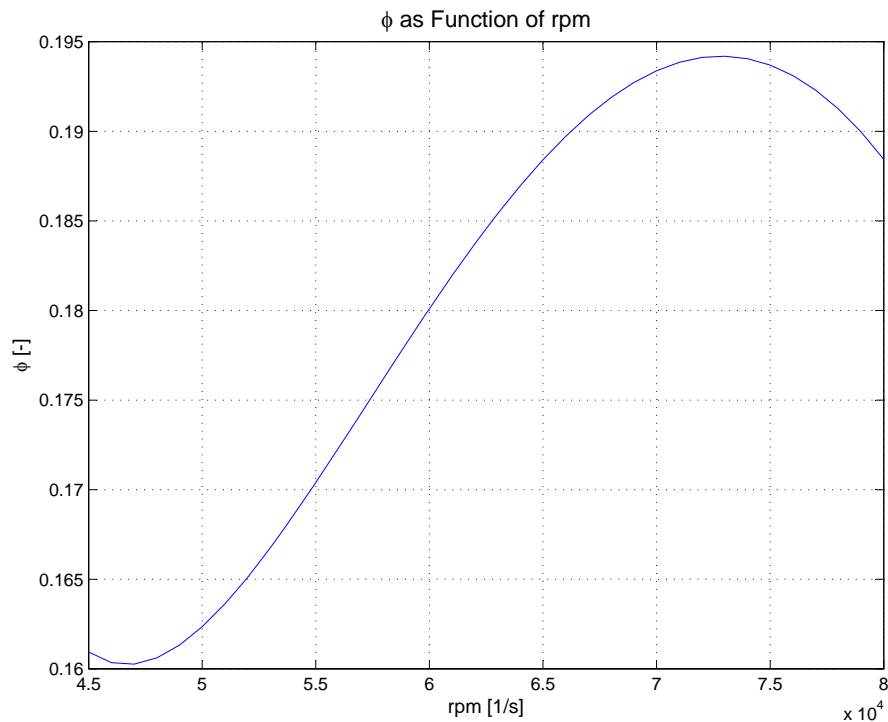


**Figure 6.6:** Equivalence ratio at different rotational speeds of the SR-30 [Jensen et al., 2012].

## 6.7 Inlet and Outlet Conditions of the Combustor Zone

Based on the measurements done on the SR-30, inlet and outlet conditions for the combustion zone is obtained. The pressures, temperatures, and the mass flow of fuel are directly taken from the measurements done, and the mass flow of air from the equivalence ratio obtained from Figure 6.6 on the preceding page. All values are obtained at the turbines maximum capability at approximately 80,000 RPM, as this is the case which will be modeled in the CFD simulation.

The mass flow of fuel has been measured in the units of  $l/hr$ , as this is the setup of the measurement software supplied by [Technologies, 2012]. Converting to SI units of  $m^3/s$  yields

$$\dot{V}_{fuel} = 19.6 \frac{l}{hr} = 5.444 \cdot 10^{-6} \left[ \frac{m^3}{s} \right] \quad (6.1)$$

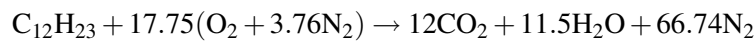
The density of kerosene, which is the fuel used in the experiments, is  $\rho_{kerosene} = 820 \text{ kg/m}^3$  [Chemical Education Group, 2012]. The mass flow of fuel is then calculated to

$$\dot{m}_{fuel} = 5.444 \cdot 10^{-6} \frac{m^3}{s} \cdot 820 \frac{kg}{m^3} = 4.464 \cdot 10^{-3} \left[ \frac{kg}{s} \right] \quad (6.2)$$

Mass flow of air at the inlet is then found by equation 6.3

$$\dot{m}_{air} = \dot{m}_{fuel} \cdot (A/F) = \dot{m}_{fuel} \cdot \frac{(A/F)_{stoich}}{\phi} \left[ \frac{kg}{s} \right] \quad (6.3)$$

Where  $A/F$  is the air-fuel ratio [-],  $A/F_{stoich}$  is the stoichiometric air-fuel ratio [-], and  $\phi$  is the equivalence ratio [-]. From Figure 6.6 on the preceding page, the equivalence ratio is obtained at a rotational speed of 80,000 RPM, and this yields a value of approximately  $\phi = 0.188$ . The stoichiometric air-fuel ratio is calculated from the molar masses of the kerosene,  $M_{fuel}$  and air,  $M_{air}$  and the stoichiometric coefficient of the combustion of kerosene and air,  $\nu_{stoich}$ . As kerosene is a mixture of different hydrocarbons, a single correct chemical formula is not obtainable. However, as Jet A is a kerosene based fuel, it is assumed that the chemical formula resembles Jet A, which is presented in a simplified manor by Su and Zhou [1999] as  $C_{12}H_{23}$ . An overall stoichiometric reaction for this can then be written as



Here it is seen that  $\nu_{stoich} = 17.75$ . Hence, the stoichiometric air-fuel ratio can be calculated as seen in equation 6.4.

$$(A/F_{stoich}) = \frac{\nu_{stoich} \cdot 4.76 \cdot M_{air}}{M_{fuel}} = \frac{17.75 \cdot 4.76 \cdot 28.85 \frac{mol}{kg}}{12 \cdot 12.01 \frac{mol}{kg} + 23 \cdot 1.01 \frac{mol}{kg}} = 14.57 \quad [-] \quad (6.4)$$

Thereby the mass flow of air can be found as equation 6.5.

$$\dot{m}_{air} = 4.464 \cdot 10^{-3} \frac{kg}{s} \cdot \frac{14.57}{0.188} = 0.346 \left[ \frac{kg}{s} \right] \quad (6.5)$$

All of the measurements and calculated values used for boundary conditions in the CFD simulations are seen in Table 6.2

**Table 6.2:** Measurements and calculated values used for the CFD simulation.

<b>Boundary condition</b>	<b>Value</b>	<b>Unit</b>
Gauge pressure after the compressor	221,000	Pa
Gauge pressure before the turbine	219,000	Pa
Mass flow of air	0.346	kg/s
Mass flow of fuel	$4.464 \cdot 10^{-3}$	kg/s
Air temperature after the compressor	483	K
Turbine inlet temperature	915	K

**In this chapter, information of the modeled SR-30 Turbojet Engine is given. This includes its operation cycle, combustion chamber, air delivery system and its liquid fuel injection system. Furthermore, the experimental results conducted by Jensen et al. [2012] on the SR-30 is presented, which are used as input for boundary conditions and validation of the CFD model presented in the next chapter.**

CFD is a strong tool for modeling soot/UFP formation due to the fact that local conditions throughout the combustion chamber of the SR-30 can be investigated. As described in section 3.3 on page 20 soot is formed in fuel rich regions. Using ANSYS Fluent enables the detection of these fuel rich regions, which as stated in the Project Description in Chapter 4 might show the presence of precursors of soot, from which soot and UFPs assumely are formed.

## 7.1 Geometry and Mesh

This section contains a description of how the geometry of the combustion chamber on the SR-30 is made, and shows the mesh constructed on the geometry. A mesh independency check is also made in order to investigate the quality of the mesh, which is found in Appendix D.

### 7.1.1 Creating the 3D geometry of the combustor

In this section the development of the 3D geometry used in the ANSYS Fluent simulation of the SR-30 combustion chamber is outlined. It was chosen to model the combustor in 3D in order to capture the flow field, and identify the paths of the particles injected into the combustion chamber.

As a CFD simulation of the entire combustion chamber would require alot of computation power and time, it is decided only to simulate 1/6 of the geometry. This is chosen as the SR-30, as described, have 6 fuel inlets, which therefore make this choice preferable considering the use of symmetry boundary conditions in the CFD simulation. To be able to create the CAD drawing suitable for CFD simulations of the combustor zone, which includes the zone from the compressor outlet to the turbine inlet, simplifications and alternations of the design had to be made. Initially in the project work, no dimensions or detailed structure of the SR-30 was available for the authors. However, after consulting Technologies [2012], a Solidworks CAD drawing of the internal parts of the combustor was created by them and is available for this project. The assembly CAD file of the differet parts are shown in figure 7.1 on the following page. The unfolded cone hanging beside the line of parts is the unfolded inner liner of the combustion chamber. This was recieved as is shown and had to be remade.

As seen this model contains all of the parts of the SR-30, including air inlet cone, compressor, turbine, exhaust, etc. Hence, based on the scope of this project on the combustion zone, only the parts and dimensions important for the combustion zone were considered for the CFD geometry. The outer surfaces of the final combustor geometry created is seen in figure 7.2 on the next page, with the outer dimensions attached.

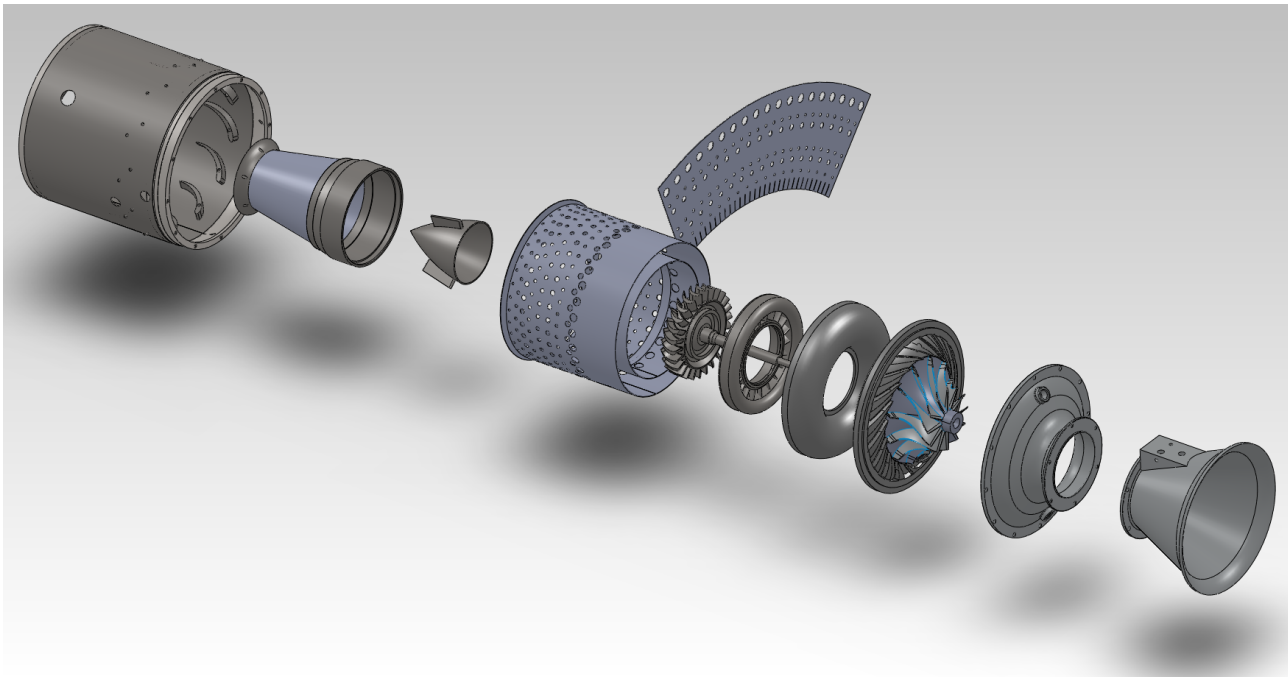


*Figure 7.1:* CAD assembly file received by Technologies [2012].

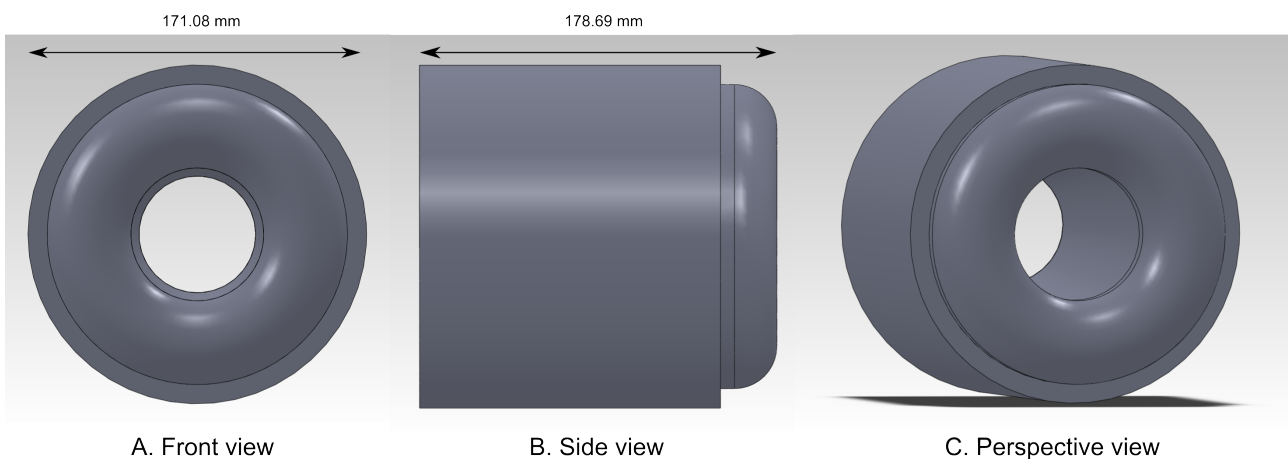


*Figure 7.2:* Outer surfaces and dimensions of the combustor geometry.

It is chosen not to reuse these Solidworks drawings due to complexities, and hence new ones are made from the dimensions and shapes given. This is mainly because the liner holes has to be moved to gain symmetry of the 1/6 part, and this cause problems with the existing CAD model parts. The new liners created are shown in figure 7.3 on the facing page

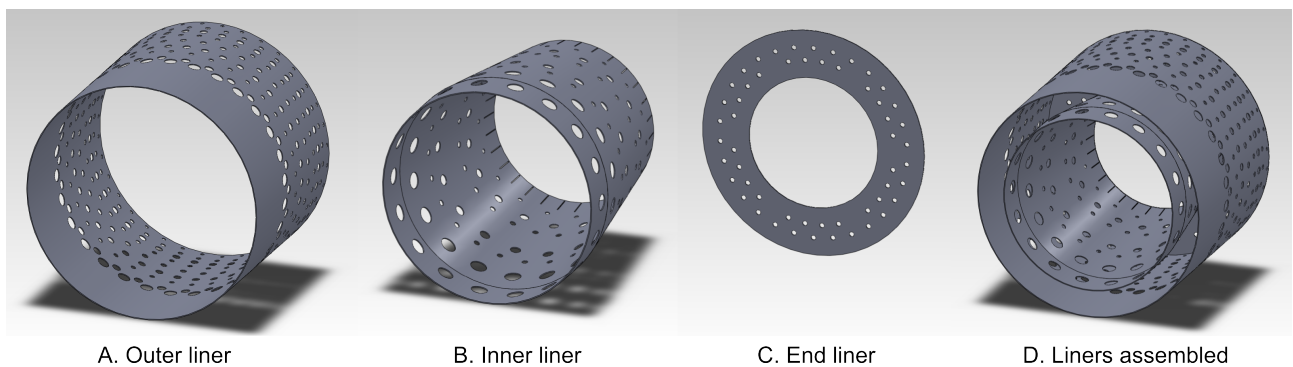
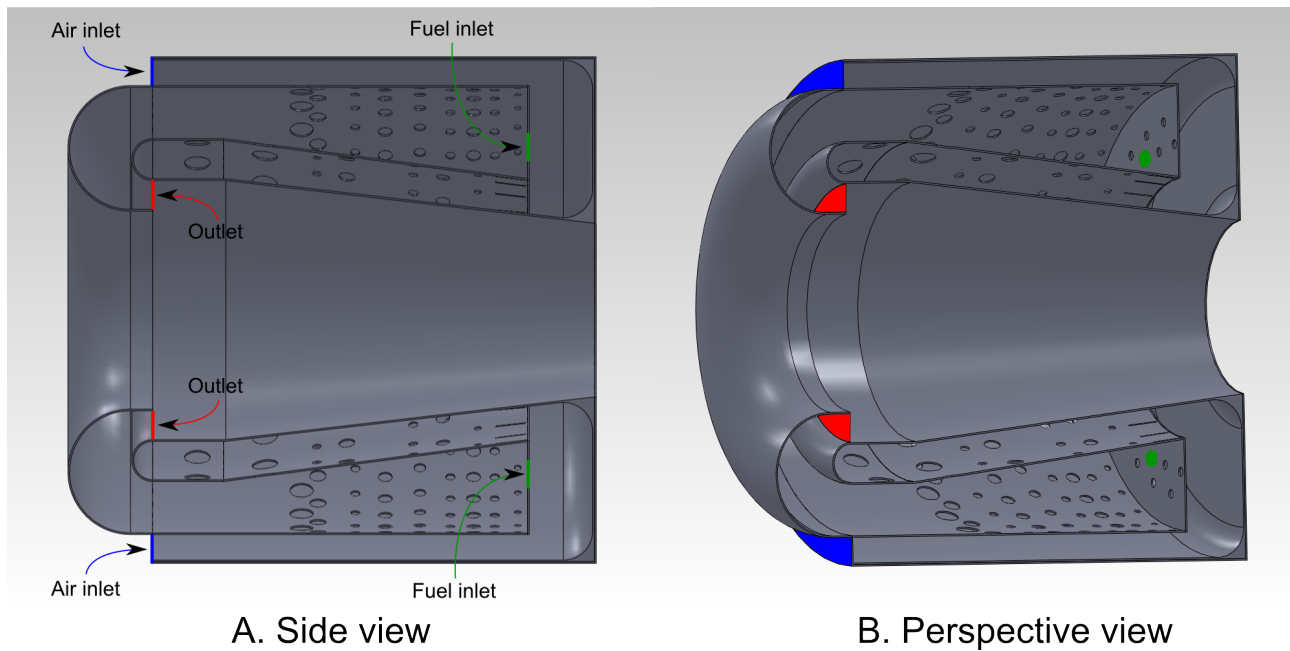


**Figure 7.3:** The liners used for the geometry.

As mentioned a few alterations of the combustor design according to the Solidworks drawings received from Technologies [2012] is made. Modifications done on the CAD model include:

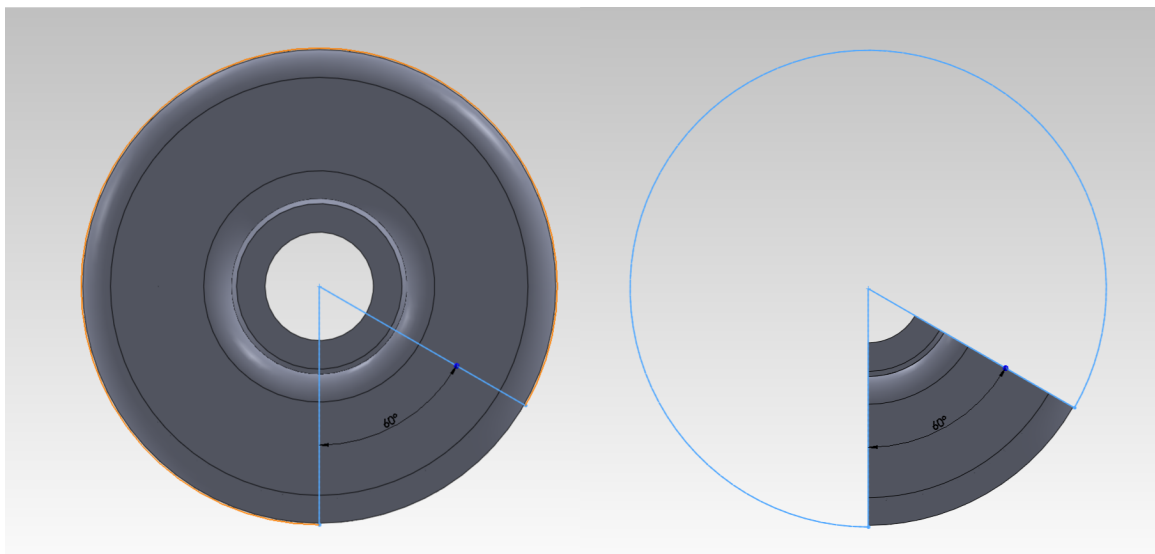
- Removal of compressor air guiding vanes on the outer shell of the combustor  
*The guiding vanes are removed as the purpose of these are to guide the air from the compressor which is not considered in this simulation, and hence are neglected.*
- Restructuring of the liner holes  
*This is done to gain symmetry of the holes in the 1/6 part. It however means that the total area of holes in the liners are not 100% correct, as moving holes to gain symmetry forced the removal or adding of holes of each type. This will have some effect on the results, but was necessary to proceed to the meshing. A way to compensate for this could be to resize the holes according to whether holes have been removed or added, but this is not done in this model.*
- Small changes in the overall dimensions.  
*Minor changes of the length and diameter of the inner liner and the end liner respectively are done, as the dimensions given in the received CAD model did not exactly fit together. The end liner diameter is decreased on the outer diameter of the part as it is here the deviation is present. To compensate for this, the end liner holes and fuel inlet are moved accordingly to keep them centered on the end liner annulus. Moreover the outer shell diameter was unavoidably reduced by 2 mm.*

Figure 7.4 on the next page illustrates the combustor cut in half, to show the inner structure of the combustor.



**Figure 7.4:** Side view of the combustor geometry. Blue marks the inlet, red marks the outlet, and green marks the approximate placement of the fuel inlets.

Marked with blue is the air inlet, while the red is marking the outlet of the combustion products. The green mark is illustrating the approximate placement of the fuel inlets. It should again be emphasized that only 6 circular fuel inlets are present in the combustor, with uniform spacing of 60 degrees on a circular surface on the end liner.



**Figure 7.5:** The 60 degree fluid domain part is cut out.

In order to be able to mesh the fluid domain and use it in the CFD simulations, the fluid domain of the combustor will have to be the solid part, and the steel walls have to be gaps in the geometry. This is obtained by using the mold cavity function in Solidworks. This function lets the user hollow out a solid block, according to the shape

of an already existing geometry. Hence, by creating a solid block which exactly fits on the combustor geometry made, and using this function, the wanted solid fluid domain is attained. The last step is then to remove 5/6 of the geometry, so the 60 degree fluid domain part of the circular combustor is left. This is illustrated on figure 7.5 on the facing page.

The 60 degree cutout fluid domain part which is to be used for meshing and CFD simulation is then better shown in figure 7.6.

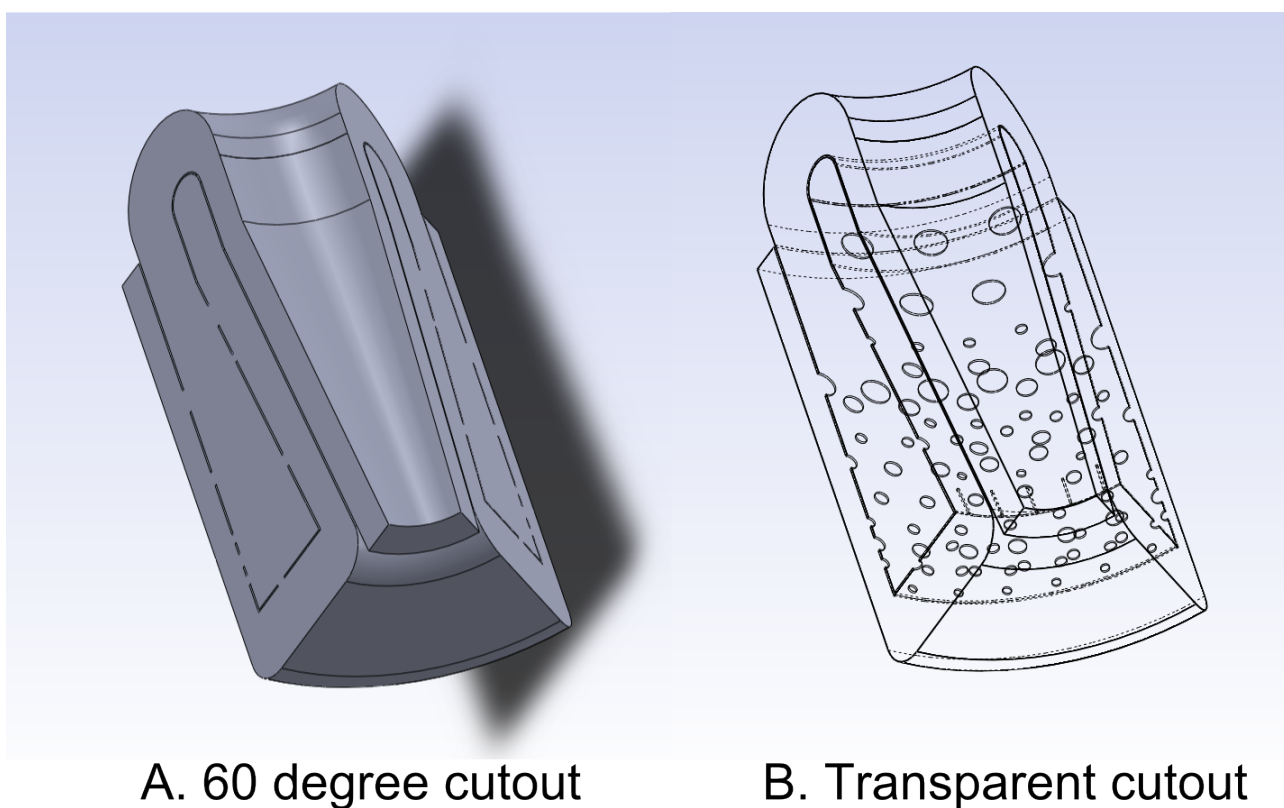


*Figure 7.6:* The 60 degree fluid domain viewed both in solid and transparent.

Figure 7.6 B shows the cutout in a transparent style, where the hollow parts inside the solid is seen. Figure 7.7 on the next page presents the cutout in a side view, to show the extra solid pipe length added to the fluid domain, after the real outlet (the turbine inlet on the SR-30) marked with red. This is attached, as an outlet boundary condition placed directly at the real outlet in a CFD simulation, would cause this to affect the flow and reactions further up in the combustor. The extra pipe length before the outlet assures that this is not the case.

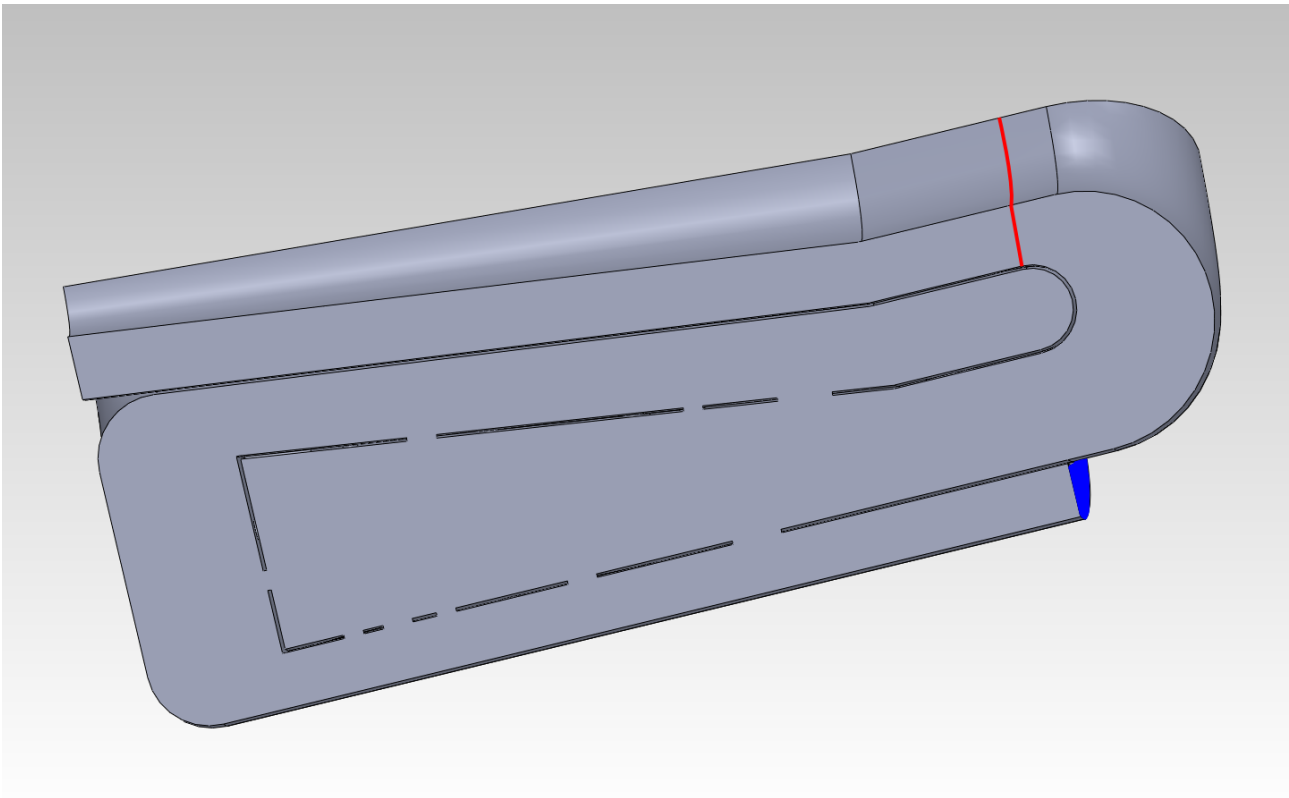


**Figure 7.7:** Side view of the 60 degree cutout. Blue marks the inlet, and red marks the real

This cutout geometry is then exported to ANSYS ICEM as an .IGS file, where the meshing is carried out.

### 7.1.2 Creating the mesh

This section shows the considerations done and the development of the mesh, to be used in ANSYS Fluent. ANSYS Icem is used for creating the mesh of the geometry, representing the fluid domain of the 1/6 cut of combustor. As the geometry is very complex, especially considering the circular and oblong rectangular liner holes which are not placed in any overall structured manner, an entirely unstructured mesh of tetrahedral cells is created. Making a pure structured mesh of this geometry is too extensive, and is not considered in this project. The use of a fully unstructured tetrahedral mesh does however have a negative impact on the solution of the flowfield, especially the boundary layers, but also on the overall flow field. For example regarding numerical diffusion, as it is not possible to make the mesh follow the streamlines of the flow.

Initially, the imported geometry is split in a few hundred different parts, mainly because each liner hole is separated in to half circles, which results in a big amount of different parts. Therefore the surfaces of the geometry is collected in fewer parts, which still makes it possible to specify specific boundary conditions where it is needed, *e.g.* the inlets, outlets, and on the different wall surface areas. The curves representing the geometry in ICEM, and the subdivision of the different geometry parts is illustrated in figure 7.8 on the facing page.

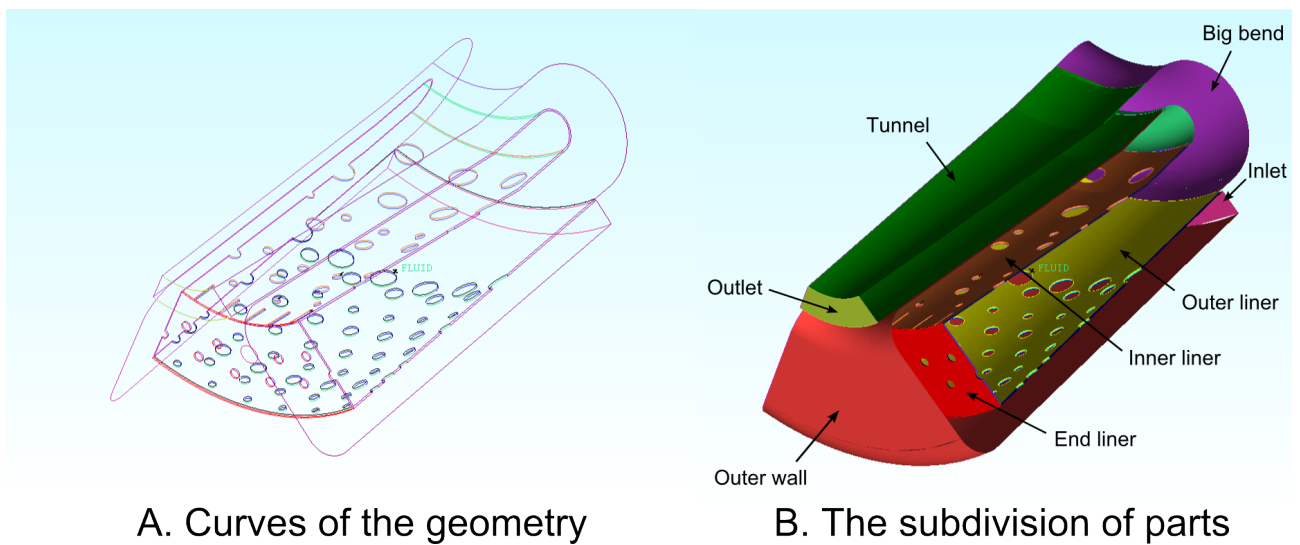


**Figure 7.8:** Figure A shows the curves defining the geometry in ICEM. Figure B shows the subdivision of parts of the geometry.

It should be noted that the each liner part showed in Figure 7.8 B is divided further into an inner and outer surface, and a part which includes the hole surface ares, due to the height of the liner holes. This is done so that boundary conditions for each of these surfaces can be specified.

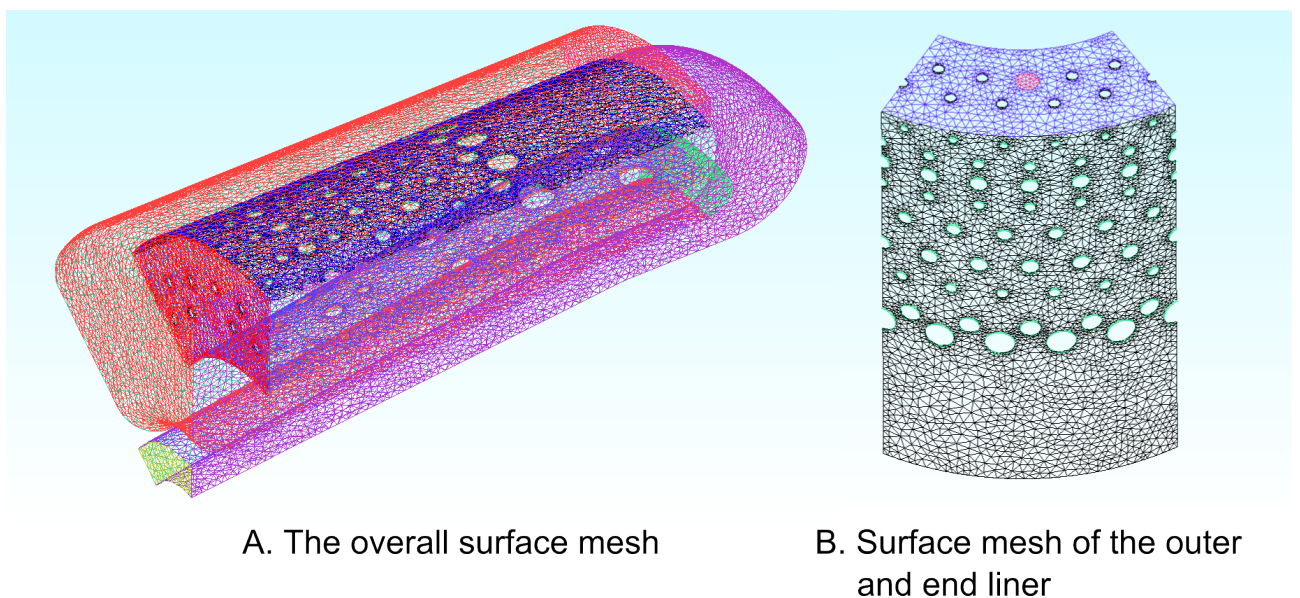


**Figure 7.9:** A. shows the overall surface mesh created, and B. shows the surface mesh of the outer and end liner.

Due to the relatively short period available for the project, it is decided to make a rather coarse mesh of the geometry, and thereby save the time of creating a structured mesh, as well as computational expenses and time by computing on a very fine mesh. It might not resemble the most accurate solution of the CFD modeling, but it is favored to be able to make reasonably fast computations.

The mesh is as mentioned earlier created in ANSYS ICEM, using the Robust(Octree) mesh method. Here the

node numbers around the circular and rectangular liner holes are specified, to get the mesh around them satisfactory refined. The mesh is then smoothed according to aspect ratio, min. angle, and equiangle skewness. Furthermore it is important that the expansion rate of the mesh is not too large. [WS Atkins and members of the NSC, 2002]. The mesh created consisting of 600,000 elements, is seen in Figure 7.9 on the preceding page, figure A and B. Note that it has been prioritized to create a relatively fine surface mesh around the liner holes, in order to avoid bad resolution of the holes and to take more care of the large velocity gradients through the holes.

The quality metrics reported by ANSYS Icem are as seen in figures 7.1

*Table 7.1:* Quality metrics from ANSYS Icem.

Quality metric	Aspect Ratio	Equiangle skewness
0.95-1	0.770 %	0.253 %
0.90-0.95	3.119 %	0.817 %
0.85-0.90	5.946 %	1.818 %
0.80-0.85	8.774 %	3.802 %
0.75-0.8	11.523 %	7.393 %
0.7-0.75	13.900 %	13.187 %
0.65-0.7	15.373 %	20.422 %
0.6-0.65	16.455 %	22.424 %
0.55-0.6	17.969 %	17.392 %
0.5-0.55	5.575 %	9.000 %
0.45-0.5	0.494 %	2.869 %
0.4-0.45	0.086 %	0.541 %
0.35-0.4	0.014 %	0.061 %
0.3-0.35	0.003 %	0.020 %
0.25-0.3	-	0.003 %
0.2-0.25	-	-
0.15-0.2	-	-
0.1-0.15	-	-
0.05-0.1	-	-
0-0.05	-	-

These are shown by a scale of 0 to 1, where 1 is a high quality mesh and 0 is poor quality. It is seen that the major part of the cells are above 0.5 which is chosen to be acceptable for the simulation. In Figure 7.10 on the facing page the lowest quality cells, < 0.4, are marked in the mesh volume. As seen these are mostly concentrated on the bottom edge of the end liner, marked with a red circle. As this is outside the combustion zone, and the majority of the cells are not in the liner hole vicinity, this is accepted and it is assumed it will not have a significant impact on the simulation results.

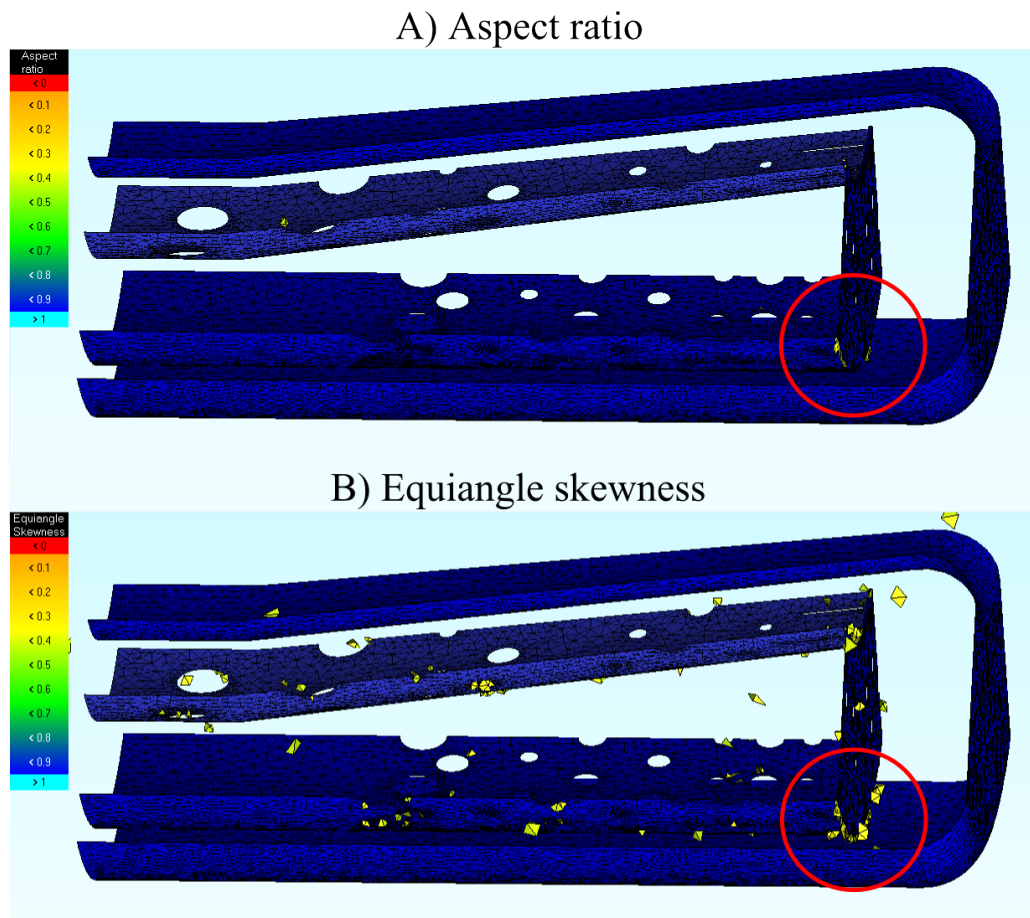


**Figure 7.10:** A. shows the aspect ratio, and B. shows the equiangle skewness.

In order to determine an appropriate cell size in the tetrahedral mesh the Taylor microscale is used. This is given by equation 7.1, and is defined as the largest length scale where dynamics of turbulent eddies are significantly affecting the viscosity of the fluid in the flow.

$$\lambda = \sqrt{10 \cdot \nu_{air} \cdot \frac{k}{\epsilon}} \quad (7.1)$$

where  $\nu$  is the kinematic viscosity of the fluid [ $m^2/s$ ],  $k$  is the turbulent kinetic energy [ $m^2/s^2$ ], and  $\epsilon$  is the dissipation rate of kinetic energy [ $m^2/s^3$ ]. The size of the mesh should be 1 to 2 times the size of the Taylor microscale.[Yin, 2012]. Therefore to determine the size of the Taylor microscale,  $\nu_{air}$ ,  $k$  and  $\epsilon$  need to be found.

The density of air,  $\rho_{air}$ , and the dynamic viscosity of air,  $\mu_{air}$ , are found at  $T = 1000K$  and  $P_{total} = 320,000 Pa$  by the use of the software Engineering Equation Solver(EES). These values of temperature and pressure resemble the setup made in the non-reacting CFD simulation, which are presented hereunder in section 7.2.1 on the following page. This yields values of  $\rho_{air}=1.113kg/m^3$  and  $\mu_{air}=4.329 \cdot 10^{-5}kg/m \cdot s$ . Hereby, the kinematic viscosity found as equation 7.2.

$$\nu_{air} = \frac{\rho_{air}}{\mu_{air}} = \frac{4.329 \cdot 10^{-5}kg/m \cdot s}{1.113kg/m^3} = 3.889 \cdot 10^{-5}m^2/s \quad (7.2)$$

$k$  and  $\epsilon$  are found on the basis of this non-reacting CFD simulation, done on the 600,000 cell mesh. Volume-weighted average values of  $k$  and  $\epsilon$  in the entire fluid domain is then be reported, and this yields values of  $k = 126.3m^2/s^2$  and  $\epsilon = 338,526m^2/s^3$ . The Taylor microscale is then calculated to

$$\lambda = \sqrt{10 \cdot 3.889 \cdot 10^{-5}m^2/s \cdot \frac{126.3m^2/s^2}{338,526m^2/s^3}} = 0.381 \cdot 10^{-4}m \quad (7.3)$$

Hence, ideally, the cell size should be in the range of 0.318-0.762 mm. This cell size would however mean that the overall amount would be too extensive, summing to a few million cells. It is therefore decided, in collaboration with the supervisors of this project, that a relatively coarse mesh for this project should be used, considering the computational requirements and the time at hand. From a mesh independency study based on the velocity in a point from the non-reacting ANSYS Fluent simulation described in the next section, a 200,000, 400,000 and 600,000 element mesh is compared in Appendix D. This shows a quite similar point velocity for all three meshes, but it is decided to proceed with the 600,000 mesh as it will have a better resolution of the flow field. This will still compromise the quality of the solution, as the gradients in combustion zone and the liner holes are not refined adequately even with the 600,000 element mesh.

The mesh is then imported to ANSYS Fluent, to proceed with the CFD simulation setup.

## 7.2 CFD Model

In this section, the different simulations done in ANSYS Fluent on the mesh case created are accounted for. Fluent setups are shown and discussed. The case simulated, is the turbine running on its maximum capability at around 80,000 RPM, which resembles a take-off scenario of an airplane.

### 7.2.1 Non-Reacting Simulation

Initially a simulation is done with the species model disabled, and therefore with pure air flowing through the combustor at a temperature of 1000 K. This is done to have a solution which can be used as initialization for the combustion simulation, which will give an initial flow field and high constant temperature in the combustor. The overall setup in Fluent for this simulation is as seen in Table 7.2

**Table 7.2:** Fluent setup for the non-reacting simulation.

Setup parameter	Setting
Solver type	Pressure based
Models enabled	Energy Radiation Viscous
Turbulence model	$k - \epsilon$ realizable
Wall treatment	Standard wall function
Radiation model	P-1
Discretization	Third-order MUSCL
Underrelaxation factors	Default

$k - \epsilon$  turbulence model is chosen, as this is a widely used model because of its good performance in a variety of engineering flows, and it is relative simple compared to more complex turbulence models [Henneke et al., 2001]. *Realizable* refers to that it meets specific mathematical constraints on the Reynolds stresses, accordant with physics of turbulent flows[ANSYS, 2009c]. The model performs well in confined flows where the importance of Reynolds shear stresses are significant, as in this case. It however does lack in performance in flows with diverging passages and curved boundary layers that cause large quick extra strains in the flow, which also is present in this simulation[Versteeg and Malalasekera, 2008]. The spreading rates of round jets, as in the liner holes, also have a tendency to be predicted incorrectly, and effects of expansion on the production of turbulence, which might be important for compressible flows, is not taken into account [Group, 2000]. It is however decided to be the most robust solution for the simulation on the coarse unstructured mesh.

As the mesh is rather course, also at the wall in the boundary layer zones, the standard wall function is used where the dimensionless wall distance  $y^+$  should be in the range of 30-300 in the log-layer [Yin, 2010], and should certainly not be under 11 [WS Atkins and members of the NSC, 2002]. This is obeyed in the majority of the nodes in boundary layers in the simulations, but not everywhere. However, as it is known that unstructured tetrahedral mesh in the boundary layers is a bad option for accuracy in the resolution of the boundary layer, places where  $y^+$  does exceed this limit is accepted. Advantages of the wall-funtion method, is that it is a robust solution and it saves computational resouces as it does not resolve the near-wall region [ANSYS, 2009c].

The discretization of the simulations is done in steps by initially using first-order upwind, then second-order upwind, and for the final solution the third-order MUSCL discretization scheme is used. These steps are done in order to secure a stable solution before proceeding with a higher order scheme. Opposed to the QUICK scheme which can only be used with a hexahedral mesh, the third-order MUSCL is applicable in all kinds of meshes, and therefore also the tetrahedral mesh used in this simulation. A third-order discretization scheme is applied to get the most accurate solution on the basis of the inputs such as mesh and Fluent the authors have specified. In comparison with the second-order upwind descritization scheme, third-order MUSCL can potentially give better accuracy of the simulation by the reduction of numerical diffusion. The effect of this is largest in 3D flows, as in this simulation. [ANSYS, 2009c] As the mesh is unstructured, and the mesh lines are not aligned with the flow direction, numerical diffusion will play a role when looking at the contour plots, as it will most likely smear out gradients.

## Boundary Conditions

The boundary conditions for the simulation are shown in table 7.3 on the next page. The inlet mass flows, temperatures and pressures are based on experimental measurements made on the SR-30 by fellow students [Jensen et al., 2012], as reported in section 6.6 on page 41. Calculation of the mass flows can be seen in section 6.7 on page 43. Note that the calculated inlet air mass flow from section 6.7 on page 43 is divided with 6 in order to have the correct mass flow in the 1/6 cut of the combustor. Late in the project period it was discovered that the mass flow of fuel in this simulation was specified as the total mass flow rate into the system, *i.e.* 0.004464 kg/s, and not the 1/6 of it. However as the so-called fuel mass flow in this simulation is air entering the flow field as a surface injection from the fuel inlet surface, it is assumed to have a minor effect on the purpose of the simulation. The primary purpose of this simlation is as mentioned earlier, to create a hot flow simulation to initiate the combustion simulation calculation. Hence it is not changed, as other parts of the report and simulations are prioritized.

**Table 7.3:** Boundary conditions setup for the non-reacting simulation.

Surface	Boundary condition	Mass flow [ $kg/s$ ]	Temperature [ $K$ ]
Air inlet	Mass flow inlet	0.05767 $kg/s$	1000 K
Fuel inlet	Mass flow inlet	0.004464 $kg/s$	1000 K
		Gauge pressure	
Outlet	Pressure outlet	192,161 Pa	-
Walls	Radiation	-	-
Side walls	Symmetry boundaries	-	

As seen in Table 7.3 a pressure outlet is specified on the outlet boundary. As the outlet on the geometry is placed at the end of the extra pipe attached, the pressure measurement at the turbine inlet, taken on the real SR-30 Turbojet Engine, can not be used directly on this boundary as the attached pipe will cause a pressure loss. The gauge pressure of 192,161 Pa is therefore found on the basis of initial simulations done on a similar Fluent case, but with gauge pressure of 219,000 Pa on the pressure outlet. As this showed a too large gauge pressure on the inlet boundary according to the experiment, the difference between the inlet gauge pressure measured in the experiment and the simulation result is calculated as

$$\Delta P = P_{inlet,simulation} - P_{inlet,experiment} = 247,839Pa - 221,000Pa = 26,839Pa \quad (7.4)$$

This is then subtracted from the gauge pressure on the outlet, to resemble the pressure loss in the attached pipe.

$$P_{outlet,simulation} = P_{outlet,experiment} - \Delta P = 219,000Pa - 26,839Pa = 192,161Pa \quad (7.5)$$

It yields a gauge pressure of 192,161 Pa on the pressure outlet, and this makes the pressure range of importance to the simulation close to similar with the experimental measurements. The measurements from the experiment is summarized in Table 6.2 in section 6.6 on page 41.

Radiation is enabled as thermal boundary condition on the walls. Internal (wall) and external (outer surface) emissivity is chosen on the basis of knowledge from the data sheet that the combustor material is Inconel 718 alloy. This value is then assumed to be  $\epsilon_{external} = 0.5$  [Ahn et al., 2010]. Additionally the External radiation temperature needs to be specified. This is assumed for each of the different surface parts in the combustor. For the outer walls this value is atmospheric temperature, and for the inner parts it is location dependent. Internal emissivities on the inlet and the outlets are specified to 0.8, on the basis of a dialog with Yin [2012] stating that normal values are in the range of 0.7-0.9.

A plug-flow is assumed in the mass flow inlet boundary condition. In reality this will not be the case, as the inlet is placed right at the exit of the centrifugal compressor in the SR-30. This will alter the shape of the velocity profile. The direction of the flow is set as to being normal to the inlet boundary, but this would also not be the case as it will have an some oblique direction from the inlet surface. The shape and precise flow direction of the inlet velocity profile is however not attainable, and for simplicity a plug-flow is used. To compensate for some of the turbulence that is present in the inlet air, Intensity and Hydraulic Diameter is used as the specification method for turbulence, and here the Turbulent Intensity is set to 17% which is typical for combustion air flows [ANSYS, 2009b].

On the basis of the non-reacting hot flow solution based on the setup presented, a combustion simulation is done, with the setup presented in the next section.

## 7.2.2 Combustion simulation

From the calculated flow field of the non-reacting simulation, a combustion simulation of the flow field is initiated. The following models are enabled; Energy, Viscous, Radiation, Species, and Discrete phase. The setup in Fluent are specified as seen in Table 7.4

**Table 7.4:** Fluent setup for the combustion simulation.

Setup parameter	Setting
Solver type	Pressure based
Turbulence model	$k - \epsilon$ realizable
Wall treatment	Standard wall function
Radiation model	P1
Species	Non-premixed combustion
Discretization	Third-order MUSCL
Underrelaxation factors	Default

As fuel and air inlets are situated separately in the geometry and are not mixed in advance, the non-premixed combustion model is used. Here it is possible to specify the oxidizer and the fuel species and concentration, and appoint them to separate inlets as needed.

Furthermore, the setup seen in Table 7.5 are applied to the non-premixed combustion model.

**Table 7.5:** Setups in the non-premixed combustion model.

Setup parameter	Setting
State relation	Steady flamelet
Energy treatment	Non-adiabatic
Operating pressure	101,325 Pa
Compressibility effects	Enabled
Inlet diffusion	Enabled
Boundary species	Mass fraction
Fuel (T = 300 K)	
$C_{10}H_{22}$	0.727
$C_6H_{14}$	0.091
$C_6H_6$	0.182
Oxidizer (T = 483 K)	
$O_2$	0.233
$N_2$	0.767

Initial simulations without compressibility effects enabled in the non-premixed combustion model showed very

high gas velocities and relatively large pressure changes due to the constriction of the fluid domain in the outlet tunnel. Therefore it is decided to include the compressibility effects in the simulation, which makes ANSYS Fluent update the density according equation 7.6.

$$\bar{\rho} = \rho_{op} \cdot \frac{\bar{p}}{p_{op}} \left[ \frac{kg}{m^3} \right] \quad (7.6)$$

Here  $p_{op}$  is the operating pressure [Pa],  $\rho_{op}$  is the density at the operating pressure [ $kg/m^3$ ], and  $\bar{p}$  is the mean pressure of a specific cell in the mesh [Pa]. When modelling the non-premixed combustion case this is the way to include compressibility effects, opposite other models where it is set in the Edit Materials setup.

Non-adiabatic simulation is enabled as the effects of radiation on the walls is taken into account, and inlet diffusion is enabled to also be able to take care of the diffusion component of energy transport at the inlet, as it depends on the temperature gradients of the flow simulation. The fuel and oxidizer species are obtained by importing the CHEMKIN mechanism and thermodynamic database which are presented in Appendix A, and the mass fractions are according to the surrogate fuel from Strelkova et al. [2007] presented in section 5.3.1 on page 31. Mass flow from the air inlet is as specified for the non-reacting case, *i.e.*  $\dot{m}_{air} = 0.05764 \text{ kg/s}$ . The mass flow of fuel is  $\dot{m}_{fuel} = 0.004464/6 \text{ kg/s} = 0.000744 \text{ kg/s}$ , and this is applied to the spray injection instead of the fuel inlet surface as in the non-reacting case.

### Steady Flamelet Model

Initially it was the intention to use the equilibrium state relation model in connection with the non-premixed combustion model. This however led to difficulties importing the CHEMKIN mechanism species into the material PDF mixture. Different approaches were tried both with the graphical user interface, and the textual user interface in ANSYS Fluent, but none of these solutions worked, as Fluent did not recognize the mechanism. Instead it is decided to use the steady flamelet model as state relation. With this model, it is possible to import the CHEMKIN mechanism and thermodynamic data directly inside the model setup user interface, which made Fluent recognize the mechanism and the species.

In general the flamelet model is capable of describing the interaction between turbulence and chemistry. It models the turbulent flame in a non-premixed combustion simulation as a gathering of steady laminar flames, which are called flamelets. ANSYS Fluent is able to calculate these opposed-flow diffusion flames/flamelets for a specific combustion case, and these are incorporated in a turbulent flame by the use of a Probability Density Function (PDF) where chemistry is tabulated and described by only the mean mixture fraction,  $f$ , and the scalar dissipation,  $\chi$ . This yields big computational savings in the simulation. [ANSYS, 2009c]

One limit of this model is that relatively fast chemistry is needed. It is capable of predicting chemical non-equilibrium which occurs when turbulence affects the flame with an aerodynamic strain. By assuming fast chemistry however, it is expected that the chemistry responds instantaneously to the strain, and as this strain fades to zero, the chemical reactions tend to reach equilibrium. Hence it can not model for example slow chemistry like  $NO_x$  reactions, where the fluid mixing time-scale is similar to the chemical time-scale. Also, when using the non-adiabatic energy treatment, the flamelet species composition changes due to heat loss or heat gain to the system and is not accounted for. For many combustion devices however this heat loss/gain can be neglected [ANSYS, 2009a].

The grid of the flamelets in this project is generated by the "Automated Grid Refinement" function. This

adaptive algorithm inserts grid points around the stoichiometric mixture fraction, which is assumed to be the peak temperature location, to make sure the change of values between two points is less than a user specified value. These tolerances are kept as Fluent default values, and the flamelet is generated based on this.

## Discrete Phase Model

Setup in the Discrete Phase Model (DPM) is as seen in Table 7.6

*Table 7.6:* Setups in the DPM model.

<b>Setup parameter</b>	<b>Setting</b>
Interaction with Continous Phase	Enabled
Continuous Phase Iterations per DPM iteration	50
Drag law	Spherical
Particle Radiation Interaction	Enabled
<b>Injection property</b>	<b>Setting</b>
Injection type	Solid-cone
Number of Particle Streams	50
Particle type	Droplet
Material	diesel-liquid
Evaporating species	C <sub>10</sub> H <sub>22</sub>
Diameter distribution	Uniform
Diameter	0.04 mm
Temperature	300 K
Spray direction	(x,y,z) = (0,0,-1)
Velocity magnitude	50 m/s
Cone angle	25°
Radius	0.65 mm
Total flow rate	0.000744 kg/s
Discrete Random Walk Model (DRWM)	Enabled
Number of tries in DRWM	10

As seen, evaporating species, which is the gas that is evaporating from the droplets, is set to C<sub>10</sub>H<sub>22</sub> as this is the major part of the fuel mixture. However when a fuel mixture is specified, as in the case of this simulation, ANSYS Fluent will make sure that all the fuel mixture spieces are included in the evaporated gas. The specified species is only used for calculating evaporation rate with regard to diffusion. [ANSYS, 2009d]

Previously mentioned in section 6.5 on page 40 the type of fuel atomizer on the SR-30 is not known, and information about it was not obtainable. Therefore atomizer property values of spray type, velocity magnitude, radius, and droplet diameter are all assumed values. This yields alot of uncertainty of the combustion pattern inside the combustor, as changing these values independently will alter it. But as the goal of the project primarily is to investigate soot formation from the soot precursor species present in the CHEMKIN mechanism, this is accepted.

Particle radiation interaction is activated to account for radiation heat transfer to the droplet particles. Boundary

conditions for the DPM model on all walls, is set to reflect particles from the wall and back into the fluid domain. The Discrete Random Walk model is enabled as turbulence and mixing plays an important role in the reactions, and 10 number of tries are specified.

### Moss-Brookes-Hall soot model

As an extra extension to the combustion model, the Moss-Brookes-Hall post-process soot formation model available in ANSYS Fluent is applied, to try and predict the soot formation from the precursor species available in the mechanism. This model is chosen as it is applicable for higher hydrocarbon fuels [ANSYS, 2009d]. The Moss-Brookes soot formation model solves the transport equations for the soot mass fraction and the normalized radical nuclei concentration, according to the equations which can be investigated in ANSYS [2009c]. Hall made an extension to this model as described below.

Moss-Brookes-Hall soot model base the initiation of the formation of soot on 2-ringed and 3-ringed aromatics ( $C_{10}H_7$  and  $C_{14}H_{10}$ ), formed due to acetylene, benzene and phenyl radicals, from the following reactions:

- $2C_2H_2 + C_6H_5 \Rightarrow C_{10}H_7 + H_2$
- $C_2H_2 + C_6H_6 + C_6H_5 \Rightarrow C_{14}H_{10} + H + H_2$

From data obtained by laminar methane flames, Hall modeled the soot inception rate to be 8 times the rate of formation of the  $C_{10}H_7$  and  $C_{14}H_{10}$  species [ANSYS, 2009c]. The model can only be applied for an ANSYS Fluent simulation when  $C_2H_2$ ,  $C_6H_6$ ,  $C_6H_5$  and  $H_2$  are available in the species list, which is the case for the imported CHEMKIN Mechanism.

The setup in the Moss-Brookes-Hall is seen in Table 7.7

**Table 7.7:** Setups in the Moss-Brookes-Hall soot formation model.

Setup Parameter	Setting
Precursors from Soot Precursors	species-list $C_2H_2$ , $C_6H_6$ , $C_2H_4$
Surface Growth	$C_2H_2$ , $C_6H_6$ , $C_2H_4$
Turbulence Interaction Mode	PDF Mode - Mixture fraction
Mass of Incipient Soot Particle	144 $kg/kgmol$
Mean Density of Soot Particle	2000 $kg/m^3$
Soot Oxidation Model	Lee
OH Model	Instantaneous
Soot-Radiation Interaction	Enabled

As seen the precursors are chosen from the species list from the CHEMKIN Mechanism, *i.e.*  $C_2H_2$ ,  $C_6H_6$ , and  $C_2H_4$ . The authors thought that  $C_6H_5$  would be present on the list as well as it is present in the reaction mechanism, but this is not the case. The turbulence interaction mode setup is set as mixture fraction, by recommendation from ANSYS [2009d] which state that for non-premixed combustion calculations this generally shows the best accuracy and results. Regarding the mass of incipient soot particle and mean density of soot particles, these are default values proposed by the Moss-Brookes-Hall model. The soot oxidation model is

specified as Lee, as this both take into account oxidation due to OH and molecular oxygen [ANSYS, 2009d]. Modeling parameters of the [OH] is set to instantaneous, as recommended by ANSYS [2009d]. To take into account the the radiation from the soot particles created by the model, the Soot-Radiation Interaction is enabled. This however requires the soot model not to be calculated entirely as post-processing, but with the other models enabled aswell. This was showed to be rather computational demanding, even with the relatively coarse mesh used in this simulation. It is however done, as it can be an important parameter on the radiation absorbtion coefficient.

**This chapter described the development of the ANSYS Fluent mode. From the developed CAD geometry of the 1/6 part of the combustor created in Solidworks, a mesh consisting of 600,000 elements is created in ANSYS Icem. This mesh is then imported to ANSYS Fluent, and the boundary condions and other setups presented here are applied to the case file. The next chapter treats the simulation convergence and results of the simulation. This is done with residual and contour plots, which are analysed and discussed.**



This chapter contains the results from the CFD combustion model of the SR-30 combustion chamber.

The planes used for the contour plots in this section are illustrated in Figure 8.1. Planes are hereafter referred to with numbers as seen in the illustration.

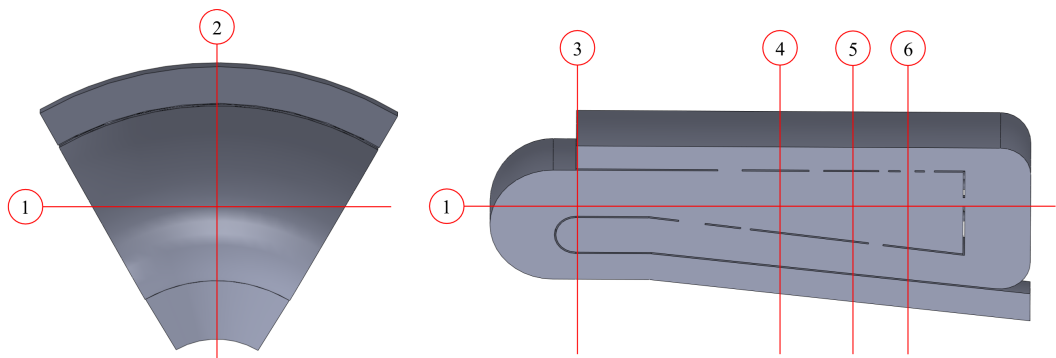


*Figure 8.1:* The different planes used for contour plots in this section.

## 8.1 Results from the Combustion Simulation

In this section the simulation results for the combustion simulation are shown. Contour plots of temperatures, velocities, species mass fractions, and droplet pathlines are presented and analysed based on the theory of soot formation presented in chapter 3 on page 15. It is emphasized that even though it is desired to resemble the general flow field and experimental results from the SR-30 Turbojet Engine as good as possible, the alternations of the geometry will have an impact on the simulation result. The alternations include removal/adding of liner holes to obtain a symmetric cutout of the geometry, and small changes in the dimension, as described more thoroughly in section 7.1 on page 45. Also, as mentioned in section 7.2 on page 54, knowledge about the atomizer and its properties was not obtainable which also adds uncertainty to the comparability with the SR-30.

### 8.1.1 Convergence of the Simulation

The mass and energy fluxes for the simulation is shown in table 8.1. It is seen that the error in both the net mass flow rate and the net total heat transfer rate is very low, and the small change is treated as negligible to the solution. This report goes for all the contour plots in this section and in Appendix C, as they are exported from the same simulation.

**Table 8.1:** Net mass and energy flux reports from the combustion simulation in ANSYS Fluent.

	Net result	% Error, relative to mass/energy into the system
Mass Flow Rate	$1.615 \cdot 10^{-6} \text{ kg/s}$	$2.766 \cdot 10^{-5} \%$
Total Heat Transfer Rate	-13.63 W	$1.2 \cdot 10^{-3} \%$

Residuals for the simulation are shown in Figure 8.2. This shows the previous iterations done with both the first-order and second-order upwind, as well as the last iterations with the third-order MUSCL scheme. The part showing the residuals from 3000 to approximately 6000 have somehow been altered by ANSYS Fluent, which should be clear when looking on the figure. It is as if it skips the majority of the residual steps, and take big jumps with the curves. This part of the plot should be ignored, and only account the iterations >6500.

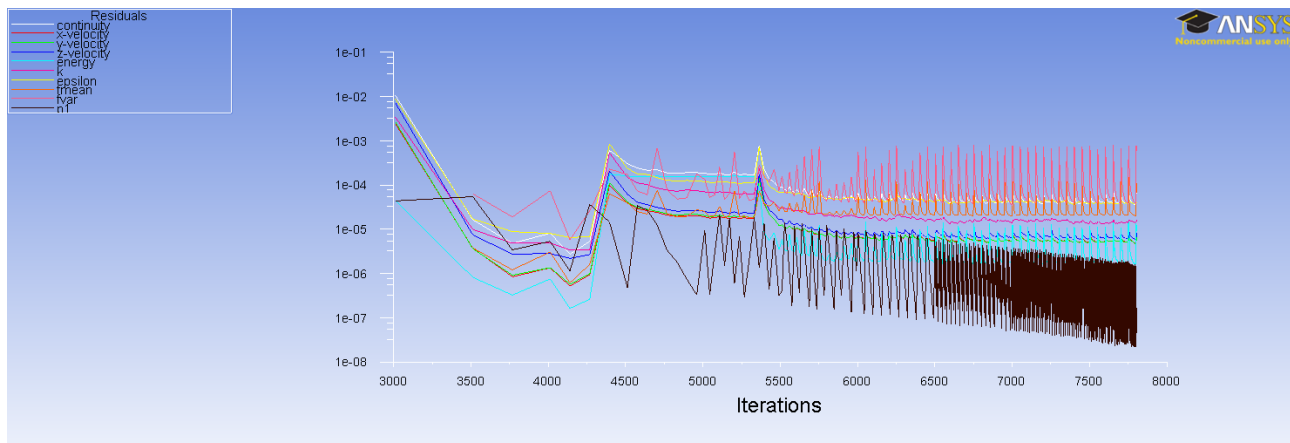


**Figure 8.2:** The residual plot for the combustion simulation.

Furthermore a point in the inlet, in the dilution zone area, and in the outlet is used as monitors to check the temperature and velocity development in the calculation of the solution. These all show a satisfactory stable tendency, which also indicate a converged solution.

Figure 8.3 on the facing page shows the mass imbalance of each cell in the mesh, at the centered vertical plane. It is seen that the overall mass imbalance is in the range of  $10^{-9}$ , which is also seen as an acceptable error with minor influence on the simulation. Looking at other different planes of the simulation, gives the same picture of the error as it stays in the range of  $10^{-8}$ - $10^{-10}$ .

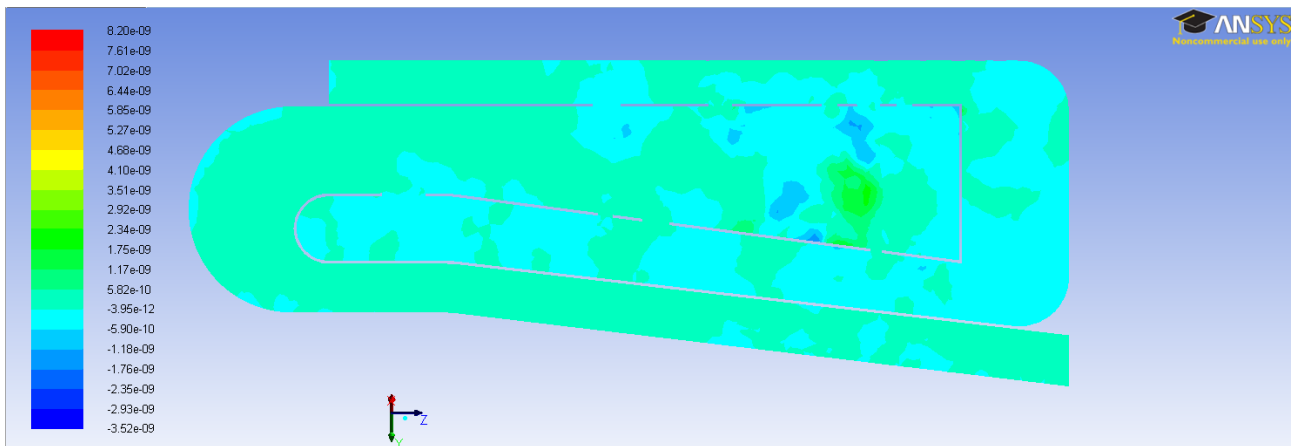


**Figure 8.3:** Mass imbalance countours on plane 2. In units of  $[kg/s]$

Hence the simulation is concluded to be reliable according the residuals and mass/energy balances. The next section will present the results obtained from the simulation.

### 8.1.2 Combustion Simulation Results

The static presure contours on plane 2 is seen on Figure 8.4. The goal with this contour is to resemble the gauge pressures measured in the experiment by Jensen et al. [2012] at the compressor exit and the turbine inlet measured to approximately  $221,000 Pa$  and  $219,000 Pa$  respectively. It should be noted that these gauge pressures fit quite well with the engine compression ratio defined by the manufacturer, which is given to be 3.4:1, as seen in Table 6.1 on page 39.

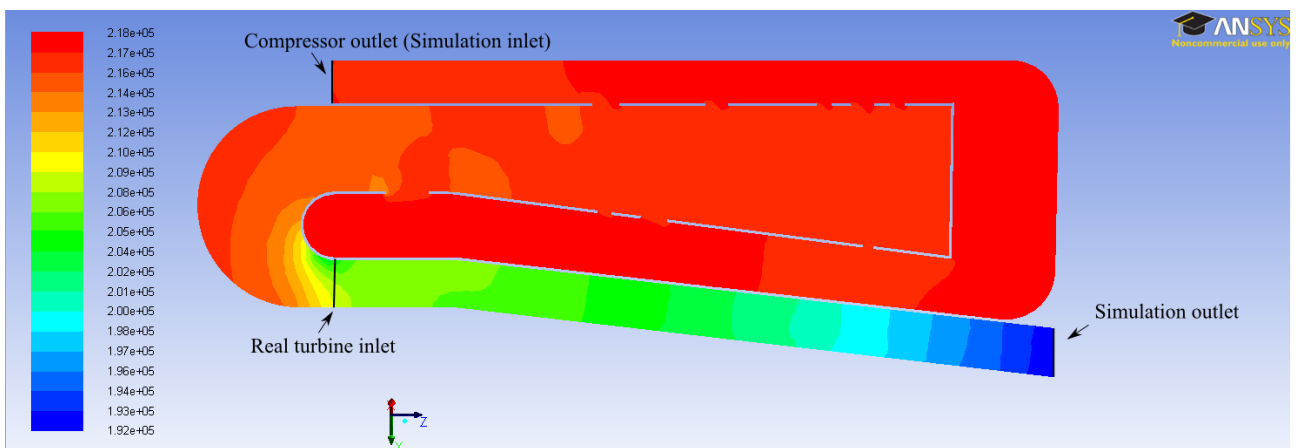


**Figure 8.4:** Static pressure contours on plane 2. In units of  $[Pa]$

On the contours, the gauge pressure at the inlet can be seen to be 218,000 Pa, which resembles the gauge pressure measured well. The placement of the turbine inlet on the contours is marked on the figure. Here it is seen that the simulated pressure is a bit underpredicted according to the experiment. Where exactly the pressure measurement sensor is placed is not known though, and this obviously has an impact in what the measurement shows. Chances are it is placed a distance longer into the bend of the combustor guiding vanes etc. are placed at the real turbine inlet. The longer away from the turbine inlet, the higher the gauge pressure as seen from the simulation. So a value somewhere in the interval of 206,000 Pa to 214,000 Pa is shown from the simulation, depending on where the gauge pressure is measured. All in all, however, it is decided that it agrees with the experiment acceptably well. Taking into account the alterations of the design, a 100 % resemblance is not expected.

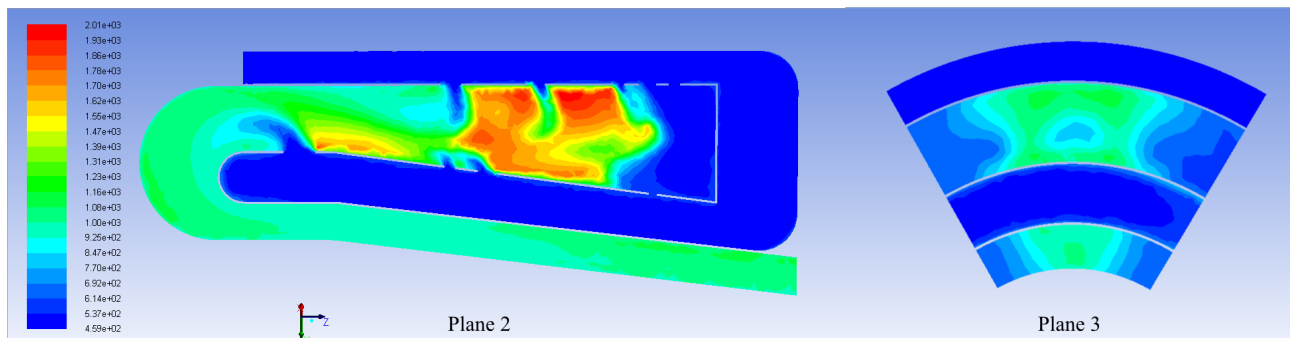


**Figure 8.5:** Static temperature contours on plane 2. In units of [m/s]

In Figure 8.5 the temperature contours are seen on plane 2 and plane 3. Here the temperature from the simulation is again compared to the temperature obtained from the experimental measurements at the turbine inlet, which yields a temperature of 915 K. Looking at the temperature contours of the simulation, the value of this is also highly dependent on where exactly in the flowfield the temperature is obtained. As seen in the outlet duct cross section of plane 3, taking the temperature in the center of the area shows a temperature of around 900-1000 K, and close to the symmetry surfaces it shows a temperature of around 600-700 K. Therefore it is hard to directly validate the simulation according to the outlet temperature, but it seems to be in a reasonable range of the experimental results. The big change of temperature is because of the big dilution liner holes adding a lot "cold" air to exhaust mixture.

Velocity contours of the flowfield on plane 2 is shown in Figure 8.6 on the facing page. It is seen on both Figure 8.5 and Figure 8.6 on the facing page how the air flowing through the liner holes, is accelerated and is penetrating into the combustion zone to mix with the hot gasses present there. However the representation and accuracy of this acceleration and spread is compromised by the k- $\epsilon$  model as described in section 7.2 on page 54. The maximum velocity in the outlet tunnel reaches approximately 200 m/s. However, only velocities up to 125 m/s are shown, to give a better resolution of the gradients inside the combustor. The increase of velocity in the outlet duct is, as mentioned before, because the cross sectional area of the duct is decreasing through the length of it, as seen in Figure 7.5 on page 48 in section 7.1 on page 45.

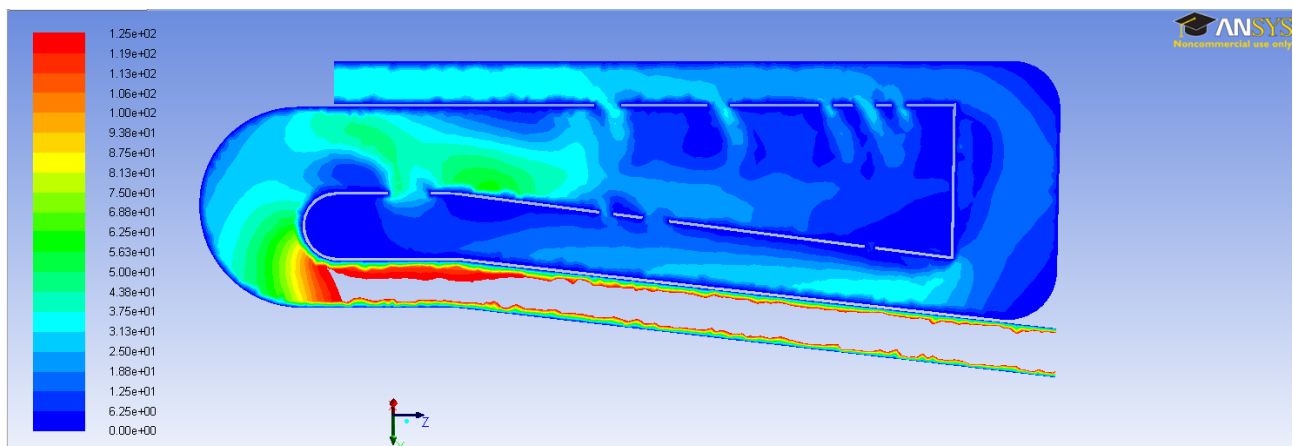


**Figure 8.6:** Velocity magnitude contours on plane 2. In units of [m/s]

In Figure 8.7 pathlines of the air entering the inlet are shown all the way through the combustor. It is clear that most of the air is entering the combustion zone through the bigger dilution holes farthest away from the fuel inlet, both on the outer and the inner liner to cool the outgoing exhaust gas. A smaller amount of air is entering the liner holes in the intermediate and primary area of the combustor. Here the major part of this is entering from the outer liner side, while it seems most of the air pass the holes on the end and inner liner, atleast in the primary zone.

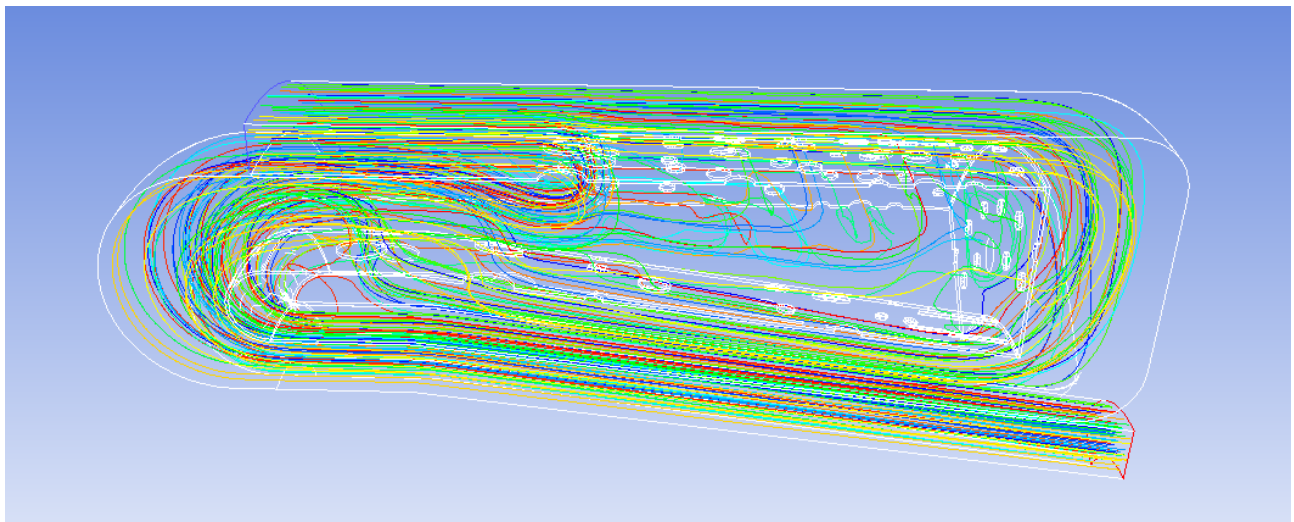


**Figure 8.7:** Velocity magnitude contours on plane 2. In units of [m/s]

The particle tracks and the evaporation rate of the inserted droplets are shown in Figure 8.8 on the next page from two different perspectives. As the path lines vanishes, the droplets are evaporated to the gas phase species specified in the fuel mixture. Investigating the figure, it is seen that the droplets closest to the outer liner are evaporated prior to the evaporation of the droplets closer to the inner liner. Referring to the Figure 8.7 it is evident that a higher mass flow of air is entering the primary zone from the outer liner. Hence this will cause a better mixing and a higher convectonal heat transfer to the droplets closer to the outer liner, and cause them to evaporate faster than the ones approaching the inner liner. Furthermore it is seen that because of the

reflecting boundary condition on the walls, droplets reaching the inner liner are reflected and reenter closer to the intermediate zone where they are evaporated. It is seen from the scale that the droplets approximately are resident inside the combustion chamber for  $9 \cdot 10^{-4}$  to  $2.349 \cdot 10^{-4}$  seconds for the longest droplet track.

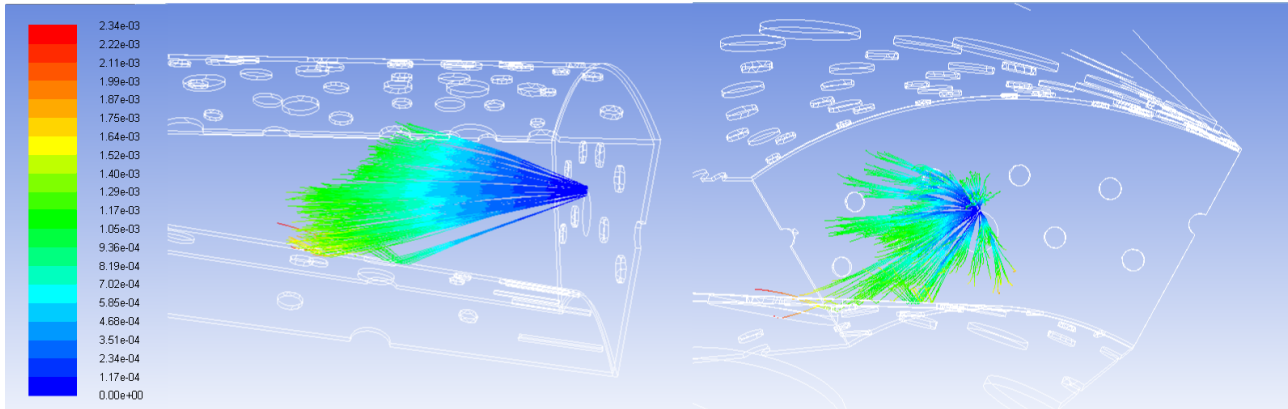


**Figure 8.8:** Pathlines of the droplets into the fluid domain, colored by residence time. In units of [s]

Contours of mass fractions of the different set precursors and other species on plane 2 are seen on the next two pages. These are further discussed in the next section. In Appendix C more contours are shown with species and temperature on planes 4, 5 and 6 along with mass fractions of benzene, ethylene, acetylene and OH on plane 1. These can be looked at to give a different perspective, and get a better picture of the overall contours.

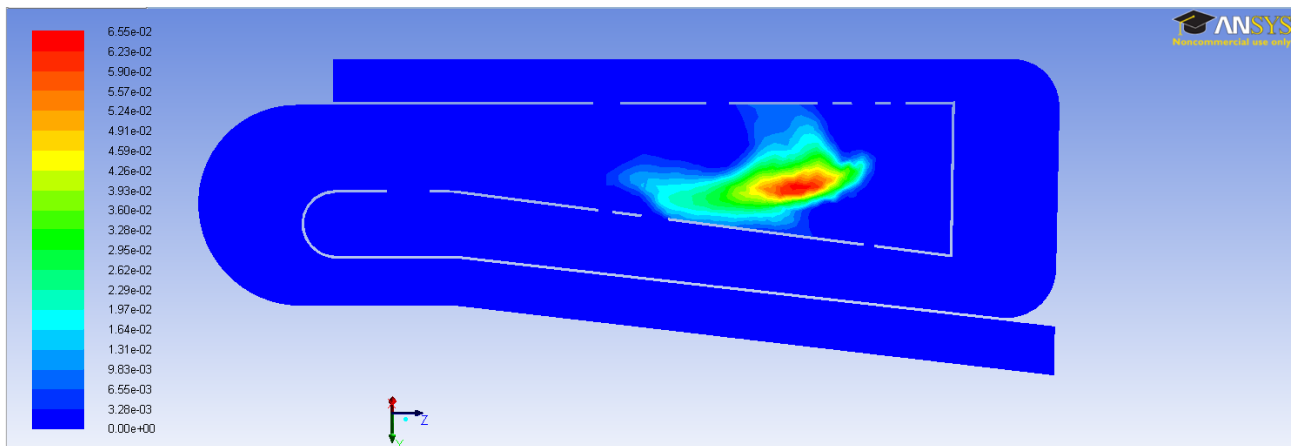


**Figure 8.9:** Mass fraction contours of benzene on plane 2.

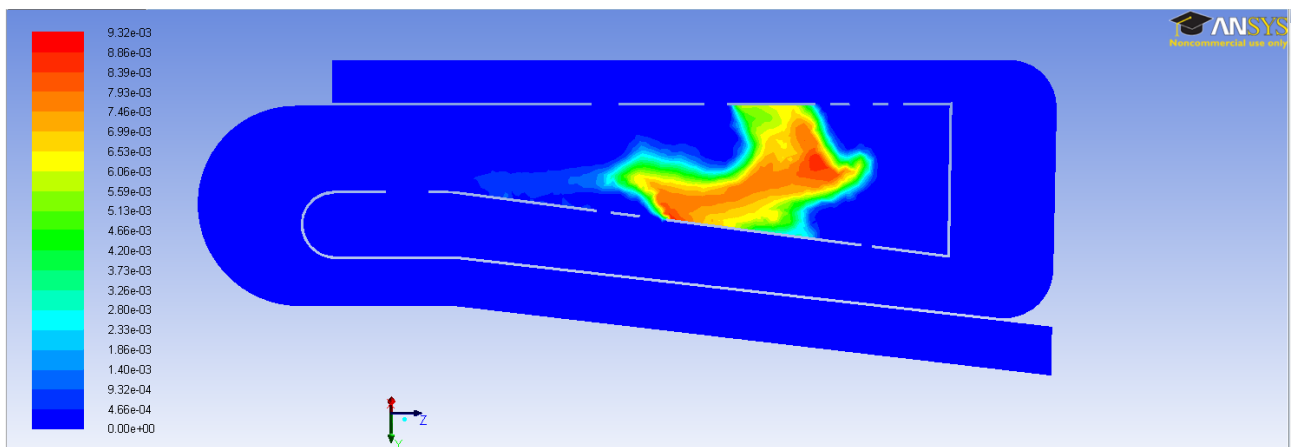


**Figure 8.10:** Mass fraction contours of ethylene on plane 2.

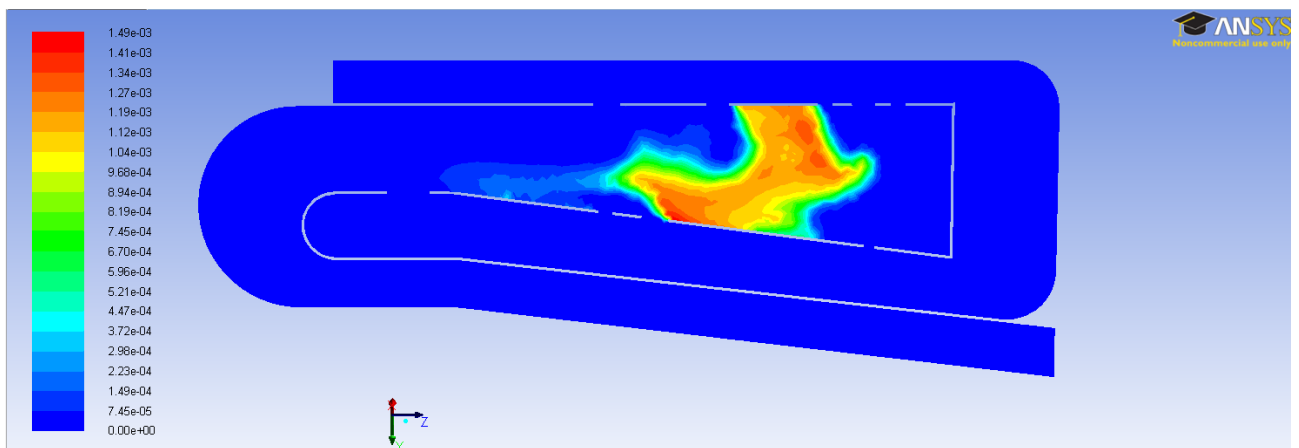


**Figure 8.11:** Mass fraction contours of acetylene on plane 2.

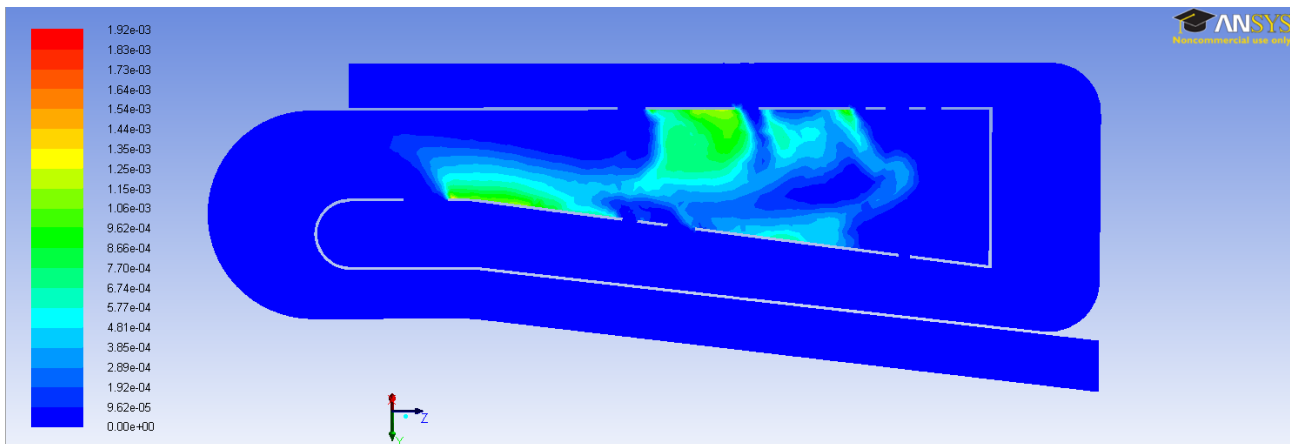


Figure 8.12: Mass fraction contours of OH on plane 2.

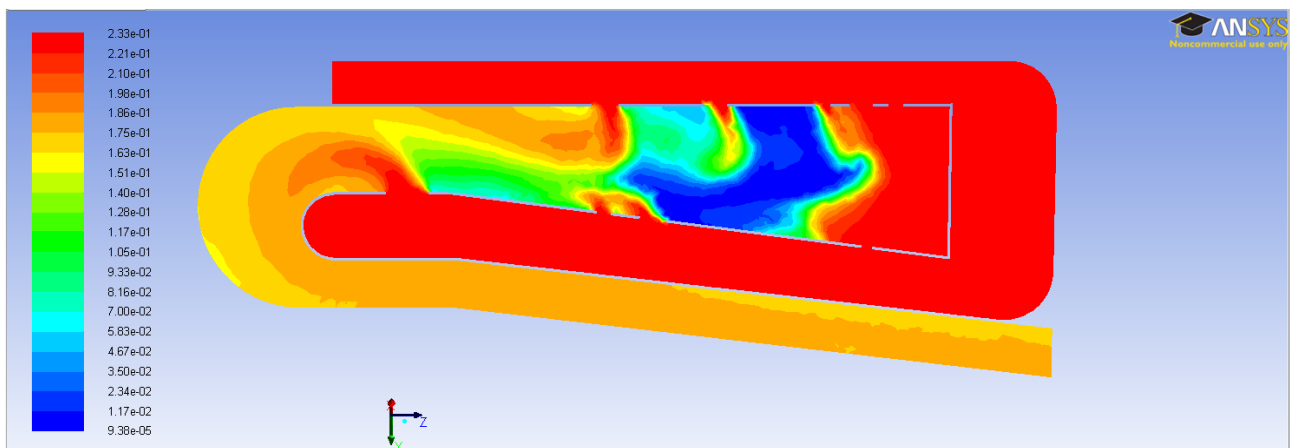


Figure 8.13: Mass fraction contours of  $O_2$  on plane 2.

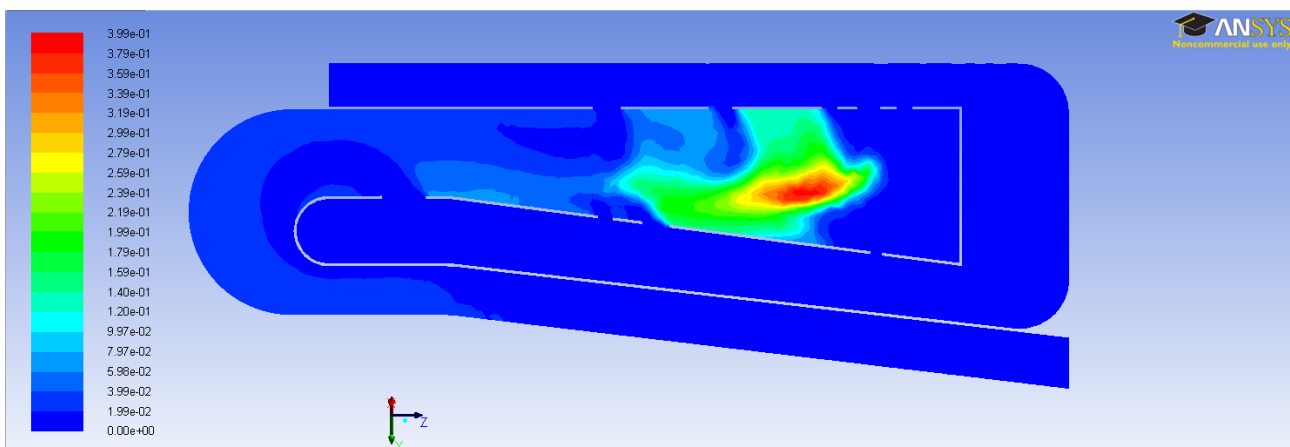


Figure 8.14: Mean mixture fraction contours on plane 2.

## 8.2 Soot Formation Discussion

This section contains an analysis and discussion of the CFD simulation results, regarding the formation of soot from the soot precursors included in the reduced mechanism, shown in section 5.3.1 on page 31. The discussion is based on the knowledge gained in chapter 3.2, and the that soot is mentioned in the Project Description.

It should be noted that because PAHs are not included in the reduced mechanism incorporated in the CFD simulation, a complete description of the reaction pathway of soot formation is not possible to predict. The soot formation pathway which is investigated hereunder is based on assumptions made by looking at the contour plots combined with knowledge of soot formation obtained through the project. The presence of PAHs in the combustion chamber can not be seen on any contour plots which again makes it impossible to validate the described pathway, but a discussion of a possible pathway is made.

Figures 8.9, 8.10 and 8.11 on page 69 show the mass fractions of benzene, acetylene and ethylene respectively, which all are referred to as precursors to soot formation. It is seen that the mass fractions contours of acetylene and ethylene seems to be very equal, predicting the highest mass concentrations of each species in the same area. The higher mass fractions of benzene is also present inside this domain, along with the other specified fuels, decane and hexane, which indicates that most of the droplets are evaporating here, which is also seen in Figure 8.8 on page 68. Hereby all the defined precursors are present in the same area, which could indicate that soot formation does occur. Adding this with the high temperatures that are present in the area as well, as seen on the temperature contours in figure 8.5 on page 66, it further promotes conditions favoring soot formation which are described in section 3.3.1 on page 25. Hence the formation of PAHs, like naphtalene, can be assumed to happen from the growth of acetylene and ehtylene on benzene and phenyl radicals, thereby the basis for soot formation is present. In Appendix C the mass fractions on planes 1, 4, 5, and 6 are shown, for a better perspective on the overall distribution in the combustor.

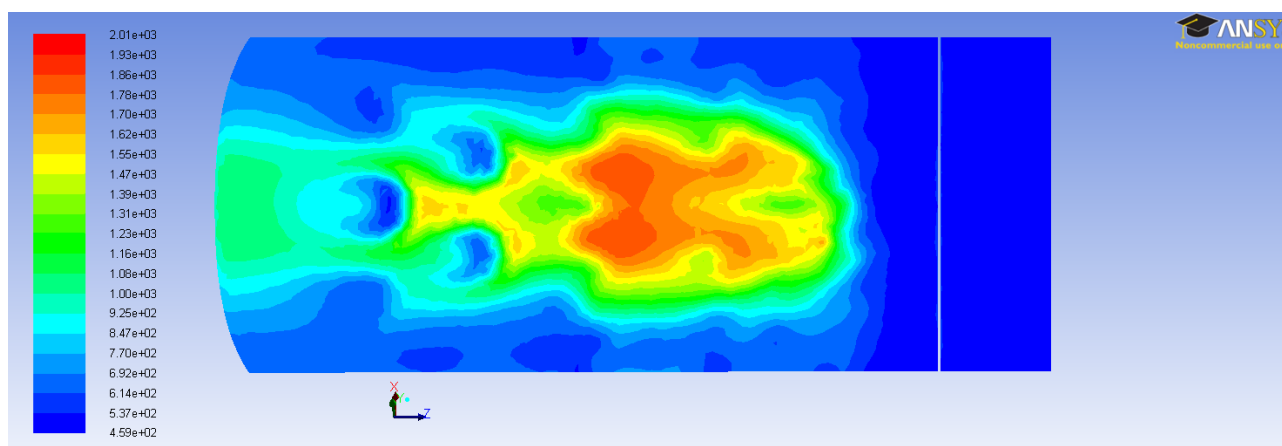


**Figure 8.15:** Static temperature contours on plane 1. In units of [K]

Further growth of the naphthalenes is much more complex to predict from the simulation results, as PAHs are not present in the mechanism species. Figure 3.9 on page 25 shows that  $C_2$  isomers can add to naphthalene and form a larger PAH, that again can facilitate growth to larger PAHs. This is able to happen in the area where these  $C_2$  isomers are present with the PAHs.

Kennedy [1997] describes that soot is formed early in the flame, and that the following oxidation of soot happens at and after the flame tip. Thus the soot particles are considered to be formed before the tip of the flame, which

is also seen to be happening as the precursors are present in the high temperature flame zones. Due to the holes in the liners fresh air is continuously disturbing the flame, and it makes it difficult to visualize the precise shape of the flame. Figure 8.15 and 8.16 give the best picture of a continuous flame, and the high temperature and low  $O_2$  concentration area it covers.

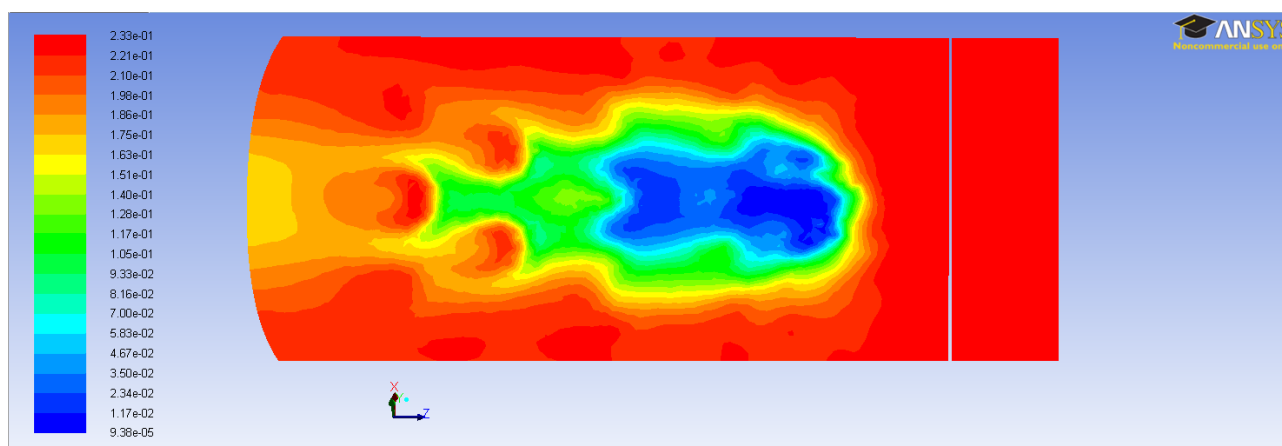


**Figure 8.16:** Mass fraction contours of  $O_2$  on plane 1.

From Figure 8.10 and 8.11 on page 69 it is seen that both ethylene and acetylene are present further downstream of the main "formation area" where the high mass fractions are observed, although in lower concentrations. Looking at Figure 8.15 on the previous page, it is observed that these lower concentration zones are present in a high temperature area. This indicates that the PAH growth reactions described above from Figure 3.9 on page 25 in section 3.3.1 on page 22 can possibly happen here, and further facilitate the formation of larger PAHs from the addition of acetylene and ethylene. Following the reaction pathways in Figure 3.9 from naphthalene with the addition of  $C_2$  isomers (as only these are present in this simulation in form of acetylene and ethylene) the PAH "cyclopenta acenaphthylene" is presumably able to be formed within the flame, with the very limited species and precursors present in this simulation. However, if it is desired to investigate all the different paths to the larger PAHs, a much more detailed mechanism is needed which includes the different  $C_1$ ,  $C_2$ ,  $C_3$  and  $C_4$  isomers that are all participating in the formation of larger PAHs, and information of the reactions building up the larger PAHs.

Soot is the result of the growth and nucleation of PAHs to nuclei, which is in the size range of UFPs and are further developed via agglomeration and coagulation. Thus since the PAH "cyclopenta acenaphthylene" presumably is present in the combustion chamber, this can nucleate to form soot. Gas-phase species like acetylene, ethylene, benzene and the vinyl-radical are present in the combustion zone and therefore it is possible for these species to cause the soot nuclei to grow by agglomeration and coagulation. It is therefore likely that soot is formed in the combustion zone. With the presence of soot in the flame postulated, on the basis on the statement in the Project Description, UFPs are assumed to be present as well.

Oxidation of the soot happens at, and after, the flame tip, as mentioned above. From Figure 8.14 on page 70 it is seen that low fuel concentrations are present in the area outside of the flame, as it is of course taking part in the reactions happening inside the flame. It is thus seen that most of the combustor area is fuel-lean, for which  $O_2$  is the dominant species that oxidizes the formed soot.  $OH$  also helps oxidize the soot as described in section 3.3.1 on page 25, but  $O_2$  is the major oxidizer in a fuel-lean combustor. Looking at Figure 8.16 and 8.13 on page 70 it is seen that high concentrations of  $O_2$  is present in most of the combustor, except for the

flame zone, where the  $O_2$  is used to oxidize the fuel. The majority of the OH is present in the flame zone, and only small concentrations away from it, and hereby in this case does not contribute significantly to the oxidation process of the soot. It is assumed that due to the presence of  $O_2$  and soot, soot is likely to be oxidized by the  $O_2$ , possibly causing part of the soot particles to burn-out and vanish before exiting the combustor. In section 3.3.1 on page 21 it also is described how the mature soot nuclei under pyrolytic conditions, *i.e.* at high temperatures and in the absence of oxygen, can be converted to a carbonaceous solid in the intermediate zone. This can also be the case for the soot formation described here, as the flame, and thereby the low oxygen region, is partly located in the intermediate zone might facilitate the altering to the carbonaceous solid.

With having analysed and discussed the possible formation of soot in the combustion simulation, this is further investigated by the attempt to implement the Moss-Brookes-Hall soot formation model incorporated in ANSYS Fluent. This is done to possibly be able to see that same tendencies which were predicted and described in this section.

### 8.3 Results from the Combustion Simulation incl. Moss-Brookes-Hall Soot Model

In this section the results from the combustion simulation with the Moss-Brookes-Hall Soot model are presented. This model is a post-process model available in ANSYS Fluent, and is applied to the reacting case solution, and then calculated. The model is applied as it possibly can show similar sooting tendencies as discussed above based on the theory obtained through the project. It also makes it possible to compare the soot model with the predicted soot pathway.

#### 8.3.1 Convergence

Table 8.2 shows the net mass and energy flux reports, which both show a negligible small error according to the inlet of mass/energy into the system.

**Table 8.2:** Net mass and energy flux reports from the combustion simulation including soot post-processing in ANSYS Fluent.

	Net result	% Error, relative to mass/energy into the system
Mass Flow Rate	$3.006 \cdot 10^{-7} \text{ kg/s}$	$5.149 \cdot 10^{-6} \%$
Total Heat Transfer Rate	-13.65 W	$1.21 \cdot 10^{-3} \%$

In ANSYS [2009d] it is stated that the residuals included for the soot model, *i.e.*  $\text{pollut}_{\text{soot}}$  and  $\text{pollut}_{\text{nuclei}}$ , should reach  $10^{-6}$  for a fully converged solution, and thereby a fully developed nuclei and soot field. Even though different schemes and lower underrelaxation factors were tried in different combinations, it was not possible to make the residuals reach  $10^{-6}$ . As seen in Figure 8.17 on the following page they only reach the range of  $10^{-4}$ - $10^{-5}$ . Therefore, it is evident that the solution showed here is not fully evolved. However, even though it might not be fully developed, it is decided to show the tendencies of the solution. The solution shown here has default underrelaxation factors, which were shown by trial and error to be just as good as other combinations of underrelaxation factors, with regard to residual magnitudes. Again the first part of the residual

plot should be skipped, as only the residual above 6500 is valid as ANSYS Fluent somehow altered the first part.

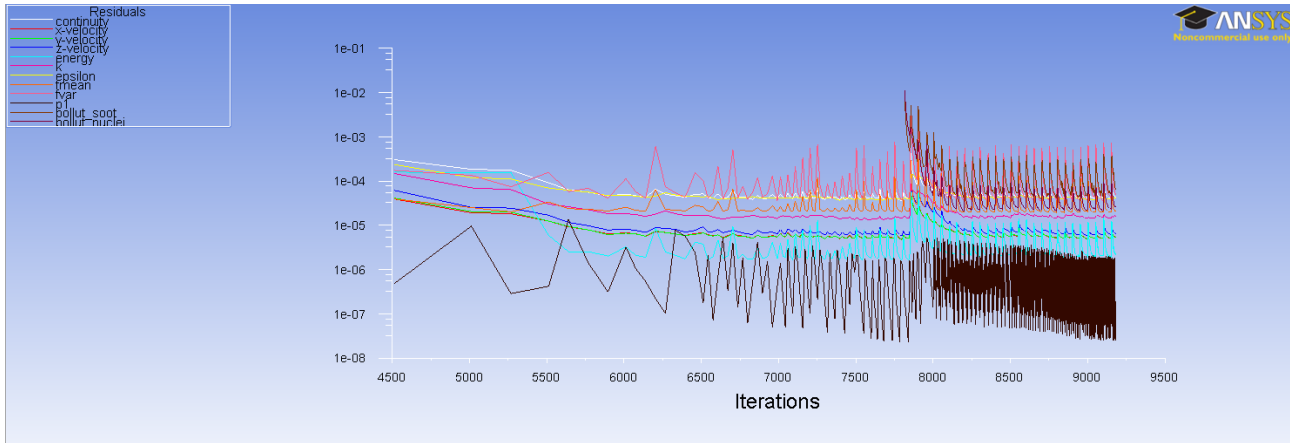


*Figure 8.17:* The residual plot for the combustion simulation with the soot model enabled.

### 8.3.2 Results from the Soot Simulation

Figure 8.18 shows the contours of the soot calculations done by the Moss-Brookes-Hall soot model. Comparing with the discussion above of possible soot formation tendencies inside the combustor, these results seem to agree with the predictions. The soot seem to form in the high temperature region, where the soot precursors are present and are able to initiate the formation process, and complete the formation of soot particles. If a further trace of these soot concentration is wanted, a transient solution must be applied. This could give a picture of the soot formation and degradation over time in the combustor.

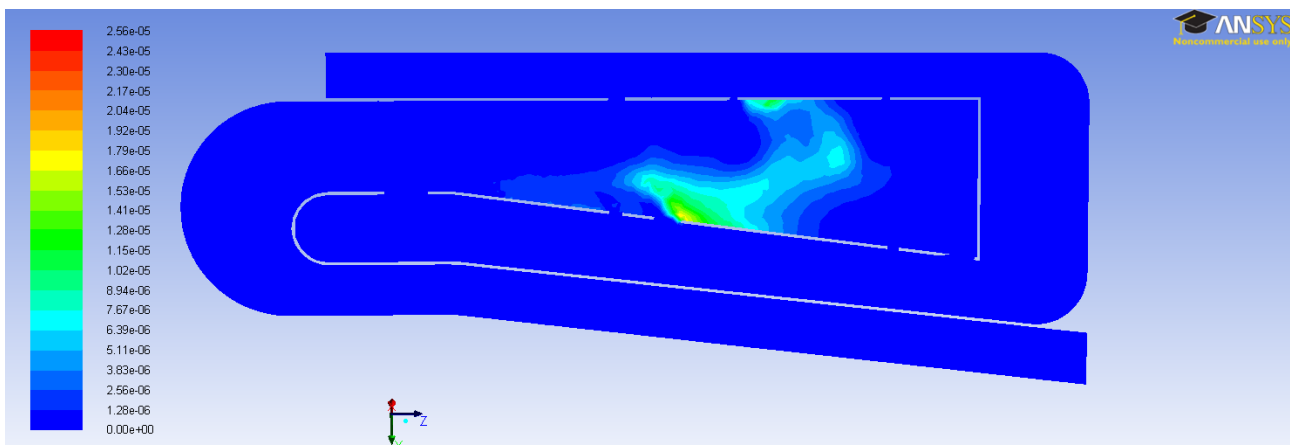


*Figure 8.18:* Contours of mass fraction of soot.

With the prediction of soot formation from the combustion simulation analysed and discussed, this shows that according to the theory and knowledge obtained through the project, that the basis for soot formation is present. However, as a reduced mechanism is used, with only a few of the possible soot precursors and no reactions for the formation of larger PAHs, there is no hard evidence for the further formation

**and nucleation of the soot particles. To obtain a better picture of the soot formation process, a larger more detailed mechanism would be interesting to implement, as to be able to track more soot precursors, and the mutual reactions of these to create PAHs.**



---

## Conclusion

---

# 9

The motivation of this report is based on the the evidence that UFPs emitted from the aeroengines and APUs on commercial airplanes are harzardous, and potentially lethal for especially people working in the surrounding areas at airports. With this in mind, there is an increasing interest in how these particles are formed inside the combustion chamber of the aeroengines, and how they can be reduced.

In this project, a 3D numerical study in ANSYS Fluent of one sixth of a combustion chamber in an aeroengine is conducted, to investigate and predict the formation of UFPs from the combustion of the jet fuel, Jet A, based on the formation of soot. The choice of Computational Fluid Dynamics for the modelling of this subject is made, as it makes it possible to investigate the local conditions and distribution of the temperature species present, and from this be able to predict the formation of UFPs based on theory and knowledge obtained of soot formation.

Initially a literature study of the properties and composition of the Jet A is done, to get basic knowledge of the different hydrocarbon molecules which constitute the main component of jet fuels. Here it is found that a normal jet fuel consist of approximately 60 % straight chained paraffins, 20 % naphtalenes and 20 % aromatic compounds. If aromatic compounds are present in a fuel the formation of soot is increased, which is why aromatic free fuels like biodiesel are interesting.

Detailed descriptions of particles and the formation of soot is presented, in which different reaction pathways for soot are described. A key species for the formation of soot is the presence of an aromatic ring, either phenyl-radical  $C_6H_5$  or benzene  $C_6H_6$ . The size of first aromatic ring is then increase by addition of different gas-phase species like acetylene,  $C_2H_2$ . Through these additions PAHs are eventually created, which then nucleate to form a soot nuclei. This soot nuclei then grows via agglomeration and coagulation to form the soot particle.

A reduced mechanism is chosen for use in the CFD simulation, which models the combustion characteristics of Jet A, and not the creation of PAHs or soot. However it was chosen because it contains the soot precursors  $C_2H_2$ ,  $C_2H_4$ ,  $C_2H_3$ ,  $C_6H_6$  and  $C_6H_5$ , from which it is able to predict the initial steps of soot formation, as described from the Figures 3.8 and 3.9 in section 3.3.1 on page 22. It is considered important to correctly model the combustion of Jet A, otherwise the formation of soot is not correct. The following three points are specified as important for the reduced reaction mechanism describing the combustion:

1. The surrogate fuel resembles the real fuel
2. The combustion characteristics of the surrogate corresponds to the real fuel
3. The degree of detail; It is computational advantageous and necessary to use a reduced number of reactions and species

This means that eventhough the reduced reaction mechanism does not model the formation or oxidation of PAHs or soot particles, the combustion characteristics is still modeled in a satisfying way, which is the basic for predicting a correct soot formation pathway.

As the reaction mechanism is used in the CFD simulation a chapter describes the combustion chamber which is modeled. The modeled combustion chamber of the aeroengine is that of a small scale test gas turbine, specifically a SR-30 Turbojet Engine, which is available for the authors of this report. Experiments are conducted on the turbine by fellow students, and their results are used in this report. The students measured fuel mass flow, pressure and temperature, which are directly, or via calculations, used as setup and validation of the numerical simulation done in ANSYS Fluent.

A non-reacting, hot flow CFD simulations serves as an initial solution of the combustion chamber, and is used as a basis for a reacting CFD simulation. The reacting case simulation is a non-premixed combustion of the surrogate fuel from the reduced mechanism and air. The reduced reaction mechanism is added to Fluent, and droplets are injected into the combustion chamber as a liquid fuel which then evaporates to the surrogate gaseous fuel.

The results of the reacting case simulation showed to match the experiment results quite well, even with alternations of the design in the geometry. The CFD simulation results also varifies that CFD indeed is a good way of modeling the combustion as local concentrations of the different soot precursors can be seen, as well as how the temperature in the chamber is distributed. This makes it possible to predict what the soot formation pathway might look like.

The predicted soot formation pathway is made using the results of the CFD simulation, and the theory of soot formation. The results of the CFD simulation show that benzene, acetylene, ethylene and high temperatures are present in the same area. From these facts a soot formation pathway is predicted using soot formation theory. The pathway is that the polycyclic aromatic hydrocarbon, "cyclopenta acenaphthylene", is formed within the flame by the addition of ethylene to the 2-ring polycyclic aromatic hydrocarbon, naphthalene, that is formed from addition of acetylene and ethylene to benzene. It is assumed that the "cyclopenta acenaphthylene" can nucleate to form soot nuclei, which then can grow to a soot particle. With the assumeably presence of soot particles it shows the presence of UFPs as well.

This shows that even with a reduced reaction mechanism that is created to model the combustion characteristics of Jet A using a surrogate fuel, and which does not predict the formation of PAHs or soot, a soot formation pathway is still predicted by using the theory of soot formation.

The post-process soot model, Moss-Brooke-Hall, available in Fluent is used to model the soot formation, to compare the predicted soot formation pathway. It was not possible to make the model fully converge, and the solution is therefore not completely evolved. The results however indicate that the predicted soot formation pathway might be correct, as the presence of soot is seen in the zones predictd.

It is believed that a similar approach can be used for other applications or fuels, for example diesel engines or biodiesel as a fuel, which would make it possible to describe the formation of either PAHs, soot or UFPs. It should be noted though, that the predicted soot formation pathway is only one of many pathways. A much more detailed mechanism is needed in order to predict all of the different PAHs that can nucleate to form soot nuclei. The computational requirements and time needed for a simulation using a detailed reaction mechanism, that contains all of the soot precursors, would however be very comprehensive.

This chapter discusses further possible work that can be done to extend the work done in this project. Several things can be done as mentioned below.

An obvious extent to this project would be the use of a detailed mechanism in order to capture all/most of the intermediate species in the mechanism, which also means more soot precursors can be identified. This would not only give a more correct picture of the soot formation process, but also a more correct solution of the kinetics of the combustion.

A transient CFD model would make it possible to see the formation process of soot as the fuel is injected into the combustor. Combined with a detailed reaction mechanism this would be a somewhat ideal model of the soot formation. However it would require a very large computational power, as well as be a very time consuming process.

It would be interesting to investigate different load scenarios on the turbine, and thereby determine what influence different loads have on the formation of particles. 3 scenarios could for example be used; "Idle", "Taxing" og "Takeoff". This would map the soot formation from the jet engine for different engine loads, which could help establish more knowledge on this matter.

A parameter variation of different settings in the CFD model would also be interesting. As mentioned in section 3.3.1 on page 25 a lower cone angle makes the combustion zone more fuel-rich, and it would be interesting to prove this by testing it in the CFD model. Effects of a variation of droplet size, and droplet velocity would also be interesting, to help determine the ideal settings of these values.

As mentioned in section 7.1 on page 45 a partly or full structured mesh of the geometry could have been made, as well as a more fine mesh. This would increase the accuracy of the simulation due to for example smaller numerical diffusion, and better calculation of the boundary layers.

Biodiesel was mentioned as an alternative fuel to conventional jet fuel. Using a biodiesel or a surrogate of biodiesel in the CFD model would enable the comparison of the fuels, and highlight the pros and cons of either fuel relatively to each other. A literature study of available reduced reaction mechanism for the combustion of biodiesel was made in this project, but as no suitable mechanism, of a reasonable size, was found it was not reported.

Another addition to this project would be the use of a User Defined Function in Fluent. The UDF should be able to predict the formation of soot, given specified conditions, and show different sizes of the formed soot particles. This would show much more detailed soot formation pathways, and would give a more correct picture of the formation pathways.



# Bibliography

- AeroMexico (2012). AeroMexico, ASA, and Boeing announce the first transcontinental flight in aviation history to use biofuel. Accessed 17-05-2012, from the website <http://www.aeromexico.com/us/ExperienceAeromexico/AeromexicoCorporate/PressRoom/Green-flight.html>.
- Ahn, D., Byun, K., and Kang, M. (2010). Thermal characteristics in the cutting of inconel 718 superalloy using cw nd: Yag laser. *Journal of Material Science and Technology*, 26:362–366.
- Allendorf, M. (2009). Description of gas-phase data (CHEMKIN) format. Accessed 22-05-2012, from the website <http://www.sandia.gov/HiTempThermo/chemkin.html>.
- Altman, R., Baljet, M., Barker, S., Brown, N., Dawoodjee, J., Freerks, R., and Gagliardi, T. (2010). IATA 2010 Report on Alternative Fuels. Technical report.
- ANSYS, I. (2009a). *ANSYS CFX-Solver Theory Guide*.
- ANSYS, I. (2009b). *ANSYS FLUENT 12.0 - Tutorial Guide*.
- ANSYS, I. (2009c). *ANSYS FLUENT 12.0 Theory Guide*.
- ANSYS, I. (2009d). *ANSYS FLUENT 12.0 User's Guide*.
- Bailis, R. and Baka, J. (2010). Greenhouse gas emissions and land use change from Jatropha Curcas-based jet fuel in Brazil.
- Barrientos, M. and Soria, C. (2012). Index Mundi jet fuel monthly price. Accessed 22-05-2012, from the website <http://www.indexmundi.com/commodities/?commodity=jet-fuel&months=360&currency=eur>.
- Blakey, S., Rye, L., and Wilson, C. W. (2010). Aviation gas turbine alternative fuels: A review. *Proceedings of the Combustion Institute*.
- Burcat, A. (2006). Ideal gas thermochemical database with update form active thermochemical tables. Accessed 22-05-2012, from the website <http://garfield.chem.elte.hu/Burcat/burcat.html>.
- Campbell, G. and Graham, N. (2012). Inside out south east. Accessed 17-02-2012, from the website <http://www.bbc.co.uk/programmes/b01bmq9z>.
- Chemical Education Group, U. o. W.-M. (2012). Student resources for general chemistry - GenChem textbook. Accessed 22-05-2012, from the website <http://chemed.chem.wisc.edu/chempaths/GenChem-Textbook/Density-761.html>.

- Condra, T. (2010). Lecture 2 slides from the Combustion Technology course at Institute of Energy Technology, Aalborg University.
- Corporan, E., Edwards, T., Shafer, L., DeWitt, M. J., Klingshirn, C., Zabarnick, S., West, Z., Striebich, R., Graham, J., and Klein, J. (2011). Chemical, thermal stability, seal swell, and emissions studies of alternative jet fuels.
- Dagaut, P. (2001). On the kinetics of hydrocarbons oxidation from natural gas to kerosene and diesel fuel. *Physical Chemistry Chemical Physics*, 4.
- Dagaut, P. and Cathonnet, M. (2005). The ignition, oxidation, and combustion of kerosene: A review of experimental and kinetic modeling. *Elsevier*.
- Ebbinghaus, A. and Wiesen, P. (2001). Aircraft fuels and their effect upon engine emissions. *Air & Space Europe*, 3.
- Edwards, T. (2010). *Jet Fuel Toxicology*. CRC Press. Chapter 2 - Jet Fuel Composition.
- Ellermann, T., Massling, A., Løfstrøm, P., Winther, M., Nøjgaard, J., and Ketzel, M. (2011). Undersøgelse af luftforureningen på forpladsen i Københavns Lufthavn Kastrup i relation til arbejdsmiljø. Technical report, Institut for Miljøvidenskab.
- EPA (2002). A comprehensive analysis of biodiesel impacts on exhaust emissions. Draft technical report.
- EurActiv (2011). Commission sets first emissions cap for aviation sector. Accessed the 24-05-2012, from the website <http://www.euractiv.com/transport/commission-sets-emissions-cap-aviation-sector-news-502817>.
- Finnair (2012). Biofuel transported passengers surely and more sustainably. Accessed 17-05-2012, from the website <http://blogs.finnair.com/2011/07/22/biofuels-transport-passengers-surely-and-sustainably/>.
- Flagan, R. C. and Seinfeld, J. H. (1988). *Fundamentals of air pollution engineering*. Prentice-Hall, Inc.
- Fournet, R., Warth, V., Glaude, P. A., Battin-Leclerc, F., Scacchi, G., and Côme, G. M. (1999). Automatic reduction of detailed mechanisms of combustion of alkanes by chemical lumping. *International Journal of Chemical Kinetics*, pages 1–16.
- Frassoldati, A., Cuoci, A., Faravelli, T., and Ranzi, E. (2011). Global kinetic mechanism of kerosene combustion for cfd applications. *Proceedings of the European Combustion Meeting 2011*, pages 1–6. Department of Chemistry, Materials and Chemical Engineering, Politecnico di Milano, Italy.
- Frassoldati, A., Faravelli, T., Ranzi, E., Cuoci, A., Ferraris, G. B., Granata, S., Cooke, J., Bellucci, M., Smooke, M., Gomez, A., Violi, A., Faravelli, T., Humer, S., Granata, S., Seiser, R., Seshadri, K., Ciajolo, A., Tregrossi, A., and Mallardo, M. (2012). Creck modeling group - gas phase combustion schemes. Accessed 17-05-2012, from the website <http://creckmodeling.chem.polimi.it/kinetic.html>. A database of several kinetic schemes for different species, made by different authors.
- Glassman, I. (1996). *Combustion, third edition*. Academic Press, San Diego, California. ISBN 0 12 285852 2.
- Group, E. S. I. (2000). *Quality and Trust in Industrial CFD - Best Practice Guidelines*.
- Hayashi, J., Watanabe, H., Jurose, R., and Akamatsu, F. (2010). Effects of fuel droplet size on soot formation in spray flames formed in a laminar counterflow. *Combustion and Flame*.

- Haynes, B. S. and Wagner, H. G. (1981). Soot formation. *Pergamon Press Ltd.*
- Hemighaus, G., Boval, T., Bacha, J., Barnes, F., Franklin, M., Gibbs, L., Hogue, N., Jones, J., Lesnini, D., Lind, J., and Morris, J. (2006a). Avaitaion fuels technical report. Technical report, Chevron.
- Hemighaus, G., Boval, T., Bosley, C., Organ, R., Lind, J., Brouette, R., Thompson, T., Lynch, J., and Jones, J. (2006b). Alternative jet fuels - a supplement to chevron's aviation fuels technical review. Technical report.
- Henneke, M., Smith, J. D., Jayakaran, J. D., and Lorra, M. (2001). *The John Zonk Combustion Handbook*. CRC Press.
- Hileman, J., Wong, H. M., Donohoo, P., Weiss, M., and Waitz, I. (2008). Alternative jet fuels. Massachusetts Institute of Technology.
- Hileman, J. I., Ortiz, D. S., Bartis, J. T., Wong, H. M., Donohoo, P. E., and Malcolm A. Weiss Ian A. Waitz, M. (2009). Near-term feasibility of alternative jet fuels. Technical report, Massachusetts Institute of Technology.
- Hileman, J. I. and Wong, H. M. (2008). The feasibility and potential environmental benefits of alternative fuels for commercial avitaion. *Massachusetts Institute of Technology*.
- iSchool, S. C. (2004). Average bond dissociation energies. Accessed on the 19-04-2012, from the website [http://www.saskschools.ca/curr\\_cotent/chem30/modules/module3/lesson5/bondenergy.html](http://www.saskschools.ca/curr_cotent/chem30/modules/module3/lesson5/bondenergy.html).
- Jensen, A. L., Kristensen, M. S., Schmidt, E. O., Mairold, A., Nielsen, S. S., Rasmussen, K. M., Jensen, C. U., and Lebreton, H. (2012). Experiment conducted on sr-30 turbo engine by te6-603 and te6-604.
- Kalaskar, V. (2009). Emission characteristics of jp-8, jp-900, fischer-tropsch (ft) and jp-8/ft blends in a model gas turbine combustor. Technical report.
- Kee, R. J., Rupley, F. M., Meeks, E., and Miller, J. A. (2000). *CHEMKIN: A software package for the analysis of gas-phase chemical and plasma kinetics*. Sandia National Laboratories Report SAND96-8216.
- Kennedy, I. M. (1997). Models of soot formation and oxidation. *Prog. Energy Combust. Sci.*, 23:95–132.
- Kinder, J. D. and Rahmes, T. (2009). Evaluation of bio-derived synthetic paraffinic kerosene (Bio-SPK). Technical report.
- Kircher, B., Yu, F., Schröder, F., and Turco, R. (1998). Ultrafine aerosol particles in aircraft plumes: Analysis of growth mechanisms. *Geophysical Reaseach Letters*.
- KLM (2012). Klm launches commercial flights Amsterdam – Paris on biofuel. Accessed 17-05-2012, from the website [http://www.klm.com/corporate/en/newsroom/press-releases/archive-2011/KLM\\_launches\\_commercial\\_flights\\_Amsterdam.html](http://www.klm.com/corporate/en/newsroom/press-releases/archive-2011/KLM_launches_commercial_flights_Amsterdam.html).
- Kärcher, B. and Fahey, D. (1997). The role of sulfur emission in volatile particle formation in jet aircraft exhaust plumes. *Geophysical Research Letters*.
- Lefebvre, A. H. and Ballal, D. R. (2010). *Gas Turbine Combustion - Alternative Fuels and Emissions*. CRC Press.

- Lewis, C. (2011). Swafea - technical feasibility and performance of biofuels in aviation - aero engine analysis. Technical report, The European Commission.
- Luque, R., Campelo, J., and Clark, J. (2011). *Handbook of biofuels production - Processes and technologies*. Woodhead Publishing Limited.
- McCrary, J. P., Stringer, V. L., Hansen, A. C., and Lee, F. C. (2007). Computational analysis of biodiesel combustion in a low-temperature combustion engine using well-defined fuel properties. *SAE International*.
- Miller, J. A. and Melius, C. F. (1992). The formation of benzene in flames. Sandia National Laboratories, Livermore, CA, 94551-0969.
- Millikan, R. C. (1962). *Nonequilibrium Soot Formation in Premixed Flames*. J. Ohys. Chem.
- Morawska, L., Moore, M. R., and Ristovski, Z. D. (2004). Health impacts of ultrafine particles - desktop literature review and analysis. *Australian Government Department of the Environment and Heritage*.
- O'Connaire, M., Curran, H. J., Simmie, J. M., Pitz, W. J., M., F. E., Curran, H. J., Westbrook, C. K., and M., M. (2012). Physical and life sciences directorate: Combustion chemistry. Accessed 22-05-2012, from the website [https://www-pls.llnl.gov/?url=science\\_and\\_technology-chemistry-combustion-mbutanoate](https://www-pls.llnl.gov/?url=science_and_technology-chemistry-combustion-mbutanoate). A database of several kinetic schemes for different species, made by different authors.
- Palmgren, F., Christensen, J., Ellermann, T., Hertel, O., Illerup, J. B., Ketzel, M., Loft, S., Winther, M., and Wählén, P. (2009). *Luftforurening med partikler – et sundhedsproblem*. Danmarks Miljøundersøgelser, Aarhus Universitet.
- Ponticel, P. (2012). New standard a major milestone for biofuels. Accessed 22-05-2012, from the website <http://www.sae.org/mags/aem/10540>.
- Press-Kristensen, K. (2011). Forurening med ultrafine partikler. Det Oekologiske Råd, Power Point Presentation.
- Price, H. J. (2011). Faa announces alternative energy investments for cleaner, more sustainable jet fuel. Accessed 22-05-2012, from the website [http://www.faa.gov/news/press\\_releases/news\\_story.cfm?newsId=13254](http://www.faa.gov/news/press_releases/news_story.cfm?newsId=13254).
- Ramanathan, V., Chung, C., Kim, D., Bettge, T., Buja, L., Kiehl, J. T., Washington, W. M., Fu, Q., Sikka, D. R., and Wild, M. (2005). Atmospheric brown clouds - Impacts on South Asian climate and hydrological cycle. *PNAS*, 102(15).
- Richter, H. and Howard, J. B. (2000). Formation of polycyclic aromatic hydrocarbons and their growth to soot—a review of chemical reaction pathways. *Pergamon Press Ltd*.
- Riesmeier, E., Honnet, S., and Peters, N. (2004). Flamelet modeling of pollutant formation in a gas turbine combustion chamber using detailed chemistry for a kerosene model fuel.
- Sander, U., Fischer, H., Rothe, U., and Kola, R. (1984). *Sulphur, Sulphur Dioxide and Sulphuric Acid*. The British Sulphur Corporation Limited, 1st edition.
- Strelkova, M. I., Kirillov, I. A., Potapkin, B. V., Safonov, A. A., Sukhanov, L. P., Umanskiy, S. Y., Deminsky, M. A., Dean, A. J., Varatharajan, B., and Tentner, A. M. (2007). Detailed and reduced mechanisms of jet a combustion at high temperatures. *Combustion Science and Technology*.

- Su, K. and Zhou, C. Q. (1999). Numerical study of parametric effects on gas turbine combustion nox emissions using a reduced mechanism.
- Technologies, T. (2007). *MiniLab - Gas Turbine Power System*. Turbine Technologies, LTD.
- Technologies, T. (2012). Turbine Technologies Ltd., 410 Phillips St. Chetek, WI USA.
- Turns, S. R. (2000). *An Introduction to Combustion - Concepts and Applications*. McGraw-Hill.
- Versteeg, H. K. and Malalasekera, W. (2008). *An Introduction to Computational Fluid Dynamics - The Finite Volume Method*. Pearson Education Limited, second edition edition.
- Vertés, A. A., Qureshi, N., Blaschek, H. P., and Yukawa, H. (2010). *Biomass to Biofuels - Strategies for Global Industries*. John Wiley and Sons Ltd.
- Wei-hua, Y., Jun, C., Rui, S., Xu-sheng, H., and Shuang-wen, S. (2011). Experimental investigation on impingement-effusion film-cooling behaviors in curve section. *Elsevier*.
- Wheeler, S. E., Robertson, K. A., Allen, W. D., Schaefer, H. F., Bomble, Y. J., and Stanton, J. F. (2007). Thermochemistry of key soot formation intermediates - C<sub>3</sub>H<sub>3</sub> Isomers. *American Chemical Society*.
- White, F. (2011). Soot packs a punch on Tibetan Plateau's climate. U.S Department of Energy.
- WS Atkins, C. and members of the NSC (2002). Best practice guidelines for marine applications of computational fluid dynamics.
- Yin, C. (2010). Lecture slides from the Computational Fluid Dynamics course at Institute of Energy Technology, Aalborg University.
- Yin, C. (2012). Consultation with Associate Professor Chungen Yin at Institute of Energy Technology, Aalborg University.



11.1 Structure of CHEMKIN Files

```

ELEMENTS
C H O N
END
SPECIES
O2      C2H5    C2H4    HO2     N2
OH      H2O     CO2     O
C5H5   CO      H       H2O2    C2H2
HCO     C2H3   H2      CH2O    HCCO
C6H5    C6H6   C6H14   C5H4O   C10H22
END
REACTIONS KCAL/MOLE MOLECULES
C10H22+O2=>C2H5+4C2H4+HO2      2E-21      3.4      46
C10H22=>2C2H5+3C2H4             1.25E-17   0        81
C10H22+OH=>C2H5+4C2H4+H2O      1.66E-15   2        -0.76
C10H22+HO2=>C2H5+4C2H4+2OH     4.07E-11   0        17
C6H14+O2=>C2H5+2C2H4+HO2      2E-21      3.4      46
C6H14=>2C2H5+C2H4               9.55E-16   0        81
C6H14+OH=>C2H5+2C2H4+H2O      4.68E-16   1.61     0.04
C6H14+HO2=>C2H5+2C2H4+2OH     2.44E-11   0        17
C6H6+O2=>C6H5+HO2              1.58E-20   3.2      61.5
C6H6+O=>C5H5+CO+H              3.39E-11   0        43
C6H6+OH=>C6H5+H2O              2.69E-16   1.42     1.45
C6H5+O2=>C5H5+CO+O             1.7E-11    0        3.6
C5H5+O=C5H4O+H                 9.33E-11   -0.02    0.02
C5H5+O2=>C5H4O+OH              3.02E-12   0.08     18
C5H4O=>2C2H2+CO                 5.62E-32   -6.76    68.5
C5H5+O=>C2H2+C2H2+HCO          5.37E-11   -0.17    0.44
C2H4+H(+M)=C2H5(+M)            1.26E-29   0        0.76
Low/ .4600E+19 .000 1070.0/
TROE/ 1.000 .1000E-14 95.00
H2O/ 5.00/CO2/ 3.00/H2/ 2.00/CO/ 2.00/ 200.0 /

C2H4+H=>C2H3+H2
C2H4+OH=>C2H3+H2O
C2H3+O2=>HCO+CH2O
C2H3+H=>C2H2+H2
CH2O+OH=>HCO+H2O
HCO+O2=>HO2+CO
HCO+M=CO+H+M 3.1E-7 -1 17
H2O/ 5.00/CO2/ 3.00/H2/ 1.90/CO/ 1.90/
C2H2+O=>HCCO+H 1.55E-15 1.4 2.22
HCCO+O=>H+2CO 1.58E-10 0 0
CO+OH=CO2+H 1.51E-17 1.5 -0.5
H+O2=O+OH 3.39E-10 -0.1 15.12
H+O2(+M)=HO2(+M) 7.76E-30 -0.86 0
Low/ .7000E+18 -.800 .0/
TROE/ .5000 .1000E-29 .1000E+31 /
H2O/ 18.00/H2/ 2.50/O2/ .00/CO/ 1.20/CO2/ 2.40/
OH+H2=H2O+H 3.63E-16 1.52 3.48
OH+OH=H2O+O 5.5E-20 2.42 -1.94
HO2+H=>2OH 7.41E-10 0 1.4
HO2+OH=>H2O+O2 4.79E-11 0 -0.497
CH2O+H=>HCO+H2 9.55E-17 1.9 2.74
HO2+H=>H2+O2 1.75E-10 0 2.06
HO2+HO2=H2O2+O2 7E-10 0 12.6
OH+OH(+M)=H2O2(+M) 6.31E-30 -0.9 -1.7
Low/ .2300E+19 -.900 -1700.0/
TROE/ .7346 94.00 1756. 5182. /
H2/ 2.00/H2O/ 6.00/CO/ 1.50/CO2/ 2.00/
H+OH+M=H2O+m 6.17E-26 -2 0
H2O/ 16.00/H2/ 2.00/CO2/ 1.90/
END

```

Figure 11.1: Mechanism shown in notepad.

Figure 11.1 shows the CHEMKIN mechanism file developed in this project. The CHEMKIN mechanism file is used as an input to ANSYS Fluent and contains the reactions in the mechanism and gas-phase data for all species in the mechanism.

The CHEMKIN file is divided into three blocks; Elements, Species and reactions. In the Element block the elemental atoms for all species in the mechanism are defined. Defined in the Species block are all species included in the mechanism. Note that N is included in the Element block, and N<sub>2</sub> is included in the species block, even though they are not included in the mechanism. The reason is that N<sub>2</sub> is needed as input for the combustion air (79% N<sub>2</sub> and 21% O<sub>2</sub>). N<sub>2</sub> is included as an inert gas that does not react or contribute with anything in the mechanism. In the reactions block all reactions in the mechanism and units are defined. Three columns containing values for the pre-exponential factor  $A$  [*cm, molec, s*], the power  $n$  [–] and the activation energy  $E_a$  [ $\frac{kcal}{mol}$ ] are specified for each reaction. These values are obtained from the reaction mechanism seen in Table 5.1 on page 34, and are used in the Arrhenius equation, which is used to calculate the rate constant,  $k$ :

$$k = A \cdot T^n \cdot \exp\left(\frac{-E_a}{RT}\right) \quad (11.1)$$

If a reaction has the form  $A + B \Rightarrow C$ , the rate constant for the reaction is pressure independent. The rate constant of some reactions are pressure dependent, for which the pressure dependency is specified by certain values (which will be explained shortly). Some reactions contain the species  $M$ , called the third body species. There are two ways of defining reactions that include the third body species, which will be explained shortly. It should be noted that two pressure ranges, a low-pressure range and high-pressure range, are specified in the file "thermo.db" (which will be explained later in this section). If the pressure falls in either of these regions the associated values to calculate the rate constant is used. If the reaction has the form  $A + B + M \Rightarrow C + M$ , it is assumed that the rate constant is in a low-pressure limiting region. If the reaction has the formula  $A + B (+ M) \Rightarrow C (+ M)$  the rate constant is assumed to be in the fall-off region, which is the region in between the low and high pressure regions. The rate constant in this region can be solved by using either of three different methods; Lindemann, Troe or Stewart et al. Details on each method and further explanation about the content of the CHEMKIN mechanism file can be found in Kee et al. [2000], and is not covered here.

In the reaction block the values used in the fall-off region for the reactions that include the third body species  $M$  are found from two kinetic mechanism databases; Frassoldati et al. [2012] and O'Connaire et al. [2012]. Multiple reaction mechanism are specified in these databases. Each of the reactions that includes  $M$  in this reports reaction mechanism was located in mechanisms from the databases, and the appropriate values for the fall-off region was obtained.

As explained above the low-pressure and high-pressure regions are defined in the "thermo.db" file, which is the thermodynamic data used by ANSYS Fluent to calculate heat capacity  $C_p$ , entropy  $S$  and enthalpy  $H$  for each species defined in the CHEMKIN mechanism file. The coefficients are used in the so called NASA polynomials Allendorf [2009], which are:

$$\frac{C_p}{R} = a_1 + a_2 T + a_3 T^2 + a_4 T^3 + a_5 T^4 \quad (11.2)$$

$$\frac{H^o}{RT} = a_1 + \frac{a_2}{2} T + \frac{a_3}{3} T^2 + \frac{a_4}{4} T^3 + \frac{a_5}{5} T^4 + \frac{a_6}{T} \quad (11.3)$$

$$\frac{S^o}{R} = a_1 \ln(T) + a_2 T + \frac{a_3}{2} T^2 + \frac{a_4}{3} T^3 + \frac{a_5}{4} T^4 + a_7 \quad (11.4)$$

The thermodynamical data are the coefficients  $a_1, a_2, \dots, a_7$  for high temperature and similar coefficient names for low temperature. The first 7 numbers seen on Figure 11.2 are associated with the high temperature range, while the last 7 are associated with the low temperature range. In the first line in each species block the first element and its number of occurrences are defined, followed by the second element its number of occurrences. The phase of the species is defined afterwards; G = gas. Following is the low temperature, high temperature and the transition (break) temperature.

```

C5H4O          C   5H   4O   1   G   0300.00
5000.00 1000.00      1
 0.55873435E+01 0.25414973E-01-0.92914588E-05 0.11234733E-08
0.00000000E+00      2
 0.33917246E+04-0.55297999E+01-0.42780910E+01 0.54617070E-01-
0.38099352E-04      3
 0.10594704E-07 0.00000000E+00 0.58909340E+04 0.44662980E+02
4
C5H5          C   5H   5   G   0300.00
5000.00 1000.00      1
 0.96899660E+01 0.18382620E-01-0.62648842E-05 0.93933772E-09-
0.50877081E-13      2
 0.25623351E+05-0.31230099E+02-0.31967390E+01 0.40813610E-01
0.68165048E-06      3
-0.31374590E-07 0.15772231E-10 0.29892910E+05 0.38699380E+02
4

```

Figure 11.2: Example of the input coefficients for a species in .



12.1 Data From Experiment

This chapter contains an example of the raw data obtained from the experiment conducted by Jensen et al. [2012].

MiniLab	4/17/2012		klokken 11.02.28				PRESSURES
	TEMPERATURES						compressor inlet
Time (sec)	Compressor inlet T1 (C)	Compressor exit T2 (C)	Turbine inlet T3 (C)	turbine exit T4 (C)	exhaust gas temp T5 (C)		P1 (kPa)
1009,551		6,735	206,848	642,067	581,354	411,916	3,983
1009,849		6,88	207,016	641,853	581,497	411,944	3,999
1010,141		6,857	207,47	642,305	581,613	412,096	3,986
1010,429		6,988	206,961	642,117	581,54	412,007	3,961
1010,718		6,913	207,373	642,694	581,728	412,072	3,99
1011,007		6,9	207,369	642,163	581,782	412,105	4,011
1011,292		6,942	207,327	642,688	581,904	412,213	3,991

compressor exit P2 (kPa)	turbine inlet P3 (kPa)	turbine outlet P4 (kPa)	P5 (kPa)	Fuel Flow (L/hr N1 (RPM))	Thrust (N)	
221,235	219,164	18,571	20,653	19,675	79696,91	149,241
221,479	219,695	18,533	20,618	19,656	79698,892	149,74
221,547	219,734	18,393	20,74	19,663	79696,822	149,246
221,245	219,566	18,52	20,432	19,648	79694,196	149,515
221,727	219,935	18,478	20,749	19,642	79697,347	149,4
221,568	219,714	18,504	20,569	19,663	79696,112	149,724
221,626	219,983	18,534	20,628	19,649	79688,162	150,508

Figure 12.1: An example of the raw data from the experiment. [Jensen et al., 2012].



13.1 Modelling results

Figures showing mass fractions, mean mixture fraction and temperature on planes 3, 4, 5, and 6. The planes are illustrated in Figure 8.1 on page 63 in chapter 8 on page 63.

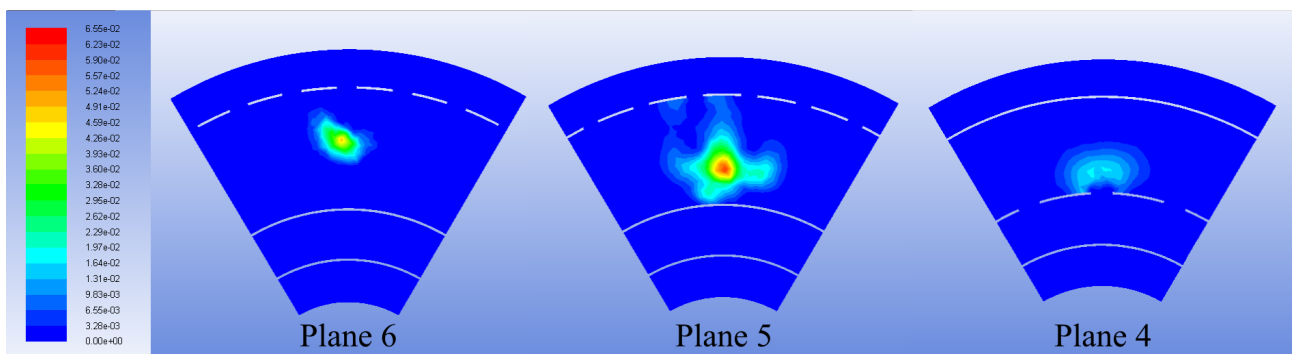


Figure 13.1: Mass fraction of benzene at plane 4, 5, and 6.

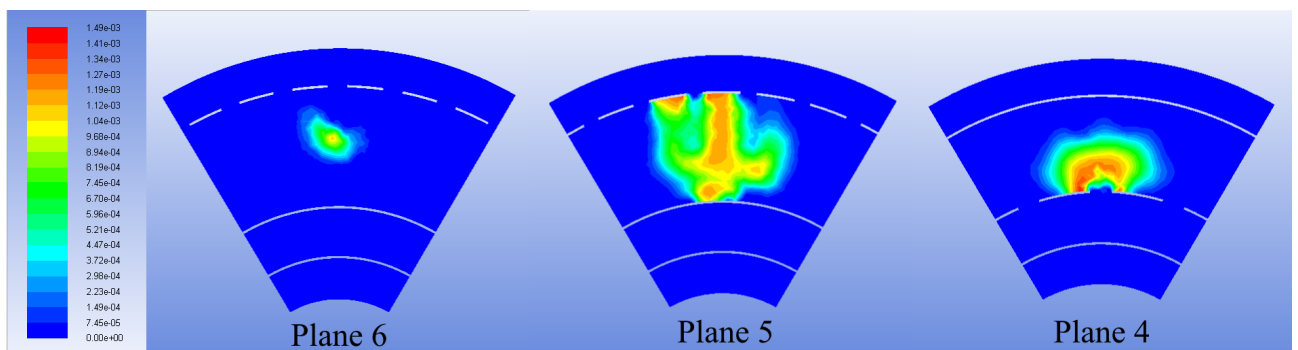


Figure 13.2: Mass fraction of acetylene at plane 4, 5, and 6.

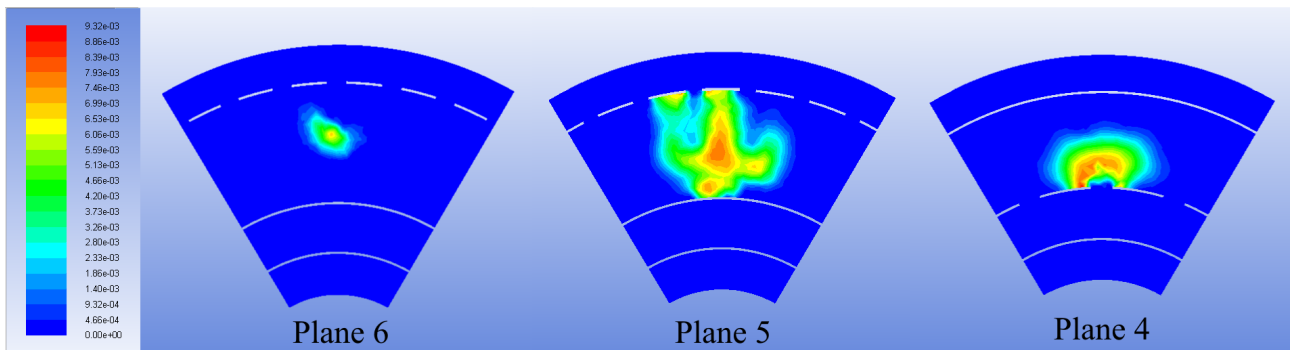


Figure 13.3: Mass fraction of ethylene at plane 4, 5, and 6.

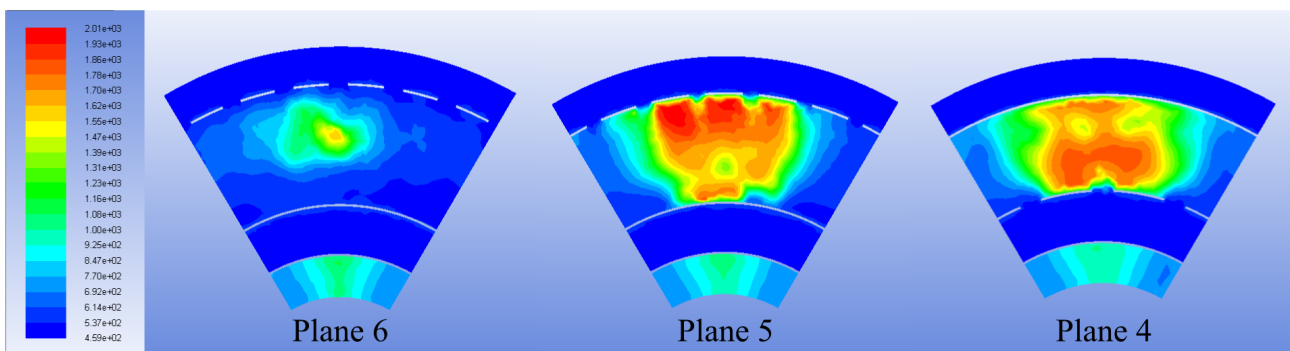


Figure 13.4: Temperature of the flow field at plane 4, 5, and 6. Units in [K]

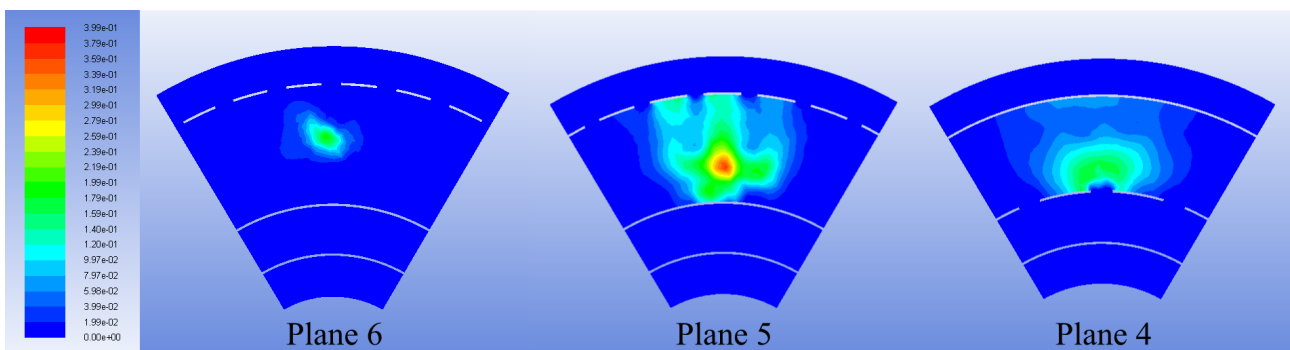


Figure 13.5: Mean mixture fraction at plane 4, 5, and 6.

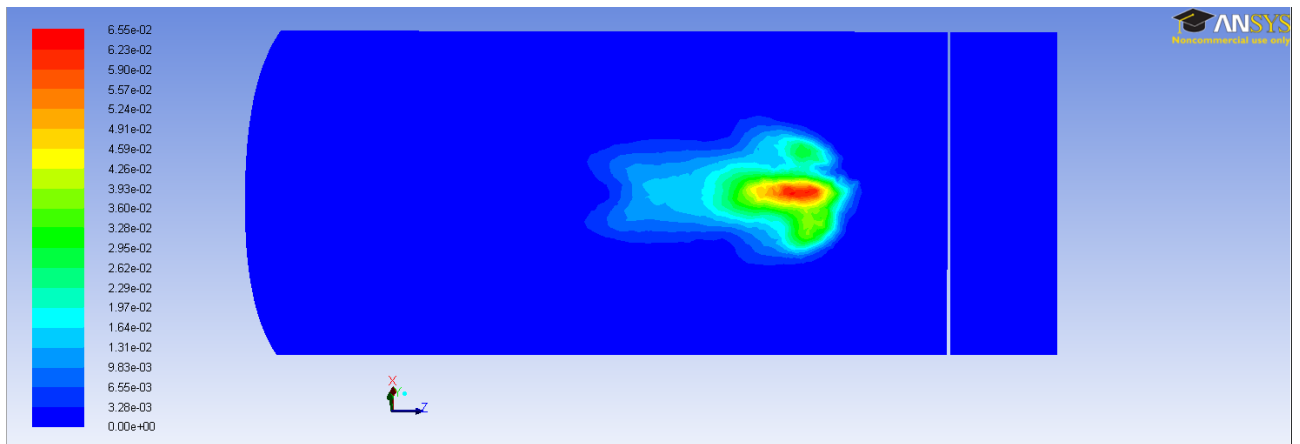


Figure 13.6: Mass fraction contours of benzene on plane 3.

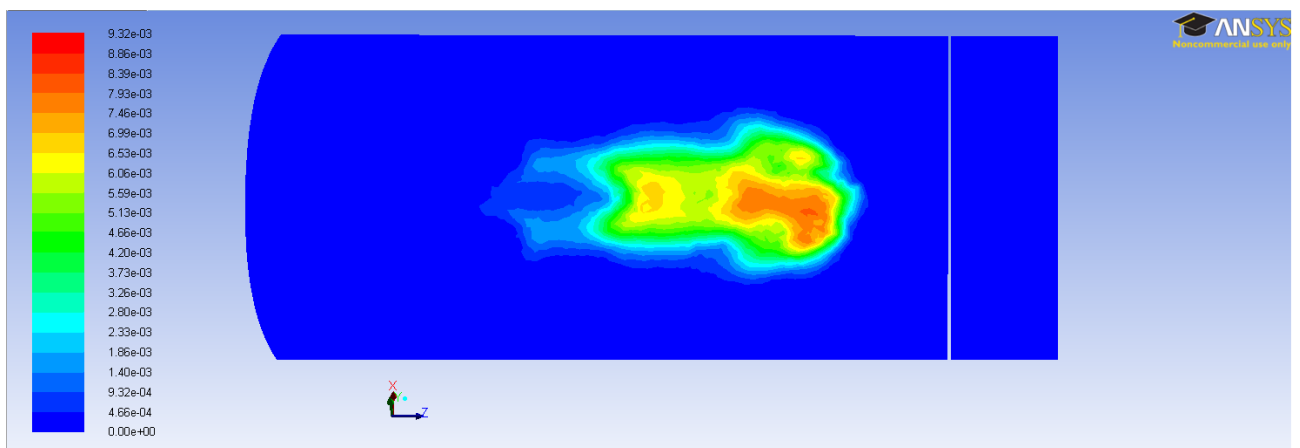


Figure 13.7: Mass fraction contours of ethylene on plane 3.

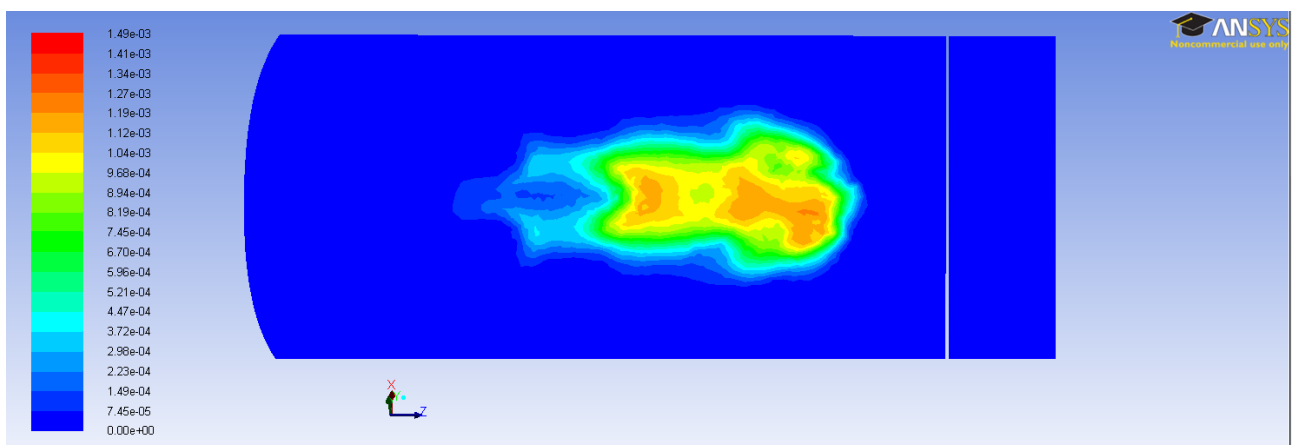
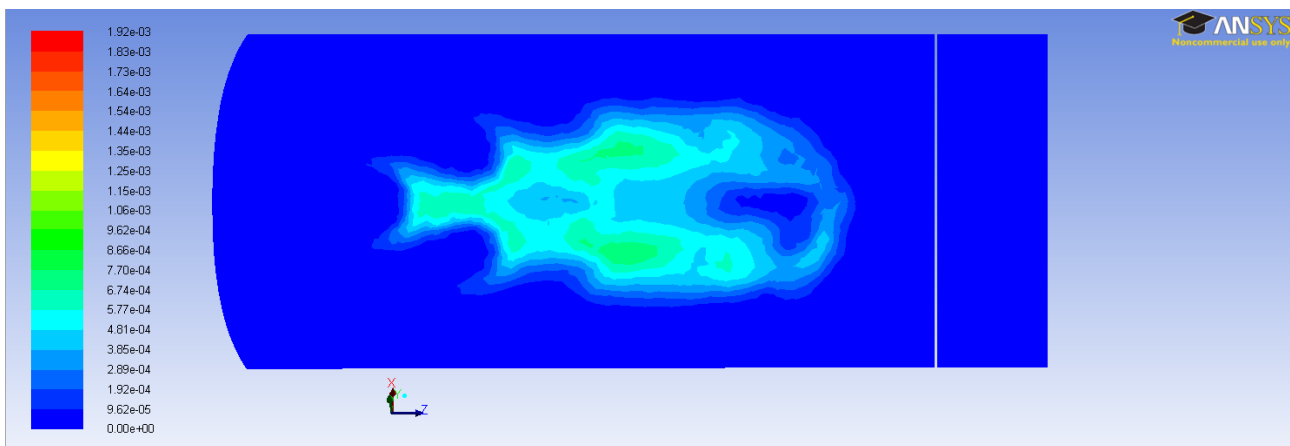


Figure 13.8: Mass fraction contours of acetylene on plane 3.



*Figure 13.9:* Mass fraction contours of OH on plane 3.

## 14.1 Mesh Independency Study

In order to create a mesh independency study of the unstructured tetrahedral, a 600,000 element mesh is first created. This is then coarsened using ANSYS ICEM, to two other meshes containing approximately 400,000 elements and 200,000 elements. Non-reacting Fluent simulations of the combustion chamber are done for each mesh, using similar setups of models and boundary conditions as shown in Table 7.2 on page 54.

In order to compare the three mesh sizes, a point is created in which velocity is tracked for all three mesh sizes. Tracking the velocity in the same point for each mesh size allows for a comparison of the meshes, to check if the the point value is independent of the mesh size. The point is located in the half circle bend of the combustor, going from the dilution zone into the outlet tunnel. The net mass flux, the net mass flow rate, is reported for each mesh, as well as the residuals are shown for each mesh size.

### 14.1.1 200,000 Element Mesh

The reported mass flux for the 200,000 element mesh is  $1.741058e-07 \frac{kg}{s}$ . The residuals of the 200,000 element mesh simulation can be seen in Figure 14.1.

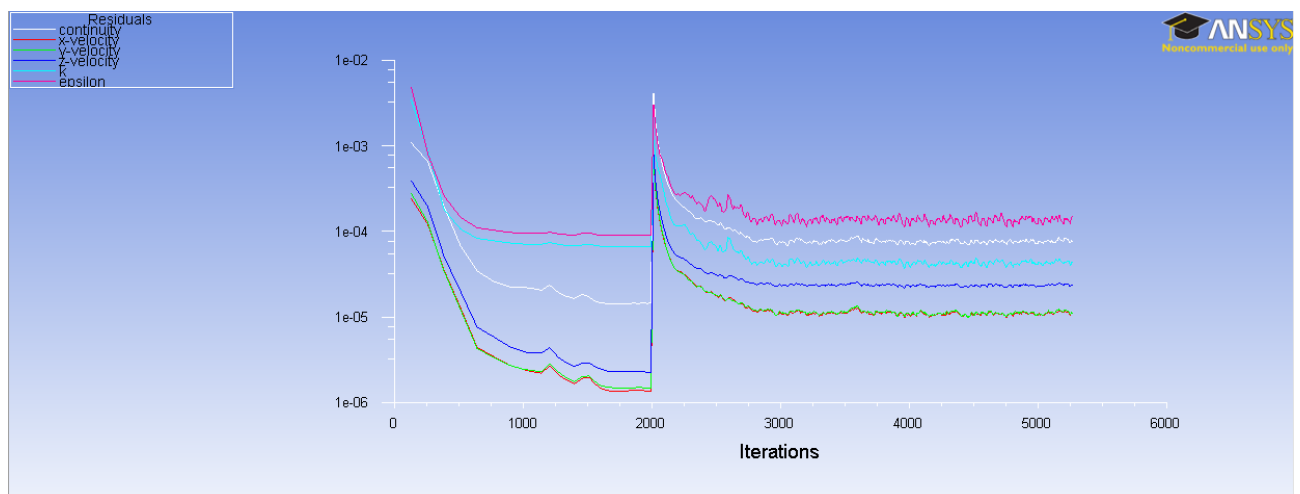


*Figure 14.1: The residuals of the 200,000 element mesh.*

The tracked velocity is shown in Figure 14.2.

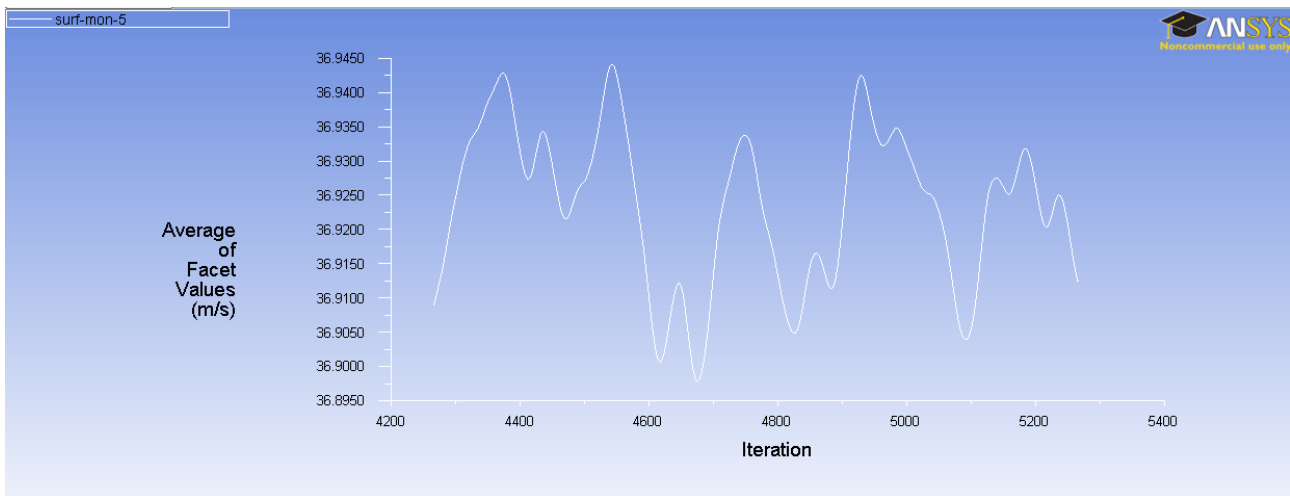


Figure 14.2: The tracked velocity of the 200,000 element mesh.

The biggest variation in velocity is from 36.8975 m/s to 36.9450 m/s which is a difference of 0.0475 m/s.

### 14.1.2 400,000 Element Mesh

The reported mass flux for the 400,000 element mesh is  $4.55598e-08 \frac{kg}{s}$ . The residuals of the mesh simulation can be seen on Figure 14.3.

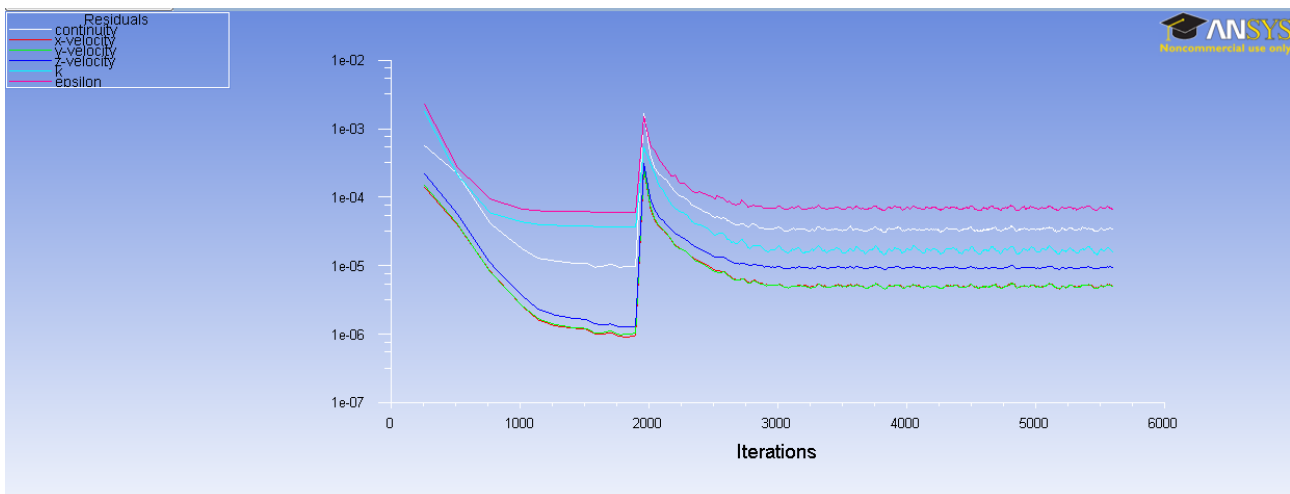


Figure 14.3: The residuals of the 400,000 element mesh.

The tracked velocity is seen on Figure 14.4.

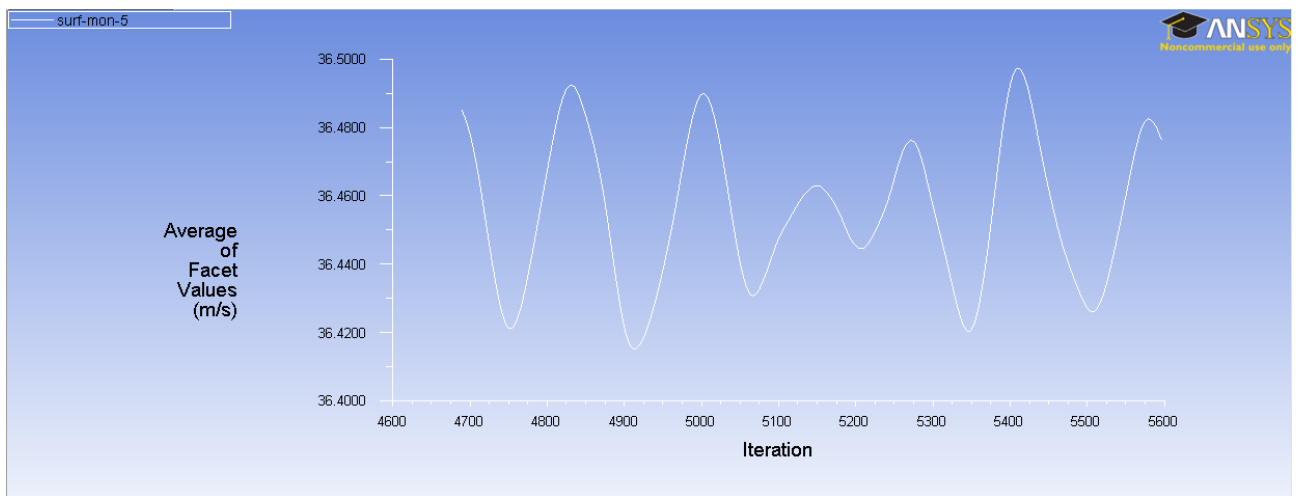


Figure 14.4: The tracked velocity of the 400,000 element mesh.

The largest variation in velocity is from 36.415 m/s to 36.500 m/s which is a difference of 0.085 m/s.

### 14.1.3 600,000 Element Mesh

The reported mass flux for the 600,000 element mesh is  $4.953555e-09 \frac{kg}{s}$ . The residuals of the 600,000 element mesh simulation can be seen on Figure 14.5.

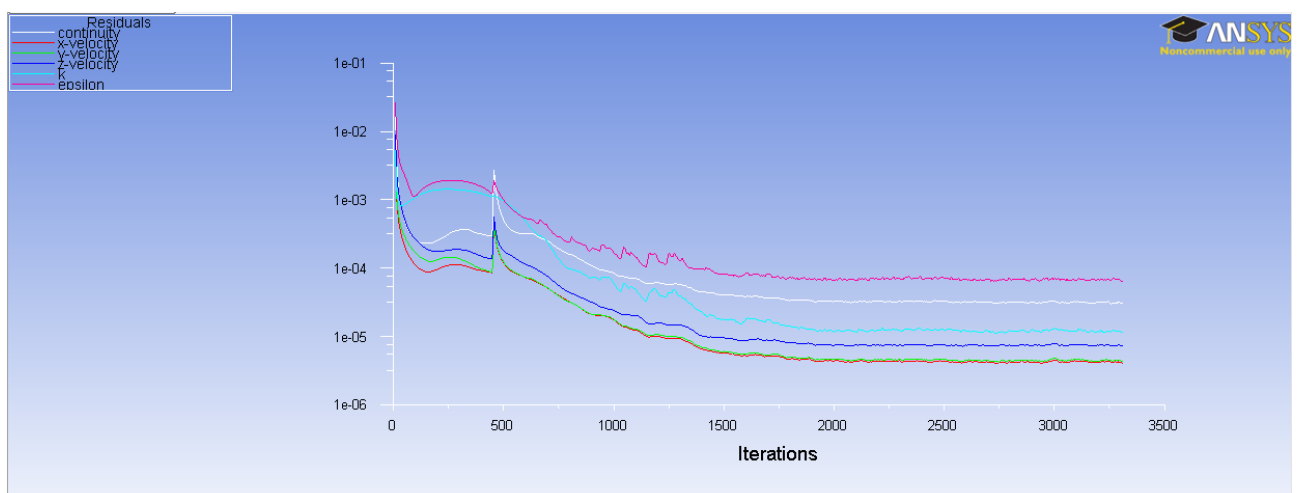
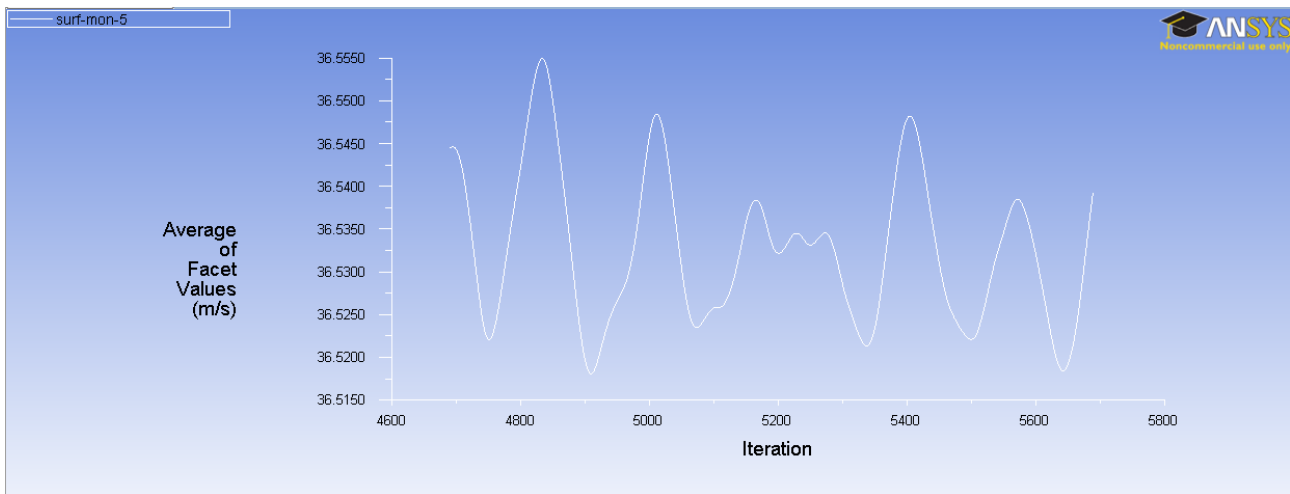


Figure 14.5: The residuals of the 600,000 element mesh.

The tracked velocity is seen in Figure 14.6.



**Figure 14.6:** The tracked velocity of the 600,000 cell mesh.

The biggest variation in velocity is from 36.5175  $m/s$  to 36.5550  $m/s$  which is a difference of 0.0377  $m/s$ .

#### 14.1.4 Comparison of the meshes

Comparing the point velocities in the three mesh sizes, it is seen that all three meshes have low velocity fluctuations in the tracked point in the combustor. Taking the approximate mean of the fluctuations based on the curves in Figure 14.2 on page 98, 14.4 on the previous page and 14.6, this show what i seen in Table 14.1.

**Table 14.1:** Point velocity mean values for the 3 meshes

	200,000 Element Mesh	400,000 Element Mesh	600,000 Element Mesh
Velocity [ $m/s$ ]	36.92	36.46	36.534

Comparing these mean values, these are all very close, but they do not resemble a completely mesh independent solution. Hence it is chosen to proceed with the 600,000 element mesh, as the additional cells will most likely yield the most accurate solution. Also considering that it is the intention to calculate a combustion simulation based on the chosen mesh, it is desired to capture as many gradients as possible.